

Rational Design of Nanostructured Surfaces for Energy Conversion and Wettability

by

Ashley R. Bielinski

A dissertation submitted in partial fulfillment
of the requirements for the degree of
Doctor of Philosophy
(Mechanical Engineering)
in The University of Michigan
2019

Doctoral Committee:

Assistant Professor Neil Dasgupta, Chair
Assistant Professor Rohini Bala Chandran
Professor Stephen Maldonado
Associate Professor Anish Tuteja

Ashley R. Bielinski

arbie@umich.edu

ORCID iD: 0000-0003-0773-5782

© Ashley R. Bielinski 2019

ACKNOWLEDGEMENTS

Thank you to everyone who supported me during my PhD. I am grateful to my research advisor, Neil Dasgupta, for his support and guidance through the PhD process. I particularly appreciate all the time and effort he committed in supporting myself and other lab members in our exploration of new research areas including nanostructures, semiconductors, and photoelectrochemistry – things outside the realm of what we typically learn in undergraduate mechanical engineering courses. I would also like to thank the remaining dissertation committee members, Professors Rohini Bala Chandran, Stephen Maldonado, and Anish Tuteja for their time and guidance.

Thank you to everyone else in the Dasgupta Research Group. It has been great to see our group grow from a couple students and a bare lab to the successful and productive team we have today. Particularly, I'd like to thank Susu for working with me closely over the past three years, for always being a wonderful resource as our “resident chemist,” and for becoming a great friend.

Much of my research over the years has been the product of strong collaborations across many disciplines. I like to thank Sam and Jimmy for their help and patient explanations as I learned to synthesize the Bi ALD precursor. I'd also like to thank Christian Schlepütz and Evguenia Karapetrova at beamline 33-BM-C at the Advanced Photon Source at Argonne National Lab for their guidance.

Thank you to my parents who have inspired and encouraged me to pursue both scientific and technical studies as well as creative pursuits. You have always supported me in trying new things and driven me to achieve more.

Finally, I would like to thank the ultimate frisbee community in Ann Arbor for being the source of many wonderful friendships and for providing much needed work-life balance.

This research was supported by the National Science Foundation (NSF) Graduate Research Fellowship under Grant No. DGE-1256260, University of Michigan Department of Mechanical Engineering Fellowship, and the University of Michigan Rackham Graduate School.

TABLE OF CONTENTS

ACKNOWLEDGEMENTS	ii
LIST OF FIGURES	vii
LIST OF TABLES	xv
LIST OF ABBREVIATIONS	xvi
ABSTRACT	xviii
CHAPTER	
I. Introduction	1
1.1 Nanoscale Materials by Design	1
1.2 Outline	3
1.3 Individual and Group Research Statement	4
II. Background	6
2.1 Nanowires for Solar Energy Conversion	6
2.1.1 Nanowire Geometry as a Model System	9
2.2 Zinc Oxide Nanowires	10
2.2.1 Properties and Applications of ZnO Nanowires	11
2.2.2 ZnO Nanowire Synthesis	12
2.3 Atomic Layer Deposition	13
2.3.1 Deviations from Ideal ALD	15
2.3.2 Atomic Layer Deposition for Surface and Interface Modification	17
2.3.3 Atomic Layer Deposition for Energy Conversion	17
2.4 Structural Wettability	18
2.4.1 Liquid Contact Angles on Planar Surfaces	18
2.4.2 Liquid Contact Angles on Nano- and Microstructured Surfaces	19

2.4.3	The Effects of Nanostructures on Contact Angle and Composite Interface Robustness	20
2.5	Photoelectrochemistry	22
2.5.1	Semiconductor-Liquid Junctions	23
2.5.2	Illuminated Semiconductor-Liquid Junctions	24
2.5.3	PEC Experiments in a 3-Electrode Half Cell	25
2.5.4	PEC Experimental Techniques	28
III.	ZnO Nanowire Growth with Tunable Orientation Using Atomic Layer Deposition Seeding	30
3.1	ALD Films for Heterogeneous ZnO Nanowire Nucleation	31
3.1.1	Control of Nanowire Orientation	33
3.1.2	Reduced Nanowire Nucleation on Ultra-Thin ALD ZnO Films	40
3.1.3	ALD Nanowire Seeding on a Range of Substrates	44
3.2	Conclusion	48
IV.	Rational Design of Hyperbranched Nanowire Systems for Tunable Superomniphobic Surfaces	49
4.1	Branched Nanowire Arrays	49
4.1.1	ALD Overlayers for Control of Nanowire Density	52
4.1.2	ALD Interlayers for Branched Nanowires	54
4.2	Super Omniphobicity	58
4.2.1	Hierarchical ZnO Nanostructures for Tunable Contact Angles	62
4.3	Conclusion	71
V.	Atomic Layer Deposition of Nanostructured Bismuth Vanadate Core-Shell Nanowire Photoanodes	72
5.1	Atomic Layer Deposition of Bismuth Vanadate	72
5.1.1	Super Cycle Approach to Depositing ALD BVO	74
5.1.2	Characterization of ALD BVO	78
5.1.3	Photoelectrochemical Performance of ALD BVO	83
5.2	Nanowire ALD BVO Core-Shell Photoanodes	87
5.3	Optimization of Nanostructure Geometry for Core-Shell ALD BVO Photoanodes	92
5.3.1	Optimization of BVO Film Thickness	93
5.3.2	Optimization of Nanowire Length	96
5.3.3	Optimization of Nanowire Density	100
5.4	Conclusion	103
VI.	Conclusions and Future Work	105

6.1	Conclusions	105
6.2	Future Work	106
	APPENDIX	108
	BIBLIOGRAPHY	121

LIST OF FIGURES

Figure

2.1	Core-shell-shell nanowire architecture showing the separation of light absorption depth, L_A , and charge carrier separation, L_D . The charge carrier separation is illustrated for a photoanode application showing the separation of holes to the electrode surface and electrons to a conductive nanowire core.	8
2.2	The number of papers published on ZnO nanowires since the year 2000 as determined by a Web of Science TM search for TOPIC: (ZnO nanowire) OR TOPIC: (zinc oxide nanowire).	11
2.3	Crystal facets of hexagonal wurtzite ZnO and typical shape from accelerated growth along the c-axis.	13
2.4	a) Diagram of one binary ALD cycle showing the reaction of precursor A with the substrate, the purge to remove excess precursor A and reaction products, the reaction of precursor B with precursor A on the substrate surface and the purge of excess precursor and reaction products. b) Cross-section SEM image showing a conformal film of ALD ZnO on etched GaP. Unlike line-of-sight limited processes, the nanoscale concave feature on the sidewall does not affect the film deposition for ALD. Adapted with permission from Lee, S.; Bielinski, A. R.; Fahrenkrug, E.; Dasgupta, N. P.; Maldonado, S. Macroporous P-GaP Photocathodes Prepared by Anodic Etching and Atomic Layer Deposition Doping. ACS Appl. Mater. Interfaces 2016, 8 (25), 16178–16185. Copyright (2016) American Chemical Society.	14
2.5	Temperature window for self-limiting ALD growth.	15
2.6	Young’s contact angle, θ , on a planar surface (left) and apparent contact angle, θ^* , on a structured surface (right), with center inset showing local Young’s contact angle on the textured surface.	19

2.7	Electronic band structure for an n-type semiconductor and a liquid electrolyte showing a) electronic states before semiconductor-liquid contact, b) electronic states after semiconductor-liquid equilibration, and c) electronic states when illuminated.	23
2.8	The air mass 1.5 G solar spectrum from the ASTM G-173 standard showing solar irradiance of earth's surface at sea level through 1.5 equivalent atmospheres corresponding to a sun zenith angle of 48.2°. Total irradiance that can be absorbed by a semiconductor is the area under the curve integrated from zero to the bandgap. Bandgaps for ZnO, BiVO ₄ , and Si are shown for reference. Spectrum data from NREL.	26
2.9	PEC experimental setup for 3-electrode half cell measurements. . .	27
3.1	Diagram of surface directed assembly using ALD to control the geometric parameters of heterogeneous nanowire independent of the substrate.	33
3.2	Cross-sectional SEM images and corresponding orientation histograms of NWs grown on different seed layer thicknesses. All other variables were held constant. Scale bar = 2 μm, except 100 and 300 cycles, where scale bar = 1 μm.	35
3.3	XRD χ-scan (tilt) data of the ZnO (002) peak for NWs and seed layers including (a) an overlay of the NW scans showing the orientation trends and (b, c) peak fitting for individual scans, where the solid red line is the perpendicular peak fit and the dashed line is the fit for the acute-angle peak, if any. (d) Full 180° χ-scan show symmetry about the perpendicular direction. (e) Symmetric θ-2θ scans for the seed layers.	37
3.4	a) The phi scan of NWs grown on a 15 cycle seed layer also communicates this same lack of in plane texture by showing that the intensity of the (101) and (002) peaks does not change for the full 360 rotation of the sample. This phi scan was performed at a chi angle of 30 which corresponds to the maximum (002) peak intensity across all chi angles. b) Full pole figure showing (002) intensity for the 100 cycle seed layer. The radial decrease in intensity from the center conveys the preferred orientation communicated by the chi scans and the lack of rotational variation indicates that there is no in-plane texture. . .	38

3.5	Plane-view BFTEM (a) and HRTEM (b) images of 15-cycle (1), 30-cycle (2), and 100-cycle (3) ZnO films deposited on SiO ₂ TEM grids, with FFT insets. (c) A magnified grain from the yellow box in the 15x sample, displaying the [001] wurtzite zone. A line profile over eight [100] planes measures $d_{100} = 2.64\text{\AA}$. (d) 100x ALD ZnO grain aligned along the [100] zone axis, with a measured projected unit cell dimension of ($d_{100} = 2.81\text{\AA}$, $d_{001} = 5.22\text{\AA}$).	41
3.6	Three sets of SAD patterns at left and simulated powder diffraction (ring type for TEM) at right of ALD 15x (a), 30x (b) and 100x (c) ZnO to obtain lattice parameter by direct comparison. (d) Line profile of diffraction intensity at center of 15x (red), 30x (blue) and 100x (black): direct comparison of R110 (110 reflection) on reciprocal space indicates isotropic shrinking of lattice parameter (a, c) by 6.9 and 5.4 % for ALD 15x and 30x respectively against original Wurtzite at 100x using $R_{hkl} \times d_{hkl} = \text{constant}$ relationship. e) Summary of measured R values (reciprocal distance from center to diffraction) and corresponding interplanar spacings of the consecutive 7 peaks. Please note that because each diffraction ring changes proportionally without distortion, the c/a ratio of Wurtzite ZnO is reserved. At low ALD cycle numbers, lattice parameters of Wurtzite structure appear contracted. Even though ring patterns at 15x are significantly broadened by small crystallite size, we can detect crystallinity. However, (002) peak seems to disappear (be weakened) or overlap with the (101) peak. Measured lattice parameters ($a=3.25\text{\AA}$, $c=5.22\text{\AA}$) are well matched with previous literature.	42
3.7	XPS scans of the ZnO O 1s spectrum in ALD films with various cycle numbers.	45
3.8	SEM analysis of (a) ZnO NWs grown on a 15-cycle seed layer on Si microposts, (b) ZnO NWs grown on a 100-cycle seed layer on Si microposts, (c) low-magnification image of ZnO NWs on Si microposts, (d) ZnO NWs grown on a track-etched polycarbonate membrane, (e) ZnO NWs grown on cotton fiber filter paper, and (f) ZnO NWs grown on a butterfly leg.	46
4.1	Diagram (not to scale) showing three successive levels of hierarchy along with the size, density, and orientation design parameters that can be controlled at each level.	50

4.2	(a) Diagram of low-density NW growth procedure showing the ZnO seed layer, sub-monolayer TiO ₂ overlayer, and hydrothermal NW growth. (b) A 90° cross-section scanning electron microscopy (SEM) image of low-density NWs grown with 4 cycles of TiO ₂ over a 100 cycle ZnO seed layer showing NW orientation perpendicular to the substrate. (c-e) Top-down SEM images of NWs grown with 3, 4, and 5 cycles of TiO ₂ over a 100 cycle ZnO seed layer showing decreased array density, increased D ₂ values, with increased number of TiO ₂ cycles.	53
4.3	a) Symmetric $\theta/2\theta$ synchrotron x-ray diffraction pattern showing wurtzite ZnO peaks from the nanosheets and a LDH peak from the substrate. b,c) SEM images showing the nanosheet morphology. . .	54
4.4	HRTEM and annular diffraction patterns (inset) of (a) single-crystalline ZnO NW, (b) ZnO NW with epitaxial ALD ZnO film growth, and (c) ZnO NW with amorphous ALD TiO ₂ blocking layer and polycrystalline ALD ZnO seed layer. (d) Energy-dispersive X-ray analysis for element mapping and (e) dark-field scanning transmission electron microscopy (STEM) image of ZnO NW with ALD TiO ₂ and ZnO films, where the red box shows the area analyzed in (d).	56
4.5	(a) Diagram of ALD interlayer procedure for branched NW seeding starting with an array of low-density ZnO NWs, then (i) adding an ALD TiO ₂ blocking layer, (ii) adding an ALD ZnO seed layer, and (iii) hydrothermal NW growth. (b) Cross-section SEM of branched ZnO NWs. (c) Cross-section SEM and diagram of a split branched NW and showing the NW core, ALD TiO ₂ blocking layer, ALD ZnO seed layer, and ZnO branches. (d) SEM top-down view of branched ZnO NWs.	57
4.6	SEM micrographs of branched nanowires grown with 5 cycle ALD TiO ₂ overlayers on a) polyamide film, b) glass slide, and c) cotton fiber filter paper.	59
4.7	SEM images of hyperbranched structures with three levels of hierarchy (a) 45° view of branched ZnO NWs on Si microposts (seeded by a 4 cycle TiO ₂ overlayer), (b) branched NWs grown with higher density trunks (seeded by a 4 cycle TiO ₂ overlayer), and (c) branched NWs grown with lower density trunks (seeded by a 5 cycle TiO ₂ overlayer).	59
4.8	a,b) SEM showing nanowires of different densities grown on Si micropost arrays.	60

4.9	a,b) SEM images showing Si micropost arrays used as substrates. The scalloped texture from the cyclic deep reactive-ion etching (DRIE) Bosch process used to create the Si microposts can be seen on the post side walls.	65
4.10	Advancing and receding contact angles with (a) water and (b) hexadecane versus the spacing ratio (D^*) for planar, unbranched, and branched NWs of varying density on planar and micropost substrates. (c) Robustness factor A^* measured with hexadecane droplet impact tests versus the spacing ratio D^* . The solid colored lines are theoretical A^* values for hexadecane calculated over varying inter-hoodoo spacing (D) for arrays of hoodoos, each corresponding to a fixed hoodoo cap radius, R (labeled on the plot). (d) Representative photographs from the contact angle goniometer of the advancing contact angles with water, hexadecane, decane, and octane on a sample of BNW-4s on 13×32 posts.	66
4.11	(a) Photograph of $\sim 3 \mu\text{L}$ dyed liquid droplets on a micropost array with branched NWs (BNW-4s on 13×32). (b) Frames from a high-speed video of a $\sim 10 \mu\text{L}$ hexadecane droplet completely bouncing from the sample in (a) after being dropped onto it from 5 cm. . . .	68
5.1	a) Super cycle deposition approach for ALD BVO showing the layered structure of binary oxides as-deposited and the post-annealed ternary oxide film. b) Photograph of as deposited (left) and annealed (right) BVO films. The annealed film shows a color transition to the characteristic yellow color of monoclinic BVO. c) Cross-sectional HAADF-STEM image of as deposited structure (left) and EDS elemental mapping (right). Each layer consists of 250 ALD cycles of the binary oxide. d) Cross-sectional HAADF-STEM image of annealed nanolaminate structure (left) and the corresponding EDS elemental mapping (right).	75
5.2	Thicknesses of ALD V_2O_5 and Bi_2O_3 films measured via spectroscopic ellipsometry. The linear fit of these data sets shows a growth rate of $0.48 \text{ \AA}/\text{cycle}$ for V_2O_5 and $0.30 \text{ \AA}/\text{cycle}$ for Bi_2O_3	76
5.3	Material composition of ALD BVO films as determined by XPS for (a) BVO deposited with different super cycle thicknesses, 10:10, 50:50, 250:250, where all have net 1,000 cycles and (b) BVO deposited with different cycle ratios, 250:250, 270:230, and 290:210, where all have net 1,000 cycles.	77

5.4	Left: XPS Bi 4f peaks (left: Bi 4f _{5/2} and right: Bi 4f _{7/2}) before and after Ar ⁺ sputtering to remove adventitious carbon. Right: TEM EDS mapping of O K, Bi L, and V K in the annealed BVO film. . .	78
5.5	(a) Reflectance, (b) transmittance, and (c) absorptance spectra of ALD BVO films of various Bi/V compositions. (d) compares absorptance data of the BVO films collected at air/film (solid line) and at air/glass/water/film (dashed line) interface.	79
5.6	Tauc plots of (a) 250:250, (b) 270:230, and (c) 290:210 BVO photoelectrodes.	80
5.7	GIXRD patterns of 250:250 (red - annealed; green - as-deposited), 270:230 (blue), and 290:210 (gray) films with reference patterns for BVO, V ₂ O ₅ , and Bi ₂ O ₃ . The BVO, V ₂ O ₅ and Bi ₂ O ₃ references are from PDF no. 01-083-1698, 01-072-0598, and #ICSD 169686 respectively.	81
5.8	AFM for grain size and surface roughness characterization of planar ALD BVO on FTO substrates for BVO samples (a) 250:250, (b) 270:230, and (c) 290:210. AFM (d) area and (e) line scan measurements of 290:210 ALD BVO demonstrating the film thickness measurements.	82
5.9	Current-voltage (J-V) responses of planar ALD BVO photoelectrodes for sulfite oxidation. (a) Dark (solid line) and illuminated (dashed line) J-V responses of an ALD BVO photoelectrode with 250:250, 270:230, and 290:210 Bi:V pulse ratio collected under AM1.5G front illumination. (b) IPCE and (c) APCE of the same ALD BVO photoelectrodes collected at 0.6 V vs. RHE. The data was obtained under AM1.5 G illumination in 0.25 M potassium borate buffer with 1 M Na ₂ SO ₃ at pH 9.2.	83
5.10	LSV of ALD BVO photo electrodes (a) comparing with and without an ALD SnO ₂ interlayer and (b) comparing front and back illumination of the working electrode. The data was obtained under AM1.5 G illumination in 0.25 M potassium borate buffer with 1 M Na ₂ SO ₃ at pH 9.2.	84
5.11	Chronoamperometry data collected from a 250:250 BVO photoanode under AM 1.5G illumination in 0.25 M potassium borate buffer containing 1 M Na ₂ SO ₃ (pH 9.2) with an applied potential of 0.6V vs. RHE.	88

5.12	Energy diagram of a ZnO/SnO ₂ /BVO system and the photogenerated charge carrier pathways under solar irradiation.	89
5.13	(a) Current-voltage ($j-V$) responses of plain, unoptimized ZnO nanowire photoelectrode (blue), ZnO nanowires with 3 nm ALD SnO ₂ interlayer (black), and ZnO nanowires/SnO ₂ /ALD BVO (red) in dark and under AM 1.5G illumination in 0.25 M potassium borate buffer with 1 M Na ₂ SO ₃ (pH 9.2). (b) Chronoamperometry of plain ZnO NW (black) and ZnO NW with 3 nm ALD SnO ₂ interlayer (orange) under AM 1.5G illumination in 0.25 M potassium borate buffer with 1 M Na ₂ SO ₃ (pH 9.2)	90
5.14	a) Diagram of BVO/ZnO nanostructured photoelectrodes with SnO ₂ interlayer, b) SEM micrograph of BVO/ZnO photoelectrode, c) Bright-field TEM and EDS mapping of BVO/ZnO photoelectrode, scale bar is 50nm, and d) J-V response of planar BVO and nanostructured BVO/ZnO photoelectrodes under AM1.5G front illumination.	90
5.15	(a) Reflectance and (b) transmittance spectra of a planar ALD BVO film and ALD BVO film deposited on ZnO nanowires.	91
5.16	A faceted ZnO NW coated with 9 nm ALD SnO ₂ and 1 super cycle ALD BVO. The BVO preferentially crystallizes on the flat facets rather than the high curvature edges.	92
5.17	Design parameters for a core-shell BVO NW photoanode.	93
5.18	a) UV-vis light absorption for planar and NW photoelectrodes with 1,2, and 4 super cycles of ALD BVO. Each super cycle consisted of 270 cycles of Bi ₂ O ₃ followed by 230 cycles of V ₂ O ₅ . b) Photocurrent at 1.23 V vs. RHE for sulfite oxidation as a function of BVO film thickness for planar and nanowire photoanodes. c-e) Cross-section SEM of ZnO NWs with 1, 2, and 4 super cycles of ALD BVO, respectively.	95
5.19	a) BVO NW photoelectrode absorption as a function of NW length. b) BVO NW photocurrent as a function of nanowire length for 1-sun illumination and sulfite oxidation (borate buffer, pH 9.2). c) External quantum efficiency, or IPCE, and d) internal quantum efficiency, or APCE, of different length NWs.	97

5.20	a,b) SEM of individual NWs of different sizes showing how the ALD BVO grain morphology differs depending on the NW diameter and faceting. c-e) Cross-section SEM images of 0.16, 0.71, and 2.85 μm ZnO NWs with ALD BVO, as examples of the NW electrodes with different length NWs. f-h) ALD BVO on ZnO NWs with different densities. The NW density was controlled with 4, 5, and 6 cycles TDMAT over the ALD ZnO seed layer, respectively.	99
5.21	a) BVO NW photoelectrode absorption as a function of NW array density. b) BVO NW photocurrent as a function of nanowire array density for 1-sun illumination and sulfite oxidation (borate buffer, pH 9.2). c) External quantum efficiency, or IPCE, and d) internal quantum efficiency, or APCE, of different NW array densities. The legend notation refers to the array density by the number of ALD TDMAT TiO_2 cycles deposited over the ZnO seed layer in the NW synthesis. See Figure 5.20 f-h for a reference of the resultant array density.	102
A.1	Ellipsometry on 100, 200, and 300 cycles was used to determine the average growth rate for the ZnO ALD. The growth rate was calculated as 1.92 \AA /cycle. The fit was linear least squares with an R value of 1.000 indicating that there is very little variation in the growth rate across cycles and samples.	115
A.2	Diagram of hydrothermal ZnO nanowire growth.	116

LIST OF TABLES

Table

4.1	Contact Angles on Fluorosilanized Samples with Different Combinations of Microscale Geometries (Planar and Microposts with Varying Spacing) and Nanoscale Geometries (Planar ALD Coatings, Unbranched Nanowires, and Branched Nanowires with Increasing Internanowire Spacing)	64
5.1	Surface roughness, film thickness (height), and grain size of the ALD BVO films annealed on FTO glass substrates.	82
5.2	Tabulated PEC responses of planar undoped single-junction BVO photoelectrodes.	85
5.3	Tabulated PEC responses of ALD photoanodes.	86

LIST OF ABBREVIATIONS

AFM atomic force microscopy

ALD atomic layer deposition

APCE absorbed photon to current efficiency

BFTEM bright field transmission electron microscopy

BNW branched nanowires

BVO bismuth vanadate

CA chronoamperometry

CVD chemical vapor deposition

DEZ diethylzinc

DRIE deep reactive-ion etching

EDS energy x-ray dispersive spectroscopy

FF fill factor

FFT fast Fourier transform

GIXRD grazing incidence x-ray diffraction

HAADF-STEM high-angle annular dark field scanning transmission electron microscopy

HER hydrogen evolution reaction

HRTEM high-resolution transmission electron microscopy

IPCE incident photon to current efficiency

LSV linear sweep voltammetry

NHE normal hydrogen electrode
NW nanowire
OER oxygen evolution reaction
PEC photoelectrochemistry
PTFE polytetrafluoroethylene
PV photovoltaic
QE quantum efficiency
RHE reversible hydrogen electrode
SAD selected area diffraction
SALD spatial atomic layer deposition
SEM scanning electron microscopy
STEM scanning transmission electron microscopy
TDMAT tetrakis(dimethylamido)titanium
TEM transmission electron microscopy
UHV ultra-high vacuum
XPS x-ray photoelectron spectroscopy
XRD x-ray diffraction

ABSTRACT

Nanoscale semiconductor materials offer many potential benefits for energy conversion. 3D nanostructures can provide light trapping and antireflective properties, while increased surface area reduces local flux and provides increased capacity for catalyst loading. Core-shell structures can improve transport phenomena and enable the use of a more diverse range of materials. However, these geometries present new challenges. Increased surface area can lead to higher recombination rates or surface degradation and many nanoscale fabrication methods can be difficult to scale-up. Engineering heterogeneous nanostructures with precise control over physical and material properties is an important step in understanding the impact of these parameters on the performance of energy conversion devices.

In this thesis, ZnO nanowires are used as a model system for engineering heterogeneous nanostructures. Atomic layer deposition (ALD) surface modification was used to direct the hydrothermal growth of ZnO, enabling arrays of nanowires and branched nanowires with precise control of density, orientation, and size. ALD is well suited to thin film deposition and surface modification for nanostructured surfaces. ALD consists of self-limiting gas-phase surface reactions that are not line-of-sight limited resulting in conformal coverage of even high aspect ratio 3D nanostructures with angstrom scale thickness control. The utility of this approach was demonstrated through the rational design of three-level hierarchical structures for structural omniphobicity, producing surfaces that repel both high and low surface tension liquids.

While ZnO is a semiconductor, its wide band gap limits applications for solar energy conversion. To address this limitation, ALD of bismuth vanadate (BVO),

a mid-band gap semiconductor, was developed to enable core-shell nanostructures. BVO was deposited using ALD of alternating films of bismuth and vanadium oxides. A novel Bi-alkoxide precursor was used to enable precise control of stoichiometry along the spectrum of Bi-rich to V-rich compositions, and monoclinic BVO films were obtained after post-annealing. Photoanodes for photoelectrochemical water oxidation were created from the ALD BVO in both planar and nanowire configurations. A planar photoanode of 42 nm thick BVO produced a photocurrent density of 2.24 mA/cm² at 1.23 V vs. RHE.

Core-shell-shell nanowire arrays consisting of ZnO nanowires, ALD SnO₂, and ALD BVO were used to create nanostructured BVO photoanodes. The geometry of these photoanodes was rationally designed to investigate the influence of different geometric parameters and to maximize their photocurrent. The thickness of the BVO was optimized to improve charge separation and transport while the length and density of the nanowire arrays were controlled to optimize light absorption. A photocurrent of 3.76 mA/cm² at 1.23 V vs. RHE was achieved on high density 1.4 μm ZnO nanowires with a 20 nm ALD BVO film as the primary absorber. These values are the highest reported to date for any ALD photoanode.

In summary, a nanoscale toolbox consisting of ALD thin films, ZnO nanowires, and complex branched nanostructures has been demonstrated as a method to study the influence of different materials and geometric properties on performance of nanostructured surfaces and devices. Understanding these properties enables the rational design of nanostructures tailored to individual applications.

CHAPTER I

Introduction

1.1 Nanoscale Materials by Design

The future of nanoscience lies in our ability to create increasingly complex material systems composed of heterogeneous building blocks in order to approach the design paradigms that we use for fabrication of macroscopic engineering systems.¹ Rational design of three-dimensional structures and interfaces at the nanoscale is imperative for the continued development of many technologies such as solar energy conversion, electrochemical energy storage, and semiconductor devices. This trend can be seen directly in evolution of field-effect transistors (FETs) from planar devices to three-dimensional nanoscale finFET designs, and even smaller to architectures such as nanowire FET designs.^{2,3} In comparison to bulk macroscale devices, at the nanoscale, geometry can directly affect the properties and performance of a material. Furthermore, as dimensions shrink, surfaces and interfaces begin to play larger roles. Simply scaling down an existing design may be difficult not only due to manufacturing limitations, but also due to altered performance from nanoscale effects.

In energy conversion systems including photoelectrochemistry, photovoltaics, batteries, and fuel cells, nanostructures can provide benefits such as high local surface area, while maintaining a small macroscopic footprint. This can reduce local electric and chemical flux and provide increased catalyst loading or reaction sites. Nanoscale

geometry can also influence how a material interacts with light resulting in light trapping, antireflectivity, or high transmission depending on the design. However, these same properties can also result in deleterious effects such as increased interface and surface recombination in semiconductor devices or active material consumption in the solid electrolyte interphase in batteries.

In order to design efficient systems of nanomaterials for the collection and storage of energy it is essential to consider the device architecture as a whole to maximize the beneficial effects and minimize the damaging effects. Independent design and optimization of each component is insufficient in predicting performance when multiple components are assembled.

Here I present a method to rationally tune geometric parameters of nanowire arrays via surface modification of heterogeneous substrates. This enables the study and optimization of geometric parameters for a range of materials and applications. Literature frequently shows the beneficial effects of using nanostructured surfaces rather than planar ones, but rarely are those nanostructures carefully controlled or optimized. Creating nanostructures and interfaces is limited by the available synthesis and manufacturing techniques for the target material. Often there is a trade-off between order and precision vs. scalability and cost. When carefully designed nanostructures are presented, they are often limited to certain materials such as Si with intensive processing such as photolithography and etching. This research looks to develop a tool box of heterogeneous thin films and nanostructures to be used in understanding the role of geometry and interfaces in a variety of applications including photoelectrochemistry and surface wettability. This drives the transition from a proof of concept tests to a rationally designed and engineered surfaces, optimized for each unique application.

1.2 Outline

Under the guiding principle of materials by design, this thesis presents the development of two material synthesis techniques and two applications. First, Chapter II provides a summary of the concepts and techniques that are most relevant to understanding the results presented in the later chapters. These topics include the properties of nanostructures relevant to solar energy conversion, the properties and synthesis of ZnO nanowires and why they have been chosen as a model system for this research, the basic theory and application of atomic layer deposition, the physics of structural wettability, and the physics of photoelectrochemistry (PEC) using semiconductor photoelectrodes.

In chapter III, atomic layer deposition (ALD) is used to control the size, orientation, and density of hydrothermally grown ZnO nanowire arrays by modifying the substrate surface to influence the nanowire nucleation. ALD is shown to enable heterogeneous nanowire nucleation on a wide range of substrates from three-dimensional micro and nanostructures to polymers and biological substrates.

Chapter IV expands on this approach of ALD surface modification to develop a method for the bottom-up growth of branched ZnO nanowires. ALD TiO_2 was used to selectively block nanowire nucleation for low density nanowires and it was used to block epitaxial growth of ALD ZnO on ZnO nanowires to enable branched nanowires. The rational design of these nanowire arrays to tune the liquid contact angle for both high and low surface tension liquids demonstrates a possible application for the precise control of geometric parameters for ZnO nanowire arrays, branched nanowire arrays, and hyperbranched nanowire arrays. Mathematical models of composite solid-liquid-gas interfaces drive the design of a super omniphobic hyperbranched nanowire array that was shown shown to repel a range of liquids with high contact angles and low hysteresis.

Chapter V begins with the second material synthesis technique, the development and characterization of atomic layer deposition of bismuth vanadate (BVO). The second application is the development of core-shell nanowire PEC photoanodes using ZnO nanowires to define the geometry and ALD BVO as the primary light absorber. The geometric control of ZnO nanowires developed in Chapter III as well as interface modification using ALD SnO₂ were leveraged to optimize the optical and electronic properties of the photoanodes.

Chapter VI concludes this thesis and presents opportunities for future work. Appendix A includes the experimental methods for the results presented in Chapters III–V.

1.3 Individual and Group Research Statement

The results presented in this thesis represent not only my personal research efforts, but also the culmination of many collaborations and would not have been possible without the expertise and efforts of my coauthors. Below is a summary of each collaborator’s contributions.

Chapter III was adapted from was adapted from Bielinski, et al. 2015⁴. Development of the ALD procedure for control of hydrothermal ZnO nanowires on diverse substrates, scanning electron micrographs (SEM), geometric analysis, and synthesis of all samples was completed by Ashley Bielinski. Synchrotron x-ray diffraction and analysis was performed by Ashley Bielinski at the Advanced Photon Source at Argonne National Laboratory with the help and guidance of beamline scientist Christian Schlepütz. Christian Schlepütz also provided data processing for the x-ray diffraction pole figure measurements. Hee Joon Jung performed the transmission electron microscopy and lattice contraction analysis for the ALD ZnO seedlayers. Kevin Wood collected and analyzed the x-ray photoelectron spectroscopy data for the ZnO seedlayers. Eric Kazyak wrote the R code to analyze and plot the nanowire size and

orientation statistics from the data Ashley collected, as well as he prepared and imaged the nanowires on the butterfly substrate. Neil Dasgupta provided guidance and support.

Chapter IV was adapted from Bielinski, et al. 2017⁵, which consisted of an equal collaboration between Ashley Bielinski and Mathew Boban in Prof. Anish Tuteja's research group at the University of Michigan. Ashley Bielinski developed the ALD synthesis process for hyperbranched ZnO nanowire arrays, studied the range of geometric parameters, prepared all nanowire and ALD samples, performed SEM imaging, and performed XRD data collection and phase analysis. Mathew Boban developed the computational model, performed silanization, and performed contact angle measurements. Yang He prepared the Si micropost substrates and Duck Hyun Lee performed TEM analysis. Neil Dasgupta and Anish Tuteja provided guidance and support.

Chapter V was adapted from Bielinski, et al. 2019⁶ as well as yet to be published work. Ashley Bielinski developed the process for ALD BVO, constructed the ALD BVO photoelectrodes, and performed XPS, XRD, and SEM data collection and analysis. Sudarat Lee and Ashley Bielinski both performed and analyzed UV-vis, PEC, and quantum efficiency measurements. James Brancho and Samuel Esarey developed the Bi-precursor synthesis procedure from the published literature, assisted in the synthesis procedure, and consulted on process refinement for increased yield. Andrew Gayle performed and analyzed AFM measurements. Kai Sun provided TEM analysis. Neil Dasgupta and Bart Bartlett provided guidance and support.

CHAPTER II

Background

2.1 Nanowires for Solar Energy Conversion

Nanoscale materials are of interest for a variety of energy applications due to unique properties and effects that arise as a result of their geometry. Beneficial effects include light-trapping, high surface areas, improved transport phenomena, and reduced material usage. However, some of these same effects can be detrimental depending on the material and application. The high surface area, which can reduce local flux and provide space for increased catalyst loading, can also result in increased surface and interface recombination. Additionally, it can be difficult to manufacture nanomaterials, particularly with high throughput and on large substrate areas. Rational design of materials and interfaces is essential to optimize nanostructures for each unique application to maximize the beneficial properties while minimizing or ameliorating effects detrimental to device performance.

Semiconductor nanowires (NWs), in particular, represent a critical building block for nanoscale materials and systems owing to the novel optical, electronic, mechanical, thermal, and magnetic properties associated with a one-dimensional geometry.⁷ NW photonics have been investigated for a range of applications including detectors and sensors, waveguides, LEDs, lasers, and solar energy.^{7,8} NWs are confined in two dimensions, defined by the cross-section, but light and charge carriers are not geo-

metrically confined along the third direction, the length of the NW. For solar energy applications, one of the primary benefits for NW arrays is improved light absorption. This is a result of the anti-reflective properties of nanostructures that arise due to scattering and trapping of incident light. The characteristic length scales of nanostructures are often on the same order of magnitude or smaller than the wavelengths of visible light. If the nanostructure dimensions are similar to those of visible light, incident light may experience multiple internal reflections and scattering, reducing the reflectance and increasing the light absorption.^{9,10} Nanostructures with length scales shorter than the wavelength of the incident light interact in a fundamentally different way. The path the light travels is altered as it enters the structures as though there were a graded increase in refractive index rather than an abrupt interface. This substantially reduces the reflectivity of the surface.¹⁰ Sub-wavelength NWs can also exhibit optical resonances in the visible spectrum that confine light to the NW. At resonant wavelengths, light is effectively concentrated in the NW, which can exhibit absorption cross-sections greater than its geometric cross-section.^{7,11}

For applications to photocatalysis or photoelectrochemistry, increased surface area provided by nanostructures can help improve device kinetics. In these devices an overpotential is necessary to drive fast chemical reactions. The Butler-Volmer model for electrochemical reaction kinetics shows that higher overpotentials are required to drive a higher flux of redox events at an electrode surface.¹² Nanostructures such as NW arrays provide a high surface roughness. The higher local surface area reduces local surface flux while maintaining high flux with reference to the projected substrate area. Effectively, nanostructures allow the loading of more active surface reaction sites per unit substrate area, reducing the required turn over frequency at each site.¹³

While high surface area is beneficial for catalytic activity, it also results in increased surface recombination in nanostructured semiconductors. Control of nanostructure size and shape is an important research area enabling the optimization of the

nanostructure geometry to balance the effects of light absorption, catalytic activity and detrimental recombination effects.⁹

A particular structure of interest for solar energy conversion is the core-shell, or core-multishell NW. This architecture allows the separation of light absorption and carrier separation onto independent orthogonal directions, as shown in Figure 2.1. In traditional planar and thin-film architectures, the thickness of the semiconductor film must be optimized to maximize light absorption, while minimizing bulk recombination losses. This eliminated the possible use of many semiconductor materials such as metal oxide semiconductors, polycrystalline semiconductors, and lower purity materials, where the average carrier diffusion length is substantially shorter than the absorption depth for incident light.^{7,14} Core-shell NWs allow us to reconsider the use of materials in this category for solar applications.

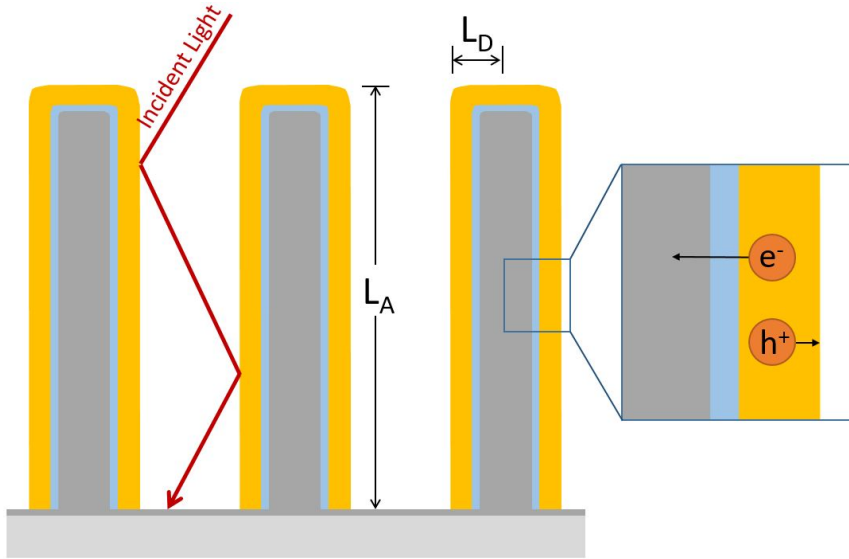


Figure 2.1: Core-shell-shell nanowire architecture showing the separation of light absorption depth, L_A , and charge carrier separation, L_D . The charge carrier separation is illustrated for a photoanode application showing the separation of holes to the electrode surface and electrons to a conductive nanowire core.

Similar to the consideration of increased surface recombination in semiconductor nanostructures, junction quality is crucial in core-shell NWs due to the high interface

area. When compared to the relatively small bulk material in a core-shell NW, the effects of surfaces and interfaces can dominate the performance of a device using this architecture. This emphasizes the need for systems level design that encompasses both the individual material components, but also interface design and optimization from the onset.¹

Compared to other solar energy technologies, a challenge unique to PEC is that many technologically relevant semiconductors, such as Si and GaAs, photocorrode when used as photoelectrodes for solar water splitting.¹⁵ One solution is to try to protect these materials¹⁵, while an alternative is to use metal oxide semiconductor photoelectrodes, which typically offer greater inherent stability. However, most metal oxide semiconductors have mid to wide bandgaps, which limits light absorption in the visible spectrum. Additionally, many metal oxide semiconductors suffer from poor optoelectronic properties, owing to high defect concentrations and low minority carrier diffusion lengths.^{16,17} Core-shell nanostructures can enable the use of many materials that are not candidates for planar solar energy architectures due to a mismatch in the optical and electronic properties. Chapter V shows how the performance of bismuth vanadate photoanodes can be improved using this approach.

2.1.1 Nanowire Geometry as a Model System

NW arrays provide an easily described geometry that is defined by the length, diameter, and orientation of the NWs relative to the substrate as well as the spacing between the NWs in the array. These parameters represent knobs that can be tuned to study the impact of structure variation on specific properties and applications.

A variety of synthesis approaches have been developed to form high-quality, single-crystalline NWs, including several bottom-up approaches based on solution or gas-phase processing.^{7,18} These approaches have several potential advantages over subtractive processes, including a reduced number of processing steps and complexity,

reduced raw material usage and cost, *in situ* doping, and the ability to create novel 3-D hierarchical and core-shell structures.¹⁹⁻³¹ However, the ability to control the morphology and relative angular orientation of bottom-up NW arrays over large areas and on a variety of substrates that have different geometric, chemical, and crystallographic properties is a key challenge limiting our ability to manufacture integrated nanosystems composed of heterogeneous materials.

As material systems continue to mature and gain complexity, methods are needed that can guide NW growth behavior on complex 3-D surfaces with deterministic and highly reproducible control. This process should be compatible with a wide range of substrate materials and should be arbitrarily scalable to facilitate manufacturing. To accomplish this, there are several typical methods of surface pretreatment involving either gas-phase or solution-based processing, including the formation of a thin-film, deposition of nanoparticles, and surface functionalization with organic components.^{7,18,26,32-34} However, these techniques often suffer from limitations that must be addressed. For example, process temperature, pressure, and chemical stability can limit the range of compatible substrates for pretreatments. Additionally, simultaneous control of the interfacial layer thickness, chemical composition, and crystallographic orientation is challenging, as it requires atomic-scale precision in synthesis over a macroscopic area. This can become even more problematic when attempting to coat non-planar and high-aspect-ratio structures, as small differences in these properties can lead to dramatic variations in the resulting NW morphology. A fundamental understanding of these morphological variations is not always understood, partially due to limitations in the ability to control the parameters of the deposited materials.

2.2 Zinc Oxide Nanowires

In the results presented in chapters III and IV, ZnO NWs were chosen as a model system to demonstrate the power of atomic layer deposition (ALD) seeding due to

their wide range of applications, including solar energy, photocatalysis, piezoelectric devices, nanophotonic structures, and sensors.^{7,35–37}

2.2.1 Properties and Applications of ZnO Nanowires

ZnO is a II-VI semiconductor material with a 3.37 eV direct bandgap and native n-type character. The most common, thermodynamically stable phase is the hexagonal wurtzite phase. It consists of alternating planes of O^{2-} and Zn^{2+} stacked along the c-axis, where each atom is tetrahedrally coordinated to four atoms of the other type. The Zn-O bond is largely ionic resulting in polar planes. Additional properties such as visible light transparency, high electron mobility, strong room-temperature photoluminescence, and piezoelectricity combine to make ZnO a popular material. ZnO has long been used in commercial applications, but more recently ZnO NWs have been developed for a range of technologies including NWs lasers,³⁷ dye-sensitized solar cells,³⁶ piezoelectric devices,³⁸ UV sensors,³⁹ and gas sensors.⁴⁰ Figure 2.2 shows the number of papers published on the topic of ZnO NWs from the years 2000-2018.

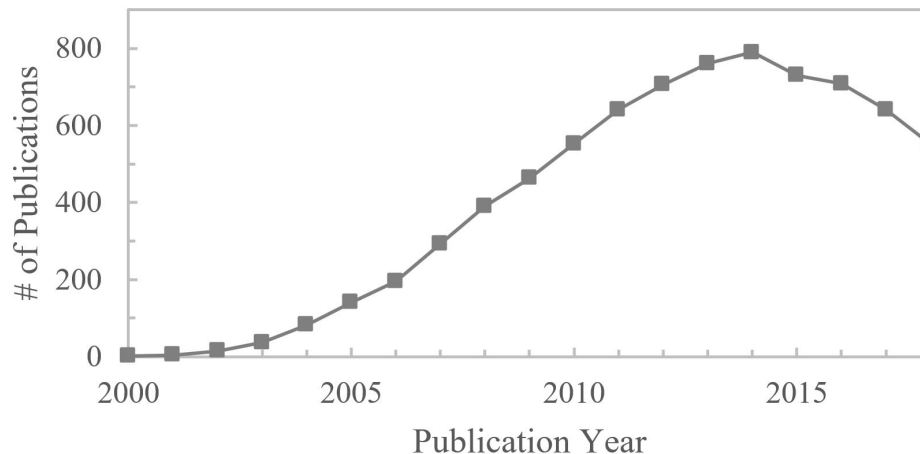
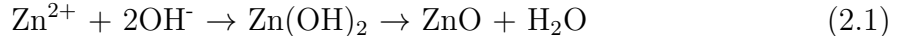


Figure 2.2: The number of papers published on ZnO nanowires since the year 2000 as determined by a Web of ScienceTM search for TOPIC: (ZnO nanowire) OR TOPIC: (zinc oxide nanowire).

2.2.2 ZnO Nanowire Synthesis

Bottom-up growth of crystalline ZnO NWs can be achieved by a variety of gas and liquid phase deposition techniques including chemical vapor deposition (CVD), physical vapor deposition (PVD), vapor-liquid-solid (VLS) or vapor-solid (VS), laser-assisted, template-assisted, or solution-based methods.^{41–48} The aqueous hydrothermal growth method, is attractive for its simple, low cost, low temperature, benign chemistry, and scalable synthesis.⁴⁹ Hydrothermal synthesis can be performed at temperature less than 100°C, which enables the use of a wide range of substrates. If a substrate with a close crystallographic match is used, NWs may grow directly on the substrate via homo- or heteroepitaxy,⁵⁰ which allows for lithographic patterning for ordered and oriented growth.^{51,52} However, to facilitate growth on an arbitrary substrate, a seed layer is necessary to promote heterogeneous nucleation of the NWs on the substrate.³²

The most common hydrothermal synthesis places a sample substrate in a heated solution of an alkaline reagent and a Zn²⁺ salt such as the mixture of hexamethylenetetramine (HMTA) and zinc nitrate. The hydrolysis of the Zn²⁺ salt in water is followed by the dehydration of the Zn hydroxyl species to form solid ZnO nuclei, as shown in Eq. 2.1. The alkaline reagent is used as the hydroxide source.⁴²



Due to the differing energies of the polar and non-polar crystal facets, ZnO crystals naturally grow most quickly along the c-axis. The relative growth velocities of the crystal faces are $V_{\langle 0001 \rangle} > V_{\langle 01\bar{1}\bar{1} \rangle} > V_{\langle 01\bar{1}0 \rangle} > V_{\langle 01\bar{1}1 \rangle} > V_{\langle 000\bar{1} \rangle}$, resulting in the elongated hexagonal morphology shown in Figure 2.3.⁵³ The addition of polyethyleneimine (PEI) to the hydrothermal growth solution can increase the crystal aspect ratio

by preferentially adsorbing to the non-polar side facets.⁵⁴ This enables the growth of higher aspect ratio NWs.

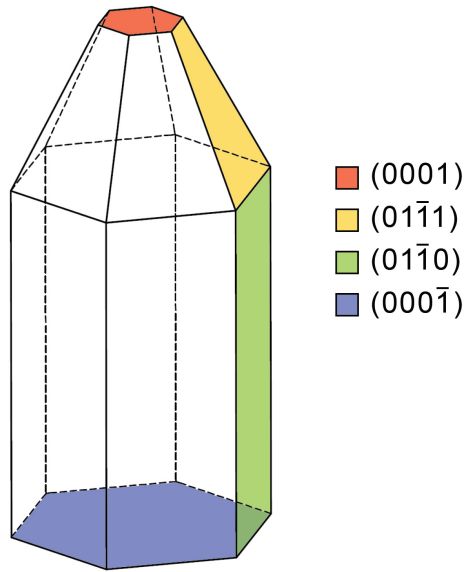


Figure 2.3: Crystal facets of hexagonal wurtzite ZnO and typical shape from accelerated growth along the c-axis.

2.3 Atomic Layer Deposition

ALD is a subcategory of chemical vapor deposition (CVD) based on sequential, self-limiting chemical reactions between precursor molecules and a surface, allowing for sub-nanometer precision in film thickness and composition without gradients over arbitrarily large areas.⁵⁵ This allows for conformal coating of ultrahigh-aspect-ratio structures ($>2000:1$).⁵⁶ Over half of the periodic table can be deposited using this method.^{57,58}

Figure 2.4a, shows one deposition cycle for a binary ALD process. A basic thermal ALD process uses two precursor gasses, though a greater number of precursors can be used for more complex film compositions. The ALD precursors are introduced in a temporal sequence to a deposition chamber under vacuum and purged with an inert gas. A typical ALD cycle contains the following four steps: 1) the introduction

and self-limiting chemisorption of a precursor gas on a substrate, 2) the purging of excess precursor gas and any reactant products with an inert carrier gas, 3) the introduction of the second precursor gas, which reacts with the adsorbed monolayer of the first precursor, and 4) the purge of excess precursor and reaction byproducts with an inert gas. An alternate form of ALD, spatial ALD (SALD) separates the precursors in space rather than time to increase deposition speeds and enable roll-to-roll manufacturing.^{59,60}

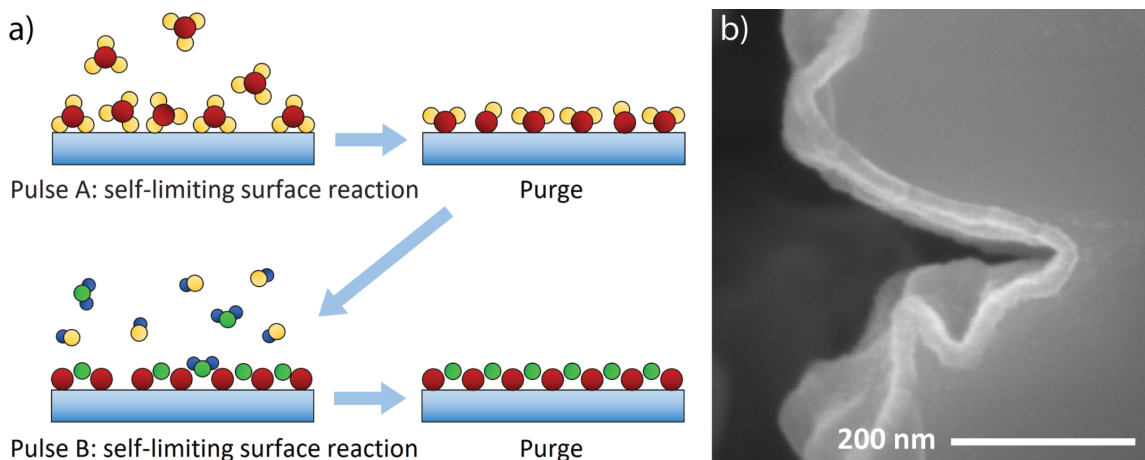


Figure 2.4: a) Diagram of one binary ALD cycle showing the reaction of precursor A with the substrate, the purge to remove excess precursor A and reaction products, the reaction of precursor B with precursor A on the substrate surface and the purge of excess precursor and reaction products. b) Cross-section SEM image showing a conformal film of ALD ZnO on etched GaP. Unlike line-of-sight limited processes, the nanoscale concave feature on the sidewall does not affect the film deposition for ALD. Adapted with permission from Lee, S.; Bielinski, A. R.; Fahrenkrug, E.; Dasgupta, N. P.; Maldonado, S. Macroporous P-GaP Photocathodes Prepared by Anodic Etching and Atomic Layer Deposition Doping. *ACS Appl. Mater. Interfaces* 2016, 8 (25), 16178–16185. Copyright (2016) American Chemical Society.

In the example of a metal oxide thermal ALD process, such as those presented in this thesis, one precursor is a metal compound and the second is an oxidizer such as water. The simplest ALD precursors are inorganic, typically metal-halide molecules such as TiCl_3 . More common are metal-organic precursors including those with sim-

ple ligands such as alkyls, for example trimethylaluminum, or any number of more complex organic components, such as the Bi-alkoxide precursor discussed in Chapter V.⁶¹ ALD precursor molecules are chosen or designed to fulfill a number of required properties such as vapor pressure, thermal stability, and self-limiting reactivity with substrate surfaces and the co-reactant precursor. A well behaved ALD precursor must exhibit stable, self-limiting growth within the ALD window. The ALD window, Figure 2.5, is the range of temperature conditions under which film growth is stable with a constant, uniform growth rate per cycle across the substrate area.

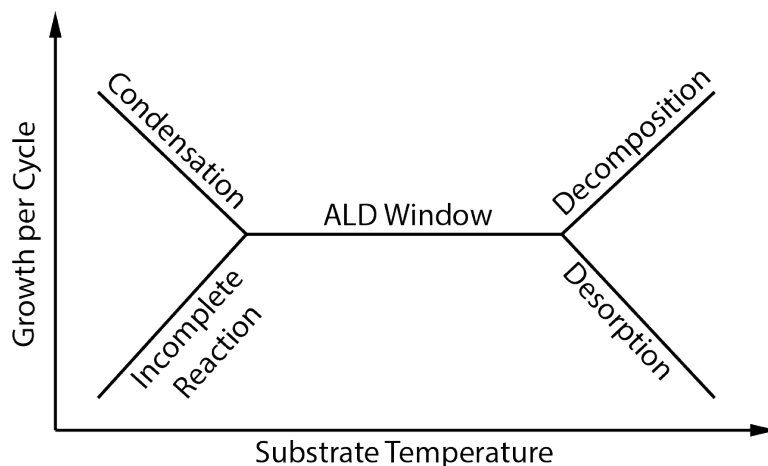


Figure 2.5: Temperature window for self-limiting ALD growth.

2.3.1 Deviations from Ideal ALD

While a simple textbook ALD process exhibits perfect layer-by-layer film growth with constant linear growth rates across the ALD window, nearly all ALD processes deviate from this ideal to varying extents. Some common variations include film nucleation effects, rough films or discrete island growth modes, and non-stoichiometric compositions.^{55,62–64}

Despite the name “atomic layer deposition” one ALD cycle does not deposit one atomic layer of the target material. Instead, a fraction of a layer is deposited due to steric hindrance of the ligand groups when the precursor molecules adsorb on a

surface.⁶¹ Availability of reactive surface groups can also affect the material deposited with each ALD cycle. During steady state growth, the material is growing on an existing layer of itself and therefore has a constant surface environment and linear growth rate. However, the initial ALD cycles when the film is nucleating on a heterogeneous substrate surface can lead to higher or lower initial growth rates.⁶³

The steady state growth rate can also vary with temperature within the ALD window. This results from changing saturation conditions for the precursor adsorption on the substrate surface. For example, increased temperatures may reduce the number of reactive surface sites, but they may also improve the kinetics of certain adsorption reactions resulting in a possible decrease or increase of the per cycle growth rate respectively.⁶¹ The observed growth rate is the balance of many such effects.

The morphology of the deposited film can change depending on factors such as the number of reactive surface sites available on the substrate vs. the deposited material, energetically favorable growth in certain crystalline directions, or defects in the substrate surface. In layer-by-layer growth (Frankvan der Merwe growth), each monolayer is completed before the next is formed.^{55,61} Alternatively, the ALD material may grow more favorably on itself resulting in an island (Volmer-Weber) growth mode. Islands can also form if the surface atoms are mobile and the island morphology results in a lower system energy.^{64,65}

While ALD can coat ultra-high aspect ratio structures, the deposition conditions must be optimized to overcome mass transport limitations. The precursor exposure time must be sufficient for the precursor molecules to fully diffuse into any structure of interest.^{55,56,66} Precursor properties such as molecule size and reaction rate further influence the necessary precursor exposure time for these structures.

Even well behaved processes can contain trace contamination from precursor ligands that were not fully removed. Carbon, hydrogen, and nitrogen can be incorporated from organic ligands, particularly when there is a small temperature gap

between the ALD window and the decomposition temperature of the precursor compound.⁶¹ Understanding the behavior of an ALD process under different conditions is an important step towards using ALD as a diverse tool for surface modification.

2.3.2 Atomic Layer Deposition for Surface and Interface Modification

ALD possesses key characteristics that make it a powerful tool for modifying surfaces and interfaces. It is a conformal deposition process that is not line-of-sight limited. This enables ALD to uniformly coat even complex 3D nanostructures, which is difficult for solution based processes or directional film deposition such as sputtering or evaporation. ALD also provides angstrom-scale control of film thickness and the chemisorption reaction process of the ALD precursors results in a strongly adhered film.^{55,67} These properties enable a delicate balance of film performance such as providing a pinhole free protective film, a carefully controlled tunnel barrier, or an active co-catalyst film that does not block light.^{15,68,69}

2.3.3 Atomic Layer Deposition for Energy Conversion

Despite these advantages, there have been relatively few reports on the use of ALD to control the properties of heterogeneous interfaces in hierarchical nanomaterials, and the underlying structural and chemical relationships between the interfacial layers and resultant nanostructures have not been investigated in detail.^{13,70-75} To this end, ALD provides a platform for both fundamental research on the mechanisms of heterogeneous nucleation and growth control through surface modifications, as well as a versatile manufacturing tool capable of creating complex integrated nanoscale systems that would be difficult to fabricate using traditional processes.

ALD has been demonstrated as an enabling technique to precisely control the composition and structure of electrode-electrolyte interfaces in a wide range of electrochemical energy conversion and storage applications, including batteries, fuel cells,

electrocatalysts, and photoelectrochemical cells.^{15,76–78} The ability to make nanometer-thick dense, pin-hole free films over large surface areas has made ALD an attractive option for surface passivation, control of charge transport, and chemical protective layers in photovoltaic (PV) cells, dye sensitized solar cells, fuel cells, photoelectrochemistry, and batteries.^{79–87} Similarly, ALD has been used to deposit islands or non-continuous films for co-catalyst loading, quantum dots, and surface passivation in a range of solar energy and catalysis applications.^{88–91}

2.4 Structural Wettability

2.4.1 Liquid Contact Angles on Planar Surfaces

A liquid droplet on a smooth, chemically homogeneous surface exhibits a characteristic Young's contact angle (θ) between the horizontal liquid-solid interface and the liquid-air interface, determined by the minimization of free energy, shown in Figure 2.6.⁹² Equation 2.2 shows the relation between the contact angle, the liquid-gas interfacial energy γ_{LG} (also commonly referred to as the surface tension of the liquid), the interfacial energy between the liquid droplet and the solid surface γ_{SL} , and the solid-gas interfacial energy γ_{SG} (also commonly referred to as the surface energy of the solid).⁹³

$$\cos \theta = \frac{\gamma_{SG} - \gamma_{SL}}{\gamma_{LG}} \quad (2.2)$$

The wettability of a surface is also frequently described by a second parameter, contact angle hysteresis, which is the difference in the maximum (advancing) contact angle and the minimum (receding) contact angle in dynamic measurements. Contact angle hysteresis is a measure of the energy that is dissipated when a liquid droplet moves on a solid surface.⁹³ In simple terms, a droplet with a low contact angle and

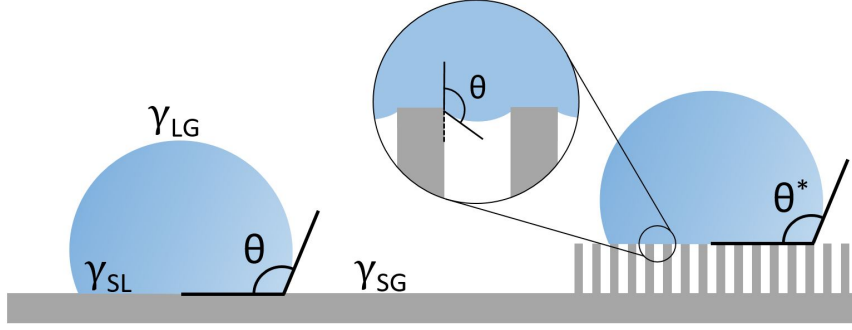


Figure 2.6: Young’s contact angle, θ , on a planar surface (left) and apparent contact angle, θ^* , on a structured surface (right), with center inset showing local Young’s contact angle on the textured surface.

high hysteresis will stick to a surface, while a droplet with low hysteresis and high contact angle will easily roll off the surface.

2.4.2 Liquid Contact Angles on Nano- and Microstructured Surfaces

On a rough substrate, liquids exist in one of two configurations. The liquid may penetrate between the surface features, yielding a fully wetted interface, frequently referred to as the Wenzel state.⁹⁴ The apparent macroscopic contact angle, θ^* , in the Wenzel state is a function of the equilibrium Youngs contact angle, θ , and the roughness, r :

$$\cos \theta^* = r \cos \theta \quad (2.3)$$

If the surface roughness is sufficiently high, air can be entrapped beneath the liquid, forming a composite solid-liquid-air interface, called the Cassie-Baxter state. The apparent contact angle for a composite interface is calculated using the Cassie-Baxter equation,⁹⁵ given as

$$\cos \theta^* = r_\phi \phi_s \cos \theta - (1 - \phi_s) \quad (2.4)$$

Here, ϕ_s is the projected area of the wetted solid divided by the total projected area, and r_ϕ is the roughness of the wetted solid. Whether a liquid will adopt a fully wetted or a composite interface with a given surface is determined by the overall free energy of the system.⁹⁶⁻⁹⁹ Very high contact angles ($>150^\circ$) with both high and low surface tension liquids are possible only in the Cassie-Baxter state and are obtained by maximizing the areal fraction of the air/vapor pockets within the composite interface ($1 - \phi_s$ in Eq. 2.4).⁵

Rough surfaces featuring hierarchical scales of texture are critical for achieving very high contact angles while maintaining a stable and robust composite interface. The porosity of the largest texture scale determines the robustness of the Cassie-Baxter state or its resistance to liquid impingement under pressure. As a consequence, adding multiple levels of texture reduces ϕ_s without compromising the surfaces robustness against wetting.^{5,93,96,100}

2.4.3 The Effects of Nanostructures on Contact Angle and Composite Interface Robustness

To characterize the porosity of disparate nanostructured surfaces, we use the spacing ratio D^* .¹⁰¹ D^* is effectively the inverse of the solid contact area ϕ_s , and in the case of these hierarchical arrays in Chapter IV, it is given as

$$D^* = \frac{4}{\pi} \left(\frac{(R + D)^2}{R^2} \right) \quad (2.5)$$

Here, R and D are the radius of the nanowires and edge-to-edge nanowire spacing, respectively. The apparent contact angle, θ^* , on a composite interface increases with increasing values of D^* . This is typically accompanied by a simultaneous reduction in the contact angle hysteresis. The Cassie-Baxter equation (Eq 2.4) can be rewritten

in terms of the spacing ratio as

$$\cos \theta^* = -1 + \frac{1}{D^*}(1 + r_\phi \cos \theta) \quad (2.6)$$

A dimensionless design parameter, the robustness factor, A^* , was developed by Tuteja, et al.¹⁰¹ to characterize the robustness of composite interfaces. It is defined as $A^* = P_b/P_{ref}$.^{93,101,102} The breakthrough pressure, P_b , is defined as the applied pressure at which a given composite interface is disrupted by sagging of the liquid-vapor interface to the point that it displaces the air pockets and irreversibly wets the surface texture. P_{ref} is a characteristic reference pressure, given as $P_{ref} = 2\gamma_{LV}/l_{cap}$. Here, $l_{cap} = \sqrt{\gamma_{LV}/\rho g}$, where γ_{LV} is the surface tension of the liquid, ρ is the fluid density, and g is the acceleration due to gravity. P_{ref} is close to the minimum pressure exerted by macroscopic liquid droplets or puddles.

For the purposes of estimating robustness, the geometries produced in Chapter IV may be approximated as micro-hoodoos,⁵ which are posts with overhanging horizontal caps.¹⁰² As previously derived,^{5,101} the robustness factor A^* for microhoodoos may be calculated as

$$A^* \approx \left(\frac{1}{H^*} + \frac{1}{T^*} \right)^{-1} \quad (2.7)$$

where

$$H^* = \frac{2R_{edge}l_{cap}\cos\theta}{D^2(1+\sqrt{D^*})} \left((1-\cos\theta) + \frac{H}{R_{edge}} \right) \quad (2.8)$$

$$T^* = \frac{l_{cap}\sin(\theta - \Psi_{min})}{D(1+\sqrt{D^*})} \quad (2.9)$$

where R_{edge} is the radius of curvature of the edge of the overhanging surface, D is the edge-to-edge spacing between post tops, R is the radius of the hoodoo caps, D^* is the spacing ratio defined in Eq 2.5, and Ψ_{min} is the minimum texture angle for a given surface, which is defined from the horizontal such that it is 90° for a vertical wall and 0° for the bottom of an overhang on a micro-hoodoo.

It has been shown that the A^* parameter is capable of providing an *a priori* estimation of the stability of the composite Cassie-Baxter state on various textured surfaces.^{101,102}

2.5 Photoelectrochemistry

Solar energy is an abundant source of renewable energy and an important component in the transition away from fossil fuels. However, the intermittent availability of the solar resource, due to factors such as seasonal changes or local cloud cover, is a major challenge as it begins to contribute a larger fraction of the global energy demand.¹⁰³ Photoelectrochemistry (PEC) is one route to harnessing solar energy and storing it in chemical bonds. In many cases, chemical fuels are easier to store than electricity, allowing us to collect solar energy when it is available, and use it when the demand arises.¹⁰⁴

PEC is the use of light-generated excited charge carriers at a semiconductor-liquid interface to drive redox chemical reactions involving species in the liquid. The study of PEC systems brings together concepts from the fields of surface science, electrochemistry, solid-state physics, and optics. A summary of the basic principles of PEC is presented by Peter (2016) with references to more detailed discussions of the fundamental concepts.¹⁰⁵ The essential concepts for understanding the PEC data presented in Chapter V are briefly reviewed below.

2.5.1 Semiconductor-Liquid Junctions

Consider a semiconductor not in contact with a liquid electrolyte, as shown in Figure 2.7a. The semiconductor has valence band energy, E_{VB} , conduction band energy, E_{CB} , and Fermi level, E_F . The Fermi level is the electrochemical potential of electrons in the material and in Figure 2.7 it is shown shifted towards E_{CB} due to n-type doping. The electrolyte in Figure 2.7 contains a redox couple (A/A^-) with a redox potential, $E(A/A^-)$, within the semiconductor's band gap.

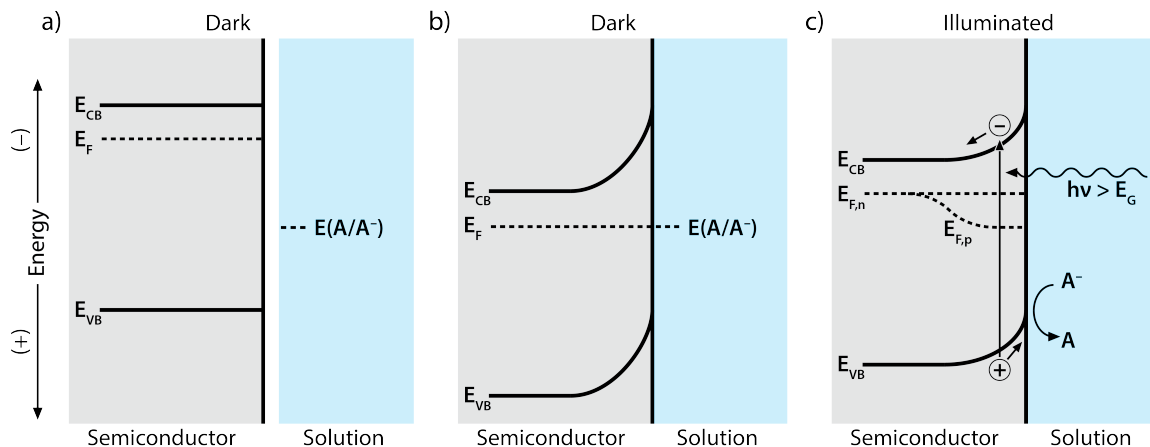


Figure 2.7: Electronic band structure for an n-type semiconductor and a liquid electrolyte showing a) electronic states before semiconductor-liquid contact, b) electronic states after semiconductor-liquid equilibration, and c) electronic states when illuminated.

When the semiconductor and electrolyte are brought into contact, a transfer of electrons will occur until thermodynamic equilibrium is achieved, shifting E_F to match $E(A/A^-)$. With the energy levels as they are drawn in Figure 2.7, electrons transfer from the semiconductor to the electrolyte creating a positive space charge region from the ionized atoms at the semiconductor interface. This space charge region generates an electric field, which in turn causes a variation in electrical potential near the semiconductor interface, shown by the upward curvature of E_{VB} and E_{CB} in Figure 2.7b. The electrostatic potential of this generated field balances the initial difference between the electrochemical potentials of the semiconductor and the elec-

trolyte. This band bending creates a potential energy barrier for electron transfer from the electrolyte to the semiconductor, but allows electrons to flow freely in the other direction.^{105,106}

2.5.2 Illuminated Semiconductor-Liquid Junctions

The illumination of a semiconductor with photon energy $h\nu > E_{gap}$, where $E_{gap} = E_{CB} - E_{VB}$, excites electrons from the valence band to the conduction band. Steady state illumination pushes the electron and hole populations in the conduction and valence band away from thermodynamic equilibrium. While the electrons and holes are not in thermal equilibrium with each other, they do quickly reach thermal equilibrium with the semiconductor lattice phonons. This is because the thermalization of the excited electron happens on a much faster time scale than carrier recombination.¹⁰⁶ In this state of quasi-thermal equilibrium the electrons and holes have different electrochemical potentials. Figure 2.7c shows how this results in the splitting of the semiconductor Fermi level near the interface into separate quasi-Fermi levels for electrons and holes. The difference in the quasi-Fermi levels for electrons and holes is the open circuit voltage, V_{OC} , generated when there is no current flow. The open circuit photovoltage determines what reactions can be driven. Thermodynamically, the standard potential for the reduction of A to A^- , $E^\circ(A/A^-)$, must be less than V_{OC} for the reaction to proceed.¹⁰⁶ In practice, there are additional kinetic barriers so the V_{OC} must sometimes be substantially larger than the reaction potential.

The electron-hole pairs generated by this process have a limited lifetime of milliseconds to nanoseconds before they recombine.¹⁰⁵ The band bending that was generated when the semiconductor and electrolyte were brought into contact helps to separate electron-hole pairs generated in or near the space charge region before they recombine. The minority carrier, the hole in the example case of an n-type semiconductor, is driven by the electric field towards the semiconductor electrolyte interface

whereas the majority carrier, in this case the electron, is driven into the bulk of the semiconductor.

Holes that successfully reach the interface can accept electrons from solution species, driving an oxidation reaction. However, if charge transfer is slow, the holes can build up at the interface, affecting the electric field strength. The interface can also be a detrimental location for carrier recombination.^{106,107} At the atomic scale, the electronic properties of the semiconductor surface differ from the bulk due to surface terminations such as dangling bonds, surface reorganization, or binding to solution species. This can result in allowed electronic states within the band gap.¹⁰⁸ These “trap states” can increase surface recombination and cause Fermi level pinning.^{109,110} These effects are particularly important for high surface area nanostructured photoelectrodes.

2.5.3 PEC Experiments in a 3-Electrode Half Cell

The photoelectrochemical splitting of water into hydrogen and oxygen, Eq. 2.10, has a standard potential of $E^\circ = 1.23 \text{ V}$.¹⁰⁶



In order to provide that thermodynamic driving force along with kinetic over potentials, a wide band gap semiconductor is necessary to achieve unassisted solar water splitting at a single photoelectrode. The use of wide band gap semiconductors limits the overall solar-to-fuel conversion efficiency due to the lower intensity UV portion of the solar spectrum, Figure 2.8. An alternate approach uses a dual light-absorber where the oxygen evolution reaction (OER) and hydrogen evolution reaction (HER) are split onto a separate n-type photoanode and p-type photocathode respectively.^{16,112} This enables the use of smaller band gap semiconductors that

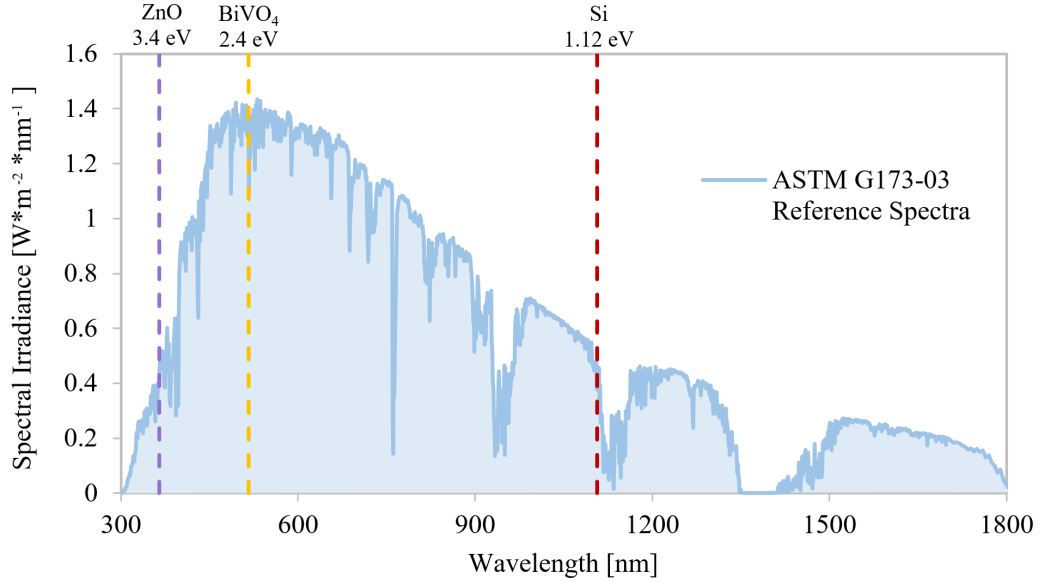
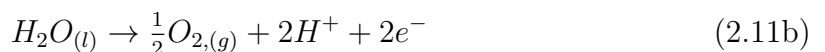


Figure 2.8: The air mass 1.5 G solar spectrum from the ASTM G-173 standard showing solar irradiance of earth’s surface at sea level through 1.5 equivalent atmospheres corresponding to a sun zenith angle of 48.2° . Total irradiance that can be absorbed by a semiconductor is the area under the curve integrated from zero to the bandgap. Bandgaps for ZnO, BiVO₄, and Si are shown for reference. Spectrum data from NREL.¹¹¹

can absorb a larger portion of the solar spectrum. This type of cell architecture, commonly referred to as a z-scheme, is inspired by the two photon absorption process in natural photosynthesis.¹⁶ The two photoelectrodes are connected in series via an ohmic contact. The minority carriers excited at each photoelectrode are used in the photocatalytic reaction and the majority carriers recombine at the junction between the two electrodes. In the case of water splitting, the HER (Eq. 2.11a) occurs at the photocathode and the OER (Eq. 2.11b) occurs at the photoanode. This approach also provides spatial separation of the H₂ and O₂ product gasses. The HER and OER half reactions are shown below and when combined they are equivalent to the full water splitting reaction, Eq. 2.10.



In research it is common to independently study only one of the photoanode or photocathode at a time in order to isolate the performance of the associated semiconductor, interfaces, and co-catalysts. Figure 2.9 shows a typical three-electrode PEC half cell of the type used to study the photoanodes in Chapter V. A semiconductor working electrode is paired with a counter electrode and reference electrode. This type of cell can be used to determine many of the properties discussed in subsection 2.5.2. For example, the open circuit voltage, V_{OC} , when the working electrode is illuminated is a measurement of the difference between the electron and hole quasi Fermi levels. A potentiostat can be used to control the voltage of the the working electrode relative to the fixed voltage of the reference electrode. This enables linear sweep voltammetry and quantum efficiency measurements such as those shown in Figures 5.9 and 5.14.

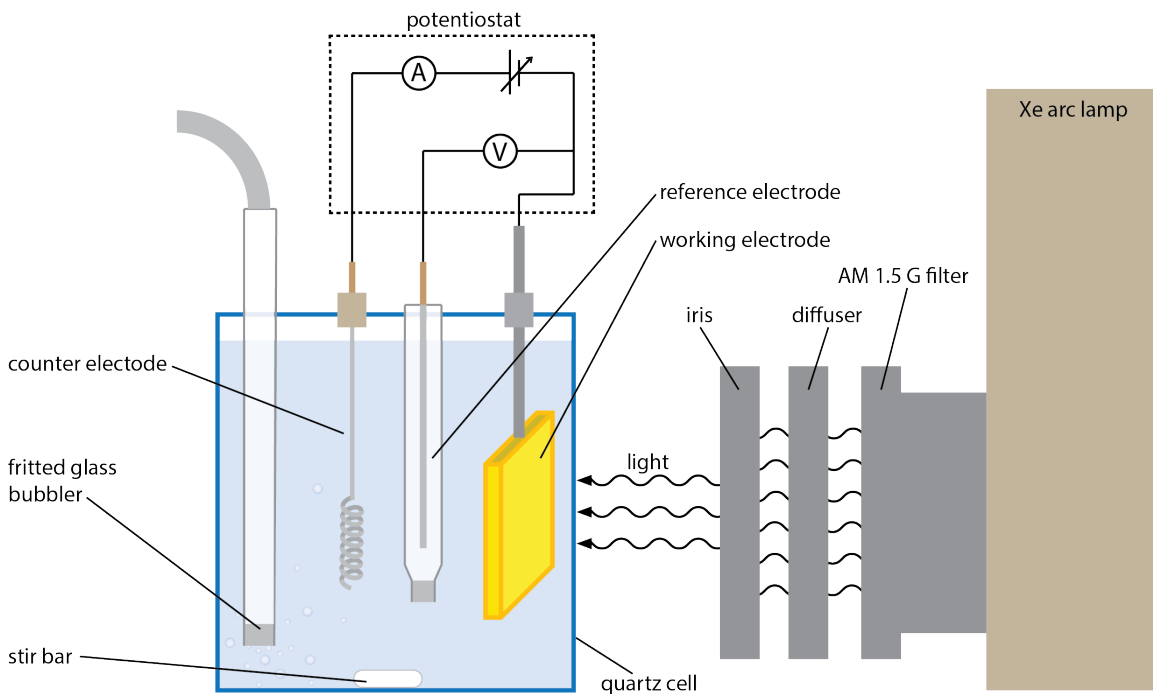


Figure 2.9: PEC experimental setup for 3-electrode half cell measurements.

The potential in a three-electrode cell is controlled relative to a reference electrode. The role of the reference electrode is to provide a known constant electrochemical

potential. The reference electrode used for PEC measurements reported here was Ag/AgCl immersed in 3 M NaCl. The potential of the working electrode relative to the reference electrode can be converted to the reversible hydrogen electrode (RHE) scale using the Nernst equation, as shown in Eq. 2.12a, using the pH of the electrolyte and the potential of the reference electrode, $E_{ref} = E_{Ag/AgCl, 3M NaCl}$.

$$E \text{ (vs. RHE)} = E \text{ (vs. Ag/AgCl)} + 0.059 V \times \text{pH} + E_{ref} \quad (2.12a)$$

$$E_{Ag/AgCl, 3M NaCl} = 0.209 V \text{ vs. NHE at } 25^\circ\text{C} \quad (2.12b)$$

Conversion to the RHE scale simplifies interpretation of the HER and OER redox potentials and comparisons of photocurrents across published literature where different electrolyte solutions and reference electrodes are used.

2.5.4 PEC Experimental Techniques

There are three main types of PEC measurements presented in this thesis: linear sweep voltammetry (LSV), quantum efficiency (QE), and chronoamperometry (CA). All three were performed in 3-electrode cells, as shown in Figure 2.9.

A LSV measurement is performed by applying a range of electrical potentials to the working electrode relative to the constant potential of the reference electrode. The potential is changed at a constant rate and the corresponding current between the working and counter electrodes is measured. For PEC, the LSV can be collected in the dark or with the working electrode illuminated. The current can be used as a measure of the reaction rate at the photoelectrode. In the case of a photoanode for water splitting, Eq. 2.11b shows that for every molecule of O₂ generated, 4 electrons are transferred from the solution species to the photoanode, which corresponds to the hole transfer to the semiconductor-solution interface in Figure 2.7c.

QE measurements probe the fraction of incident photons on the electrode surface that are converted into excited charge carriers and that are successfully separated and collected as a function of the wavelength of the incident light. External QE for a photoelectrode, also known as incident photon to current efficiency (IPCE) is defined as:

$$\text{IPCE} = \frac{\text{electrons generated}}{\text{incident photons}} = \frac{j(\text{mA}/\text{cm}^2) \times 1239.8}{\lambda(\text{nm}) \times P_{in}(\text{mW}/\text{cm}^2)} \quad (2.13)$$

where j is the spectral photocurrent, P_{in} is the power of the incident light for the given wavelength, and 1239.8 is a conversion factor relating the energy of a photon in eV, E , to its wavelength in nm, λ . This factor is calculated from, $E = hc/\lambda$ where $E(\text{eV})/\lambda(\text{nm}) = hc = 1239.8(\text{eV nm})$, where h and c are Planck's constant and the speed of light, respectively. Some of the light incident on a photoelectrode is reflected or transmitted so another metric of interest is internal quantum efficiency, or absorbed photon to current efficiency (APCE). APCE is calculated by dividing the IPCE by the absorption spectra of the photoelectrode, as shown in Eq. 2.14.

$$\text{APCE} = \frac{\text{IPCE}(\lambda)}{A(\lambda)} \quad (2.14)$$

CA measurements, specifically controlled-potential chronoamperometry, apply a potential step to the working electrode and then measure how the photocurrent varies with time. In the case of PEC water splitting, CA is commonly used to measure the stability of photoelectrodes. The illumination and current flow simulate operating conditions for a solar PEC cell.

CHAPTER III

ZnO Nanowire Growth with Tunable Orientation Using Atomic Layer Deposition Seeding

Adapted with permission from Bielinski, A. R.; Kazyak, E.; Schlepütz, C. M.; Jung, H. J.; Wood, K. N.; Dasgupta, N. P. Hierarchical ZnO Nanowire Growth with Tunable Orientations on Versatile Substrates Using Atomic Layer Deposition Seeding. *Chem. Mater.* 2015, 27 (13), 4799-4807. Copyright 2015 American Chemical Society.

The ability to synthesize semiconductor nanowires with deterministic and tunable control of orientation and morphology on a wide range of substrates, while high precision and repeatability are maintained, is a challenge currently faced for the development of many nanoscale material systems. Here we show that atomic layer deposition (ALD) presents a reliable method of surface and interfacial modification to guide nanowire orientation on a variety of substrate materials and geometries, including high-aspect-ratio, three-dimensional templates. We demonstrate control of the orientation and geometric properties of hydrothermally grown single crystalline ZnO nanowires via the deposition of a ZnO seed layer by ALD. The crystallographic texture and roughness of the seed layer result in tunable preferred nanowire orientations and densities for identical hydrothermal growth conditions. The structural and chemical relationship between the ALD layers and nanowires was investigated with synchrotron x-ray diffraction (XRD), high-resolution transmission electron mi-

croscopy, and x-ray photoelectron spectroscopy (XPS) to elucidate the underlying mechanisms of orientation and morphology control. The resulting control parameters were utilized to produce hierarchical nanostructures with tunable properties on a wide range of substrates, including vertical micropillars, paper fibers, porous polymer membranes, and biological substrates. This illustrates the power of ALD for interfacial engineering of heterogeneous material systems at the nanoscale, to provide a highly controlled and scalable seeding method for bottom-up synthesis of integrated nanosystems.

3.1 ALD Films for Heterogeneous ZnO Nanowire Nucleation

Herein, we provide an in-depth mechanistic study of the use of ALD seed layers to tune the morphology and relative angular orientation of hydrothermally grown ZnO NWs. By varying the thickness of the ALD seed layers, we demonstrate that the NW orientation and density can be tuned in a highly repeatable manner. This behavior has been evaluated through a statistical analysis of the resultant morphology using cross-sectional scanning electron microscopy (SEM), transmission electron microscopy (TEM), x-ray photoelectron spectroscopy (XPS), and synchrotron x-ray diffraction (XRD). The X-ray data allow for a quantitative analysis of the NW texture and crystallographic properties and demonstrates their orientation relationship with respect to the substrate and the interfacial ALD seed layer. These complementary techniques allow us to observe the evolution of the structural and morphological parameters of the ALD seed layer and to correlate them quantitatively to the density and orientation dependence of the resultant NWs.

A number of publications^{46,72,113,114} have investigated how to optimize seeding and growth parameters for perpendicular NW growth. In these publications, NW orientation is usually qualitatively grouped into two categories, either oriented or disoriented, or represented by a single roughness value. We expand this investigation by

demonstrating that perpendicular NWs are not the only form of order and that textured polycrystalline seed layers fabricated by ALD can produce distinct and highly controllable preferred orientations at acute and right angles relative to the substrate. To identify and quantify these nonperpendicular preferred orientations we employ a statistical analysis of cross-sectional SEM images combined with synchrotron X-ray analysis to correlate the crystallographic properties of the seed layers and resulting NWs.

To demonstrate the full power of this NW growth technique using ALD surface directed assembly, Figure 3.1, hierarchical structures were fabricated by growing highly conformal ZnO NWs with controlled geometric parameters on a variety of high surface area 3-D templates, including microposts, paper fibers, porous polymer membranes, and even biological materials. The tunable control of NW orientation and morphology using the ALD seed layer is maintained independent of the substrate geometry. The versatility of this process, combined with the conformal and highly controlled nature of ALD deposition, enables the fabrication of hierarchical and heterogeneous nanosystems with an unparalleled degree of control, uniformity, and reproducibility. This is critical to the future of nanoscience, as systems-level engineering principles are incorporated in the design of complex materials, requiring deterministic control of relative feature geometries and interfacial properties to provide targeted functionality.¹ Importantly, these complex hierarchical materials can be fabricated using low-temperature, scalable, and completely bottom-up processing, without the need for expensive and time-consuming lithography or clean-room processes.

A number of seed layer deposition methods have been developed for ZnO, the most common of which are the thermal decomposition of a Zn solution to form ZnO¹¹⁵ and the deposition of a colloidal solution of ZnO nanoparticles.³⁶ ZnO adopts the wurtzite crystal structure, and hydrothermally grown ZnO NWs are known to grow preferentially along the [002] direction to minimize the free energy of the system. It

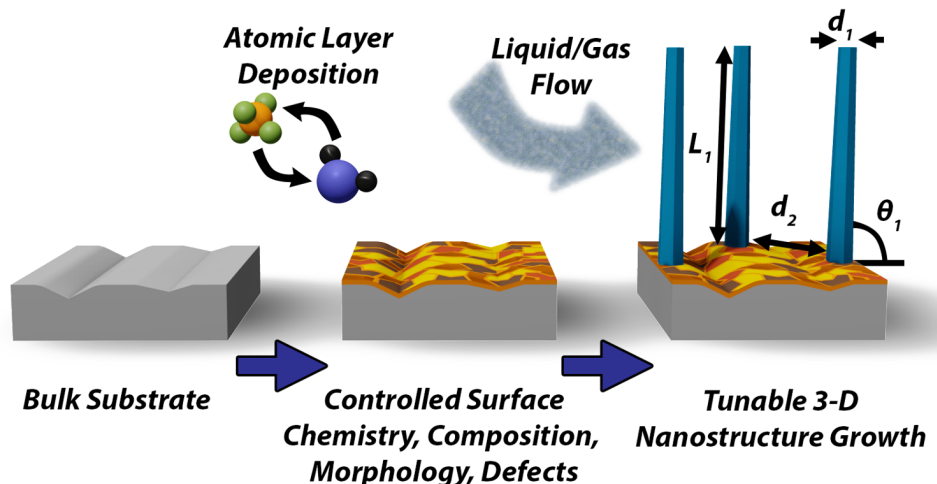


Figure 3.1: Diagram of surface directed assembly using ALD to control the geometric parameters of heterogeneous nanowire independent of the substrate.

is well-accepted that by starting with (002) oriented grains, perpendicularly oriented NW arrays can be grown.³² Here, we extend this concept to demonstrate that precise control of the seed layer crystallographic texture in polycrystalline films can be used to deterministically tune the resulting orientation of the NWs relative to the substrate at a variety of nonperpendicular angles. However, controllable variation of these crystallographic properties requires atomic-scale control of film deposition, which is difficult to achieve using traditional techniques, especially when coating three-dimensional surfaces. We show that ALD provides a versatile technique to address this challenge, as demonstrated by control of NW-substrate orientation relationships in three dimensions.

3.1.1 Control of Nanowire Orientation

Figure 3.2 shows a series of cross-sectional SEM images of ZnO NWs grown on planar Si substrates with ALD seed layers of different thicknesses. Identical hydrothermal growth parameters were used for each sample. The thickness of the seed layers is linearly dependent on the number of ALD cycles, with a constant growth rate of 1.92 Å/cycle (Appendix A, Figure A.1). Also included in Figure 3.2 are his-

tograms of NW orientation relative to the substrate extracted from the images. The image analysis displays a distinct three-part trend in NW out-of-plane orientation as a function of the ALD seed layer thickness. Starting from thinnest and moving to thicker seed layers, the three regimes observed are a preferred acute angle, perpendicular orientation, and a bimodal angular distribution. In the acute angle region (Figure 3.2, 15-30 cycles) the preferred angle increases with increasing seed layer thickness until it reaches a perpendicular condition. From the perpendicular orientation region (Figure 3.2, 100 cycles), as seed layer thickness increases, a secondary bimodal orientation begins to emerge at around 200 cycles and grows stronger until it is dominant in the 600-cycle sample. In the bimodal distribution (Figure 3.2, 300 and 600 cycles) some of the NWs are perpendicular and others have a preferred low-angle orientation. These trends were reproducible, and the continuity of the trends across different sample thicknesses indicates that none of the observed results were outliers.

Additional trends occur with the NW diameter. The trend in diameter is hypothesized to be a result of the NW density. High density causes a steric hindrance in radial growth, decreasing the average NW diameter. A higher density also limits mass transport in the growth solution around the NWs, causing the solution in those regions to deplete more quickly. Lower density NWs are less affected by mass transport limitations, leading to faster growth in all dimensions.

The SEM images do not provide in-plane orientation data, and the quantitative out-of-plane orientation data are limited by the sample size and projection of the three-dimensional NWs onto a 2-D image. Therefore, synchrotron X-ray diffraction was employed to quantify the observed out-of-plane orientation trends at an ensemble level and to investigate in-plane orientation. Out-of-plane orientation was measured using χ (tilt) scans, and in-plane orientation was measured using φ (rotation). In both cases, the incident beam and detector were fixed at symmetric angles such that

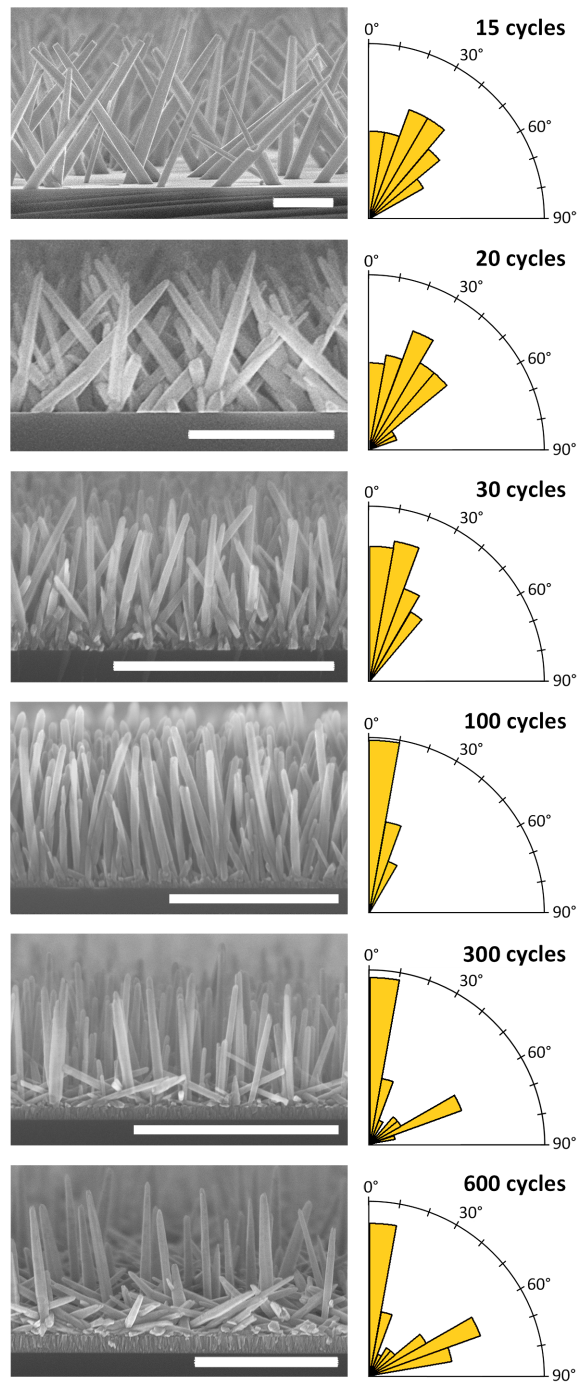


Figure 3.2: Cross-sectional SEM images and corresponding orientation histograms of NWs grown on different seed layer thicknesses. All other variables were held constant. Scale bar = 2 μm , except 100 and 300 cycles, where scale bar = 1 μm .

the three strongest ZnO diffraction peaks could be recorded on the area detector. These three peaks correspond to the (100), (002), and (101) planes.

For all samples, the φ scan data exhibited no significant variation in intensity, Figure 3.4a, indicating that neither the seed layers nor NWs show preferential in-plane orientation. In contrast, the χ scan data showed variation in intensity as a function of the χ angle, indicating a clear trend in the preferential out-of-plane orientation in the NWs (Figure 3.3a), in agreement with the SEM analysis. The χ and φ scans are sections of a pole figure, measuring intensity along certain constant-variable lines. However, since initial full pole figures, Figure 3.4b, showed no preferred in-plane orientation, only φ scans at $\chi = (002)$ peak maximum and χ scans at $\varphi = 0^\circ$ were conducted for subsequent samples.

To correlate the orientation dependence of the NWs with the interfacial ALD seed layers, synchrotron diffraction measurements were also performed on ALD films without hydrothermal growth (Figure 3.3c). The 30-, 100-, and 600-cycle samples were used to determine the relationship between the seed layer and NWs. Diffraction data for the 15- and 20-cycle thin films are not included in Figure 3.3 because we were unable to observe a measurable signal above the background for these samples. This problem would be exacerbated by the peak widening that occurs as a result of thickness-limited crystalline domain size.¹¹⁶ However, a direct correlation was observed between the seed layer (002) texture and the resulting NW orientation in the samples with greater than 30 cycles.

The (002) diffraction peak was used to measure the NW out-of-plane orientation, as its normal vector points along the NW growth direction. We observe that the χ angles with the maximum diffracted intensity in the NW samples (Figure 3.3a,b) correspond directly to the preferred angles measured from the SEM images in Figure 3.2, including the angles associated with the bimodal distribution. This allows

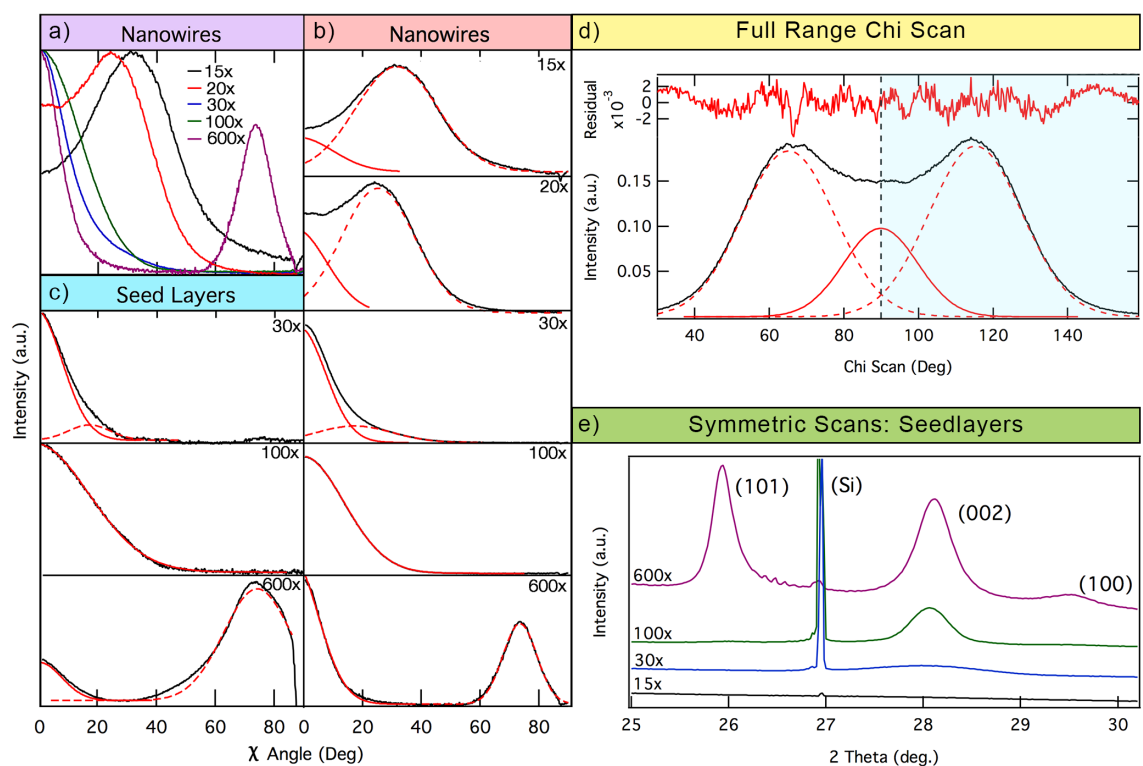


Figure 3.3: XRD χ -scan (tilt) data of the ZnO (002) peak for NWs and seed layers including (a) an overlay of the NW scans showing the orientation trends and (b, c) peak fitting for individual scans, where the solid red line is the perpendicular peak fit and the dashed line is the fit for the acute-angle peak, if any. (d) Full 180° χ -scan show symmetry about the perpendicular direction. (e) Symmetric θ - 2θ scans for the seed layers.

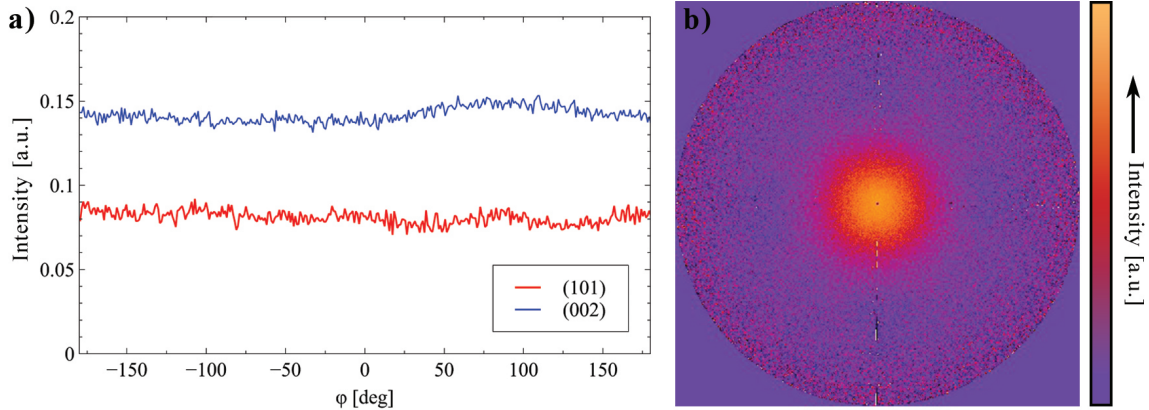


Figure 3.4: a) The phi scan of NWs grown on a 15 cycle seed layer also communicates this same lack of in plane texture by showing that the intensity of the (101) and (002) peaks does not change for the full 360 rotation of the sample. This phi scan was performed at a chi angle of 30 which corresponds to the maximum (002) peak intensity across all chi angles. b) Full pole figure showing (002) intensity for the 100 cycle seed layer. The radial decrease in intensity from the center conveys the preferred orientation communicated by the chi scans and the lack of rotational variation indicates that there is no in-plane texture.

for a quantitative comparison to the SEM data, providing insight into the mechanism of orientation control afforded by the ALD seeding process.

Gaussian peak fitting for the NW samples (Figure 3.3b, red lines) shows that the 15-cycle sample has a dominant preferred orientation of 30° relative to the substrate normal with a lesser preferred orientation of 0° . The 20-cycle sample shows growth of the 0° preferred orientation and a shift to smaller angle for the preferred acute angle. With an increase to 30 cycles, the dominance of these peaks is reversed. The vast majority of the NWs now have a preferred orientation near 0° , while only a small portion grows with an acute preferred angle. The NWs grown on the 100-cycle seed layer no longer show a preferred acute angle and are all encompassed in the distribution centered about 0° . The 600-cycle sample maintains a 0° preferred orientation, but also includes a second preferred orientation showed by the high angle peak at 73° . Peak fitting for the seed layer samples shown in Figure 3.3c results in

the same peak profiles as identified in the corresponding NW samples in Figure 3.3b. This demonstrates a direct correlation between the texture of the seed layer and the resulting NW orientation and illustrates the power of ALD to vary NW orientation through precise texture control in the seed layers.

To understand the emergence of the bimodal distribution in the samples with greater than 100 cycles, we consider a synergistic combination of effects involving crystallographic texture and film roughness. As the ZnO film thickness increases in ALD deposition, the surface roughness and average grain size both increase.¹¹⁷ ZnO NWs are known to nucleate on exposed (002) planes. Symmetric $\theta/2\theta$ XRD scans of the seed layers in Figure 3.3e show that the 100-cycle sample has a strong preferred (002) texture relative to the substrate surface, whereas the 600-cycle sample has a mixture of (101) and (002) preferred texture. For the 100-cycle sample, the polycrystalline grains have a higher lateral frequency due to the smaller grain diameter than for thicker films. NW nucleation will occur mainly on the energetically favorable sites where vertically oriented (002) planes are exposed. If a NW nucleates at an angle that deviates too far from the surface normal, it will quickly terminate due to steric hindrance. This results in the dense, perpendicularly oriented NW arrays observed in the 100-cycle sample.

In contrast, the texture of the 600-cycle sample indicates that a combination of (101) and (002) planes is aligned vertical to the substrate. From the SEM analysis, we observe that the density of perpendicular NWs is significantly reduced compared to the 100-cycle sample. The (101) texture and increased film roughness indicate that (002) planes may also be exposed at lower angles in the thicker samples. This is strongly supported by the fact that NWs that nucleate and grow on (002) planes in grains with (101) texture would be oriented at approximately 62° from the surface normal, which closely matches the acute angle observed in the bimodal distribution in the SEM images. Therefore, we conclude that a combination of evolving crystallo-

graphic texture and increasing film roughness with increasing cycle number leads to the formation of the bimodal distribution in the thicker seed layer growth.

3.1.2 Reduced Nanowire Nucleation on Ultra-Thin ALD ZnO Films

An understanding of the low-cycle regime requires a deeper investigation of the fundamental nucleation and growth behavior of the ALD films during the initial cycles. To investigate the seed layer structure and morphology in these ultrathin seed layers, TEM analysis was performed on 15-, 30-, and 100-cycle ALD ZnO films deposited on 18 nm amorphous SiO₂ TEM grids. A set of plane-view BFTEM and HRTEM images in Figure 3.5 a,b displays polycrystalline grains in all three samples. Contrast differences between each grain in the BFTEM images in Figure 3.5a stem from different out-of-plane orientations. The polycrystallinity of the samples is supported by corresponding fast Fourier transform (FFT) insets from the HRTEM images in Figure 3.5b, revealing ring-shaped spot patterns. The 15-cycle ALD ZnO sample consists of small grain sizes (lateral diameter <5 nm) with crystalline domains, as confirmed in BF and HRTEM (Figure 3.5b-1, c-1). However, we cannot conclusively determine from the TEM data if these grains are distinct islands or connected by an amorphous wetting layer. For very thin seed layers (20 ALD cycles) the resulting NWs grow individually or in small groups with a separation of 1–2 nm, as seen in Figure 3.2. This indicates that the sparse density of NWs in these ultrathin seed layers is determined by additional limiting factors beyond the aerial density of the seed grains, which are much more closely spaced. As the number of ALD cycles increases to 30, the TEM analysis exhibits nearly 100% coverage of larger ZnO grains (d = 5–10 nm), which is consistent with the transition to nearly continuous NW coverage shown in the SEM analysis.

Island formation, which can occur due to nucleation, surface diffusion, and crystallization behavior during the initial ALD cycles,^{55,64,88} is consistent with the lower

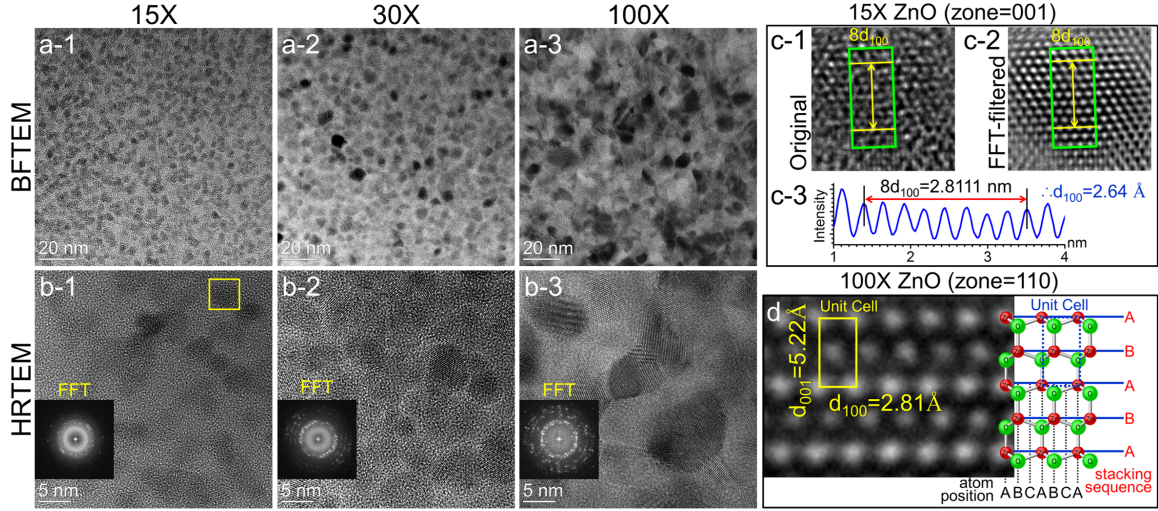


Figure 3.5: Plane-view BFTEM (a) and HRTEM (b) images of 15-cycle (1), 30-cycle (2), and 100-cycle (3) ZnO films deposited on SiO₂ TEM grids, with FFT insets. (c) A magnified grain from the yellow box in the 15x sample, displaying the [001] wurtzite zone. A line profile over eight [100] planes measures $d_{100} = 2.64\text{\AA}$. (d) 100x ALD ZnO grain aligned along the [100] zone axis, with a measured projected unit cell dimension of ($d_{100} = 2.81\text{\AA}$, $d_{001} = 5.22\text{\AA}$).

density of crystalline domains observed in the 15-cycle ALD film. Interestingly, we observe a shift in the crystallographic and chemical nature of these isolated grains compared to the continuous films at greater thicknesses. Analysis of [100] planes in the HRTEM image of the 15-cycle ZnO at the wurtzite [001] zone axis (Figure 3.5c) indicates an interplanar spacing of $d_{100,15x} = 2.64\text{\AA}$, which is contracted from the $d_{100,bulk} = 2.815$ value of bulk wurtzite ZnO. On the other hand, the 100-cycle ZnO sample (Figure 3.5d) displays a [110] zone-projected unit cell dimension ($d_{100} = 2.81\text{\AA}$, $d_{001} = 5.22\text{\AA}$), in agreement with the expected bulk values.

This lattice contraction behavior is confirmed by selected area diffraction (SAD), Figure 3.6 for the lattice parameters of the 15-cycle sample ($a = 3.04\text{\AA}$, $c = 4.88\text{\AA}$), 30-cycle sample ($a = 3.08\text{\AA}$, $c = 4.95\text{\AA}$), and 100-cycle sample ($a = 3.25\text{\AA}$, $c = 5.22\text{\AA}$). While the phase of the 100-cycle ZnO seed film is consistent with bulk ZnO, the 15- and 30-cycle ZnO films have lattice parameters that are contracted by 6.9%

and 5.4%, respectively, from the standard bulk parameters. This size-dependent lattice contraction below 5–10 nm dimension has been reported previously in a variety of material systems^{118–121} due to surface stress effects in the Laplace-Young equation. This results in a strain that is inversely proportional to the particle diameter, inferring surface-induced lattice contraction of the seed layers in the thinnest ALD films.^{118,119,122}

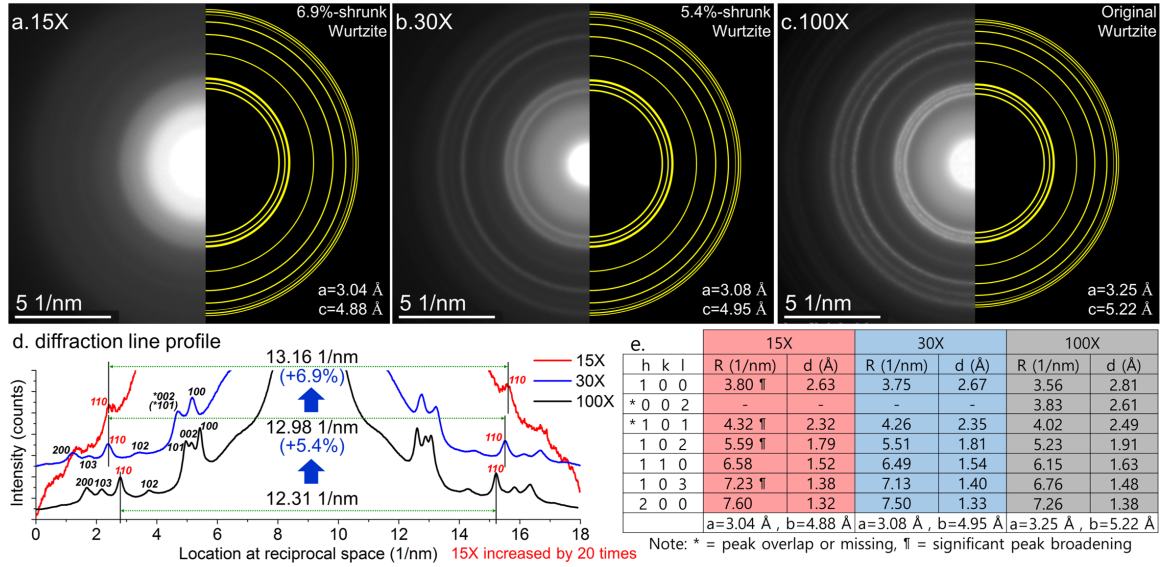


Figure 3.6: Three sets of SAD patterns at left and simulated powder diffraction (ring type for TEM) at right of ALD 15x (a), 30x (b) and 100x (c) ZnO to obtain lattice parameter by direct comparison. (d) Line profile of diffraction intensity at center of 15x (red), 30x (blue) and 100x (black): direct comparison of R₁₁₀ (110 reflection) on reciprocal space indicates isotropic shrinking of lattice parameter (a, c) by 6.9 and 5.4 % for ALD 15x and 30x respectively against original Wurtzite at 100x using $R_{hkl} \times d_{hkl} = \text{constant}$ relationship. (e) Summary of measured R values (reciprocal distance from center to diffraction) and corresponding interplanar spacings of the consecutive 7 peaks. Please note that because each diffraction ring changes proportionally without distortion, the c/a ratio of Wurtzite ZnO is reserved. At low ALD cycle numbers, lattice parameters of Wurtzite structure appear contracted. Even though ring patterns at 15x are significantly broadened by small crystallite size, we can detect crystallinity. However, (002) peak seems to disappear (be weakened) or overlap with the (101) peak. Measured lattice parameters ($a=3.25\text{\AA}$, $c=5.22\text{\AA}$) are well matched with previous literature.

As the TEM and SEM analyses demonstrate, the lower density of NWs grown from the thinner seed layers is due to additional factors besides sparse availability of nucleation sites, as the inter-NW spacing is much larger than the inter-seed grain spacing. We observe that the variations in the crystallographic and chemical properties of the thinner seed layers impact the NW density. Due to coincident site lattice (CSL) mismatch in the strained seed layers, the nucleation probability during hydrothermal synthesis will be reduced compared to a stress-free surface, such as the 100-cycle seed layer, which has the bulk ZnO lattice parameters. As the thickness of the ALD layer increases, the lattice contraction decreases, and the density of grains increases, leading to an increased nucleation density with film thickness. Furthermore, initially adsorbed zinc atoms on the surface during NW growth would have more degrees of freedom to move along the surface between continuous grains than discontinuous or semicontinuous grains with crystallographically undeveloped wetting layers, increasing the probability of reaching the critical nucleation radius for growth. Thus, the combination of thickness-dependent lattice contraction due to surface stress and coverage of seed layer grains could synergistically limit the density of NW grown on seed layers thinner than 30 cycles.

In addition to these geometric effects, variations present in the isolated ZnO crystallites are affected by differences in their surface chemistry vs the bulk films. To investigate these effects, we performed XPS analysis of the seed layers at varying thicknesses to provide information on the chemical bonding environment where NW nucleation would occur.

Investigation of the O 1s core-level data (Figure 3.7) was performed by fitting the data with four peaks: Zn-O (~ 530.0 eV), Zn-OH (~ 531.1 eV), C-O/C=O (~ 532.0 eV), and SiO₂ (~ 32.9 eV).¹²³⁻¹²⁵ For the 15-cycle sample, a relatively large concentration of hydroxyl-terminated Zn was observed, suggesting that the bonding may be dominated by surface hydroxyls during the initial island growth. These surface

hydroxyls are an expected product of the standard ALD reaction mechanism using metal alkyl precursors and water as an oxidant.⁵⁵ As the number of cycles increased, an initial increase followed by a continual reduction in relative fraction of Zn-hydroxyl bonds was observed, after reaching a maximum value in the 30-cycle sample. This is likely due to the formation of a continuous ZnO film, leading to a decrease in the fraction of Zn atoms on the surface compared to isolated islands. The continual increase of the relative peak height at ~ 530 eV (Zn–O) is indicative of increasing bulk ZnO on the surface. This further suggests that a chemical shift in the properties of the sub-30-cycle seed layers plays an important role in the nucleation behavior and formation of acute preferential angles of NWs on these ultrathin seed layers.

3.1.3 ALD Nanowire Seeding on a Range of Substrates

Equipped with the morphological tunability of NW arrays afforded by the ALD seeding process, we can now apply this technique to fabricate heterogeneous material assemblies with highly repeatable control and precision. To demonstrate the full power of this technique for hierarchical material synthesis, ALD seed layers were conformally deposited onto a variety of 3-D templates. NWs were then grown on their surfaces using the identical hydrothermal growth procedure. The 15- and 100-cycle trends in orientation, size, and density of ZnO NWs grown on vertical Si micropost arrays were consistent with the growth on the planar substrates, as shown in Figure 3.8a. As with the planar samples, the 15-cycle samples grown on microposts have an acute preferred angle relative to the projected normal along the 3-D post surface, while the NWs grown on the 100-cycle sample exhibit a preferred perpendicular orientation. Additionally, the NWs on the 15-cycle sample are less dense and larger, both of which are trends carried over from the planar samples. This demonstrates that the quantitative and deterministic control of ZnO NW morphology using the crystallographic textural evolution ALD seeding can be extended to nonplanar hierarchical

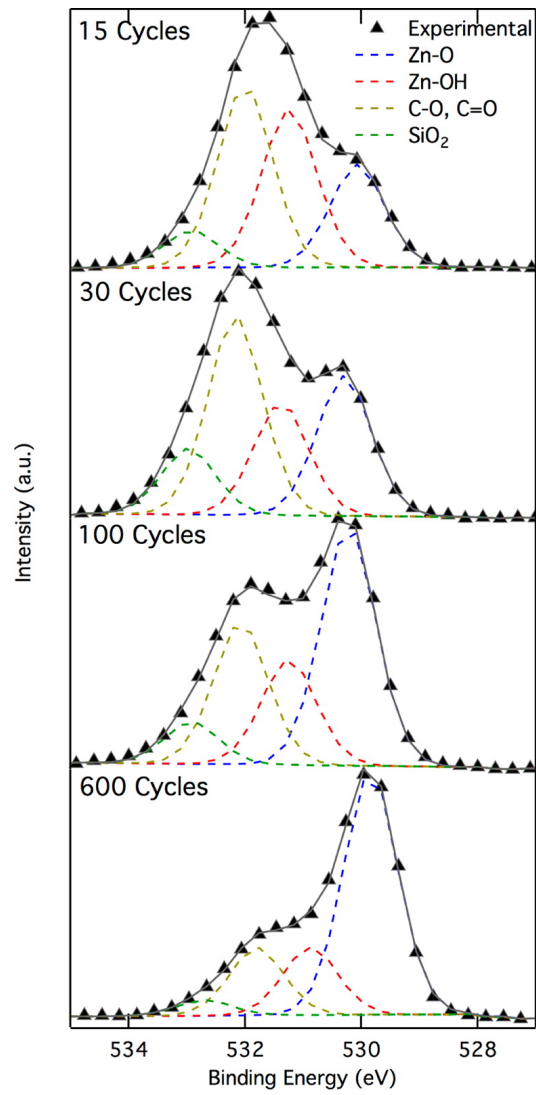


Figure 3.7: XPS scans of the ZnO O 1s spectrum in ALD films with various cycle numbers.

material synthesis. The benefits of the conformality of the ALD coating are shown by the consistent coverage along the entire micropost array and substrate surface in a lower magnification image in Figure 3.8c.

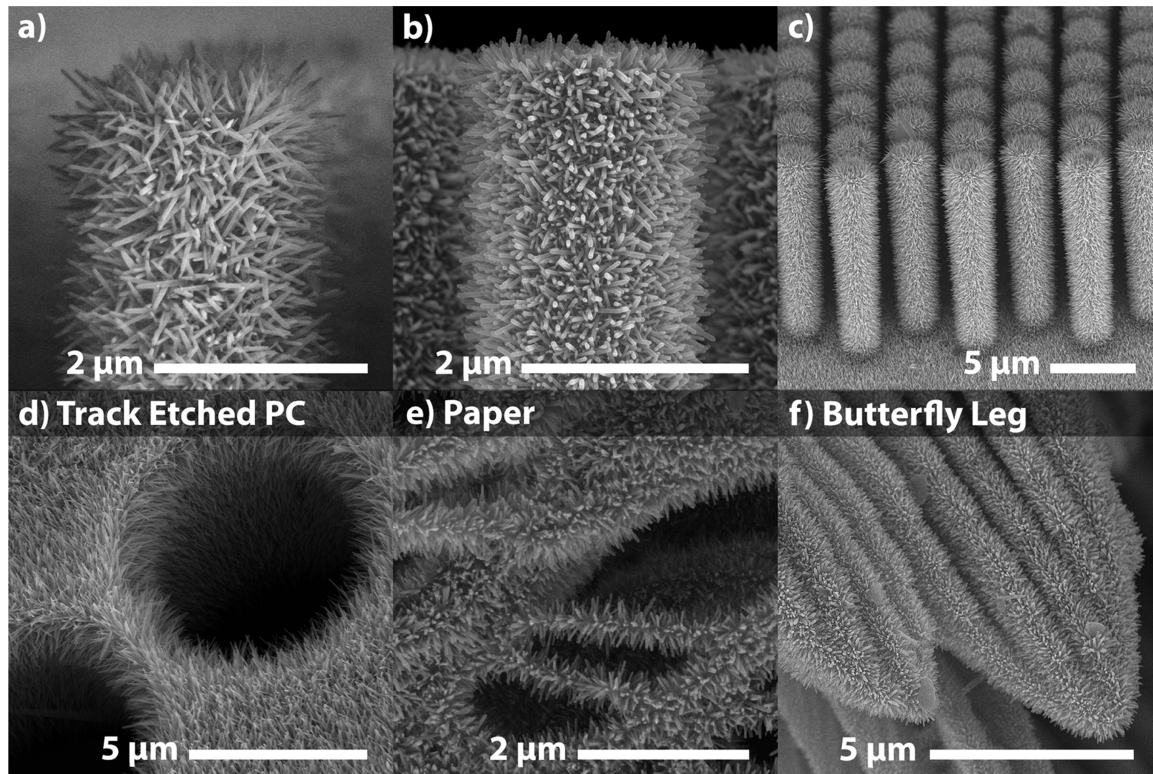


Figure 3.8: SEM analysis of (a) ZnO NWs grown on a 15-cycle seed layer on Si microposts, (b) ZnO NWs grown on a 100-cycle seed layer on Si microposts, (c) low-magnification image of ZnO NWs on Si microposts, (d) ZnO NWs grown on a track-etched polycarbonate membrane, (e) ZnO NWs grown on cotton fiber filter paper, and (f) ZnO NWs grown on a butterfly leg.

While Si is an inorganic crystalline substance, ALD also provides a consistent method of seeding other substrates with dramatically different chemical and physical properties. To demonstrate this versatility, dense coatings of NWs were grown on track-etched polycarbonate membranes, as shown in Figure 3.8d. NWs were observed to grow into the pores of the membrane, and although diffusion limitations in the solution growth are eventually expected to limit uniformity in very high aspect ratios, this demonstrates the ability to create hierarchical structures on arbitrary geometric

forms, with either convex or concave geometries. This is a step toward manufacturing complex integrated material systems with arbitrary geometric complexity while control of relative feature geometries in heterogeneous material systems is maintained. This also demonstrates the ability to coat temperature-sensitive polymer materials, which are amorphous and flexible.

The versatility of this technique is further demonstrated by coating cotton fiber paper substrates, as shown in Figure 3.8e. Paper represents an increasingly important substrate for flexible, low-cost, lightweight, functional material synthesis.¹²⁶ The integration of functional inorganic materials onto paper substrates provides a pathway to manufacture novel devices, including flexible electronics, energy devices, and sensors. Our ability to coat paper fibers with inorganic nanomaterials strongly benefits from the ALD seeding process,¹²⁷ both due to the conformality of the seed layer deposition into the high-aspect-ratio paper fiber structure and the ability to control the crystallographic texture of the seeding layer independent of the substrate chemical properties.

Finally, this process was demonstrated to facilitate formation of biotic-abiotic interfaces by conformally coating the 3-D surfaces of various biological substrates with NWs. These materials tend to be highly sensitive to temperature and chemical exposure, so the low-temperature and benign chemistry of this process is well-suited to ensure compatibility. Figure 3.8f shows the leg of a butterfly that has been conformally coated with ZnO NWs. We have also coated several other biological species with NWs, including insects and leaves, using this approach. This opens up the possibility of biotemplating of natural materials and systems with inorganic nanomaterials, which is an emerging field of nanoscience that enables a wide range of applications, including energy conversion, superhydrophobicity, structural coloration, and thermal materials.¹²⁸⁻¹³¹ Importantly, the hierarchical structural complexity provided by nature does not require any lithography or clean-room processing to provide

a 3-D template, and the functional properties of these natural materials can be further tuned using this new technique to add an additional layer of hierarchical complexity to their structure. Some consideration of surface chemistry and compatibility of the material with process conditions is needed, but a wide variety of plants and animals, chosen for a specific surface structure, could be used as a template upon which to grow additional hierarchical complexity with controllable size and orientation using ALD seeding.

3.2 Conclusion

This study represents a platform to expand our ability to manufacture integrated systems at the nanoscale, with programmable and scalable synthesis of complex geometries and relative component orientations. Furthermore, by extending a simple and powerful technique such as hydrothermal ZnO NW synthesis to a wide range of flexible, 3-D, high-aspect-ratio, and low-cost substrates, we open up the possibility of engineering these nanoscale systems in useful products that can be scalably manufactured with improved control.

CHAPTER IV

Rational Design of Hyperbranched Nanowire Systems for Tunable Superomniphobic Surfaces

Adapted with permission from Bielinski, A. R.; Boban, M.; He, Y.; Kazyak, E.; Lee, D. H.; Wang, C.; Tuteja, A.; Dasgupta, N. P. Rational Design of Hyperbranched Nanowire Systems for Tunable Superomniphobic Surfaces Enabled by Atomic Layer Deposition. ACS Nano 2017, 11 (1), 478-489. Copyright 2017 American Chemical Society.

4.1 Branched Nanowire Arrays

Current synthesis techniques provide careful control of NW morphology and consequently their mechanical, electronic, and optical properties.^{43,132} However, while NW arrays and single NW devices have been widely investigated,^{7,133} hierarchical assembly of these nanoscale building blocks into ordered three-dimensional systems remains challenging.^{13,21,134-136} Here, we demonstrate that the ability to rationally design hierarchical assemblies allows for the systematic design of superomniphobic surfaces with excellent control over the obtained contact angles and contact angle hysteresis, with a broad range of liquids.

To demonstrate this concept, we first describe a method for the bottom-up fabrication of hierarchical hyperbranched NW structures, with deterministic control over the geometric parameters for each level of hierarchy. Figure 4.1 diagrams three levels of branched hierarchy, along with the design parameters that are manipulated at each level. We will use the notation in Figure 4.1 (inter-branch spacing D_x , branch radius R_x , and branch angle relative to substrate θ_x , where x is an index of the level of hierarchy) for consistency when describing geometric control parameters. In this work, this programmable control of these geometric parameters is used to tune superomniphobic surfaces, allowing fine adjustment of contact angles and resistance to wetting by a variety of both high and low surface tension liquids.⁹³ The geometric control of individual levels of hierarchical texture on a surface can be correlated with quantitative models that can predict the experimentally measured contact angles, as well as resistance to wetting by various liquids under pressure, making it a well-suited platform to demonstrate this application of materials by design.

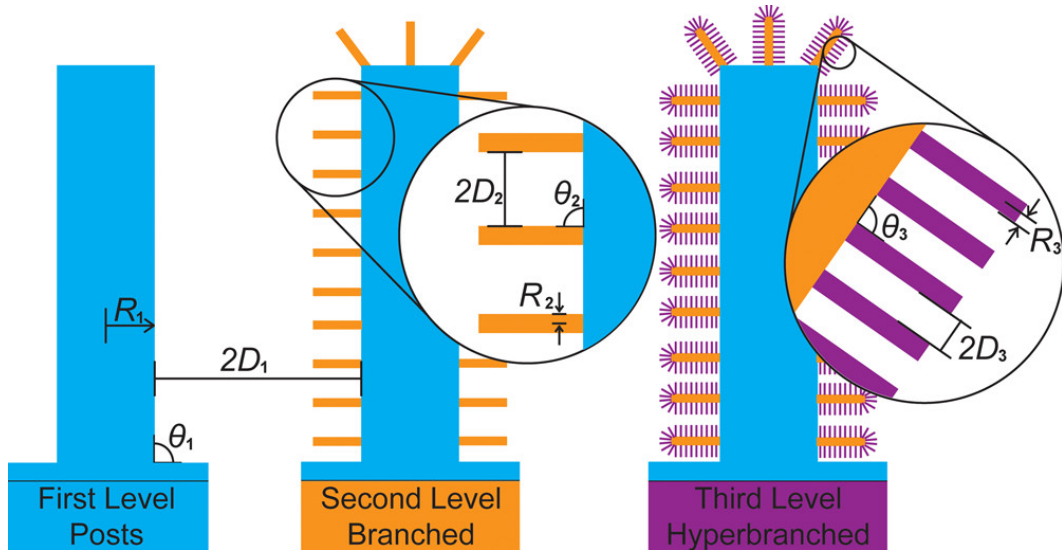


Figure 4.1: Diagram (not to scale) showing three successive levels of hierarchy along with the size, density, and orientation design parameters that can be controlled at each level.

Most current approaches to the assembly of hierarchical NW structures onto a substrate begin with either a patterning step, such as lithography or self-assembly, or rely on stochastic processes such as random attachment or supersaturated phase transformations.^{26,29,71,136–139} Patterning steps are limited by resolution, scalability, substrate compatibility, and cost. In particular, challenges arise when nonplanar substrates are used, as photolithography is line-of-sight limited. Random attachment or supersaturation methods are simple and low-cost, but they lack the control over the feature size, orientation, and spacing needed to enable materials by design. While complex hierarchically branched nanostructures can be formed using a variety of colloidal synthesis approaches,^{140,141} the formation of ordered assemblies spanning multiple length scales and over large-area substrates remains challenging using purely solution chemistry. In particular, the ability to produce tunable 3D features on the surface of high aspect ratio substrates requires extremely conformal deposition processes, as each sequential level of hierarchy must be assembled on the previous nonplanar surface.

For bottom-up NW growth, directed heterogeneous nucleation on nonplanar substrates requires control over the substrate surface chemistry and crystallographic texture. The rational growth of branched and hyperbranched NWs has been previously demonstrated using sequential seeding processes that rely on either solution- or vapor-phase deposition (typically sputtering or evaporation) of catalyst seeds onto NW surfaces.^{13,21,135,142,143} However, these approaches are limited in their ability to simultaneously control seed size, density, and crystallographic orientation, especially over high aspect ratio surfaces with both concave and convex features. This becomes increasingly challenging with multiple levels of hierarchy. Additionally, the use of high-temperature and/or high-vacuum processes limits the scalability and substrate compatibility of these approaches. To overcome this limitation, we demonstrate the use of atomic layer deposition (ALD) to independently control the interfacial composition, morphology, and microstructure of seed layers between three different levels of

hierarchy, which directs subsequent heterogeneous nucleation and growth of hyper-branched structures.

4.1.1 ALD Overlayers for Control of Nanowire Density

Here, we extend this concept to facilitate sequential growth of branched NWs with independent control of size, orientation, and spacing in both the branches and trunks (following a tree analogy). This requires an initial array of NW trunks with sufficiently large inter-NW spacing, as shown by design variable D_2 in Figure 4.1, as well as perpendicular orientation to the substrate, that is, $\theta_2 = 90^\circ$, to provide room for subsequent branches. Previously, we demonstrated that arrays with large inter-NW spacing can be seeded using ultrathin ALD films in the range of 2–4 nm.⁴ In this case, surface stress effects arising from island growth in the ALD seed layer reduce the NW nucleation probability during hydrothermal growth, resulting in a low-density array. However, the higher inter-NW spacing (large D_2) is coupled with a preferential, nonperpendicular axial orientation ($\theta_2 < 90^\circ$) using this approach. NW arrays grown perpendicular to the substrate are easily achievable using slightly thicker seed layers but also result in smaller inter-NW spacing.⁴

To enable branched NW synthesis, we developed an ALD seeding technique to decouple the NW orientation and density. As shown in Figure 4.2a, ALD was used to first deposit a ZnO seed layer with preferential (002) texture to enable perpendicular NWs. Then a second incomplete monolayer was deposited on top of the ZnO seed layer consisting of 3 – 5 cycles of amorphous ALD TiO₂. Amorphous TiO₂ films by ALD do not act as seed layers for ZnO NW growth. Thus, the incomplete TiO₂ layer partially blocks nucleation sites on the ZnO seed layer, while still leaving some exposed crystalline regions to the growth solution. Due to the self-limiting nature of ALD, the surface fraction of the seed layer that is masked from the solution can be precisely and reproducibly controlled with sub-monolayer precision by varying the

number of ALD TiO_2 overlayer cycles, illustrating the power of this approach for programmable control of geometric design parameters D and θ via NW seeding.

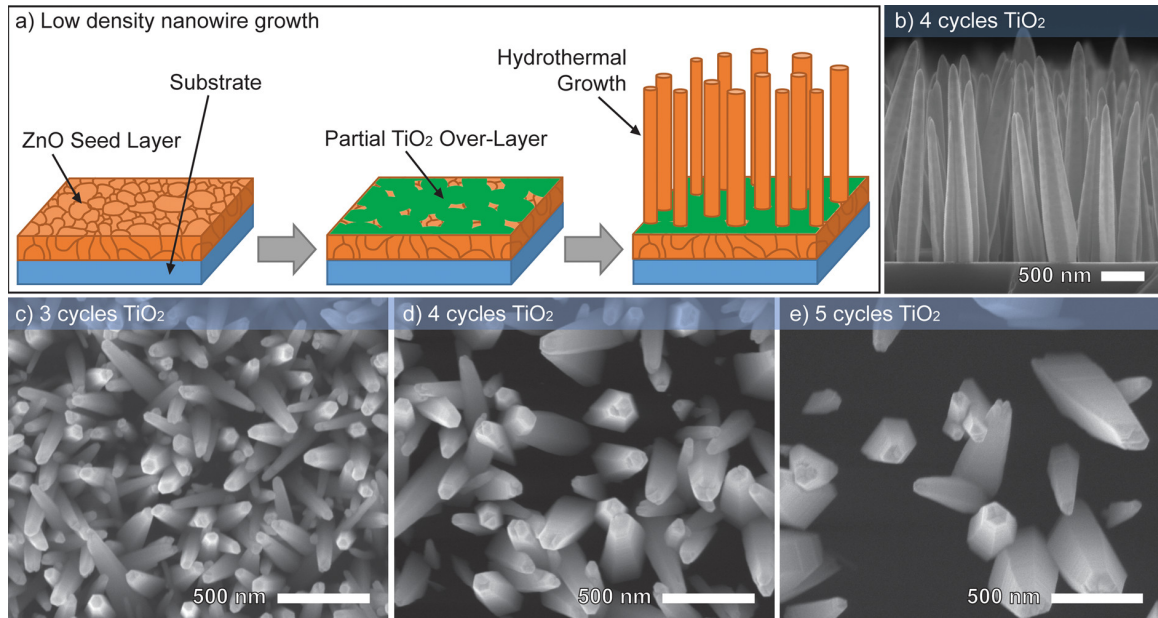


Figure 4.2: (a) Diagram of low-density NW growth procedure showing the ZnO seed layer, sub-monolayer TiO_2 overlayer, and hydrothermal NW growth. (b) A 90° cross-section scanning electron microscopy (SEM) image of low-density NWs grown with 4 cycles of TiO_2 over a 100 cycle ZnO seed layer showing NW orientation perpendicular to the substrate. (c-e) Top-down SEM images of NWs grown with 3, 4, and 5 cycles of TiO_2 over a 100 cycle ZnO seed layer showing decreased array density, increased D_2 values, with increased number of TiO_2 cycles.

Figure 4.2c-e shows the progressive decrease in NW density as the number of TiO_2 overlayer cycles is increased from 3 to 5. This can be accomplished irrespective of substrate material and geometry by simply encoding the recipe for NW growth in the ALD seed layer. The power of ALD to precisely deposit sub-monolayer films is essential for this approach and would be extremely difficult to replicate with other techniques. This enables independent control of inter-NW spacing, D_2 , as determined by the TiO_2 partial interlayer, while maintaining perpendicular orientation, $\theta_2 = 90^\circ$, which is determined by the ZnO seed layer, shown in Figure 4.2b.

When using thinner TiO_2 overlayers (1-2 cycles), the NW density remains nearly identical to that on the initial seed layer, suggesting insufficient blocking of active sites for heterogeneous nucleation. For thicker overlayers of ≥ 6 cycles, the NW density continues to decrease until a continuous TiO_2 overlayer forms, at which point the density is effectively zero. Incomplete Al_2O_3 films deposited by ALD were also tested as blocking overlayers but were found to be unsuitable, as a Zn-Al layered double hydroxide structure formed at the interface due to the reaction between the Al atoms and the hydrothermal growth solution, interfering with the nucleation process.¹⁴⁴ As a result, the use of Al_2O_3 seed layers results in the growth of nanosheets instead of NWs, Figure 4.3 which is another powerful knob that could be tuned to enable hierarchical materials by design.

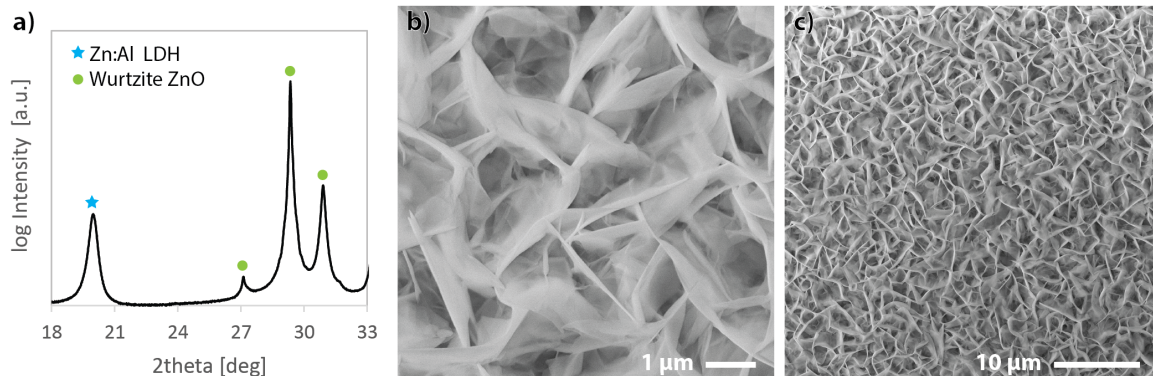


Figure 4.3: a) Symmetric $\theta/2\theta$ synchrotron x-ray diffraction pattern showing wurtzite ZnO peaks from the nanosheets and a LDH peak from the substrate. b,c) SEM images showing the nanosheet morphology.

4.1.2 ALD Interlayers for Branched Nanowires

Once perpendicularly oriented NWs of desired density were formed, the next challenge in the sequential synthesis of branched ZnO NWs was to seed the branches on their surfaces. Initial attempts to accomplish this using ALD of ZnO to form a core-shell structure failed to produce branched NWs during subsequent hydrothermal growth. ALD ZnO usually deposits as a nanocrystalline film independent of the

substrate, which acts as a seed layer for hierarchical structures. However, epitaxial growth of the ALD shell on the initial single-crystalline ZnO NW core was observed to occur, despite the low temperature (150°C) used. This result is of significant interest to the ALD research community, as low-temperature epitaxial ALD growth has been rarely achieved. With an epitaxial seed layer, subsequent growth steps simply led to enlargement of the length and diameter of the initial set of NWs rather than growth of perpendicular NW branches.

The epitaxial growth behavior was confirmed using high-resolution transmission electron microscopy (HRTEM), shown in Figure 4.4b. NW arrays were grown on planar Si substrates, coated with the desired ALD films and then transferred to TEM grids for study. Three samples were observed. The first was a control sample of as-grown ZnO NWs. The second had a shell of 50 cycles of ZnO deposited on the ZnO NWs, and the third had an inner shell of 100 cycles of TiO₂ followed by an outer shell of 50 cycles of ZnO. Figure 4.4a-c shows HRTEM images of these samples inset with the corresponding selected area electron diffraction pattern. Figure 4.4a shows that the initial NWs are single-crystalline wurtzite. Figure 4.4b shows that an ALD ZnO film deposited on the NWs grows epitaxially on the NW surface.

In order to block epitaxial growth, we devised a method to deposit an interlayer between the initial low-density NW array and the second ZnO seed layer for the branches, as shown in Figure 4.5a. For this, we used thin (50–100 cycle) ALD TiO₂ interlayers. Unlike the incomplete TiO₂ films used for the low-density synthesis, >50 cycles of TiO₂ creates a complete film that totally encapsulates the surface, creating a core-shell structure. Figure 4.4c shows that the addition of an amorphous TiO₂ interlayer between the core NW and ALD ZnO layer disrupts epitaxial growth, resulting in a nanocrystalline ZnO outer shell. This ability to synthesize coaxial core-shell-shell NWs with programmable thickness, composition, and crystallinity is uniquely enabled by the ALD process.⁸⁸ Figure 4.4e shows a lower-magnification

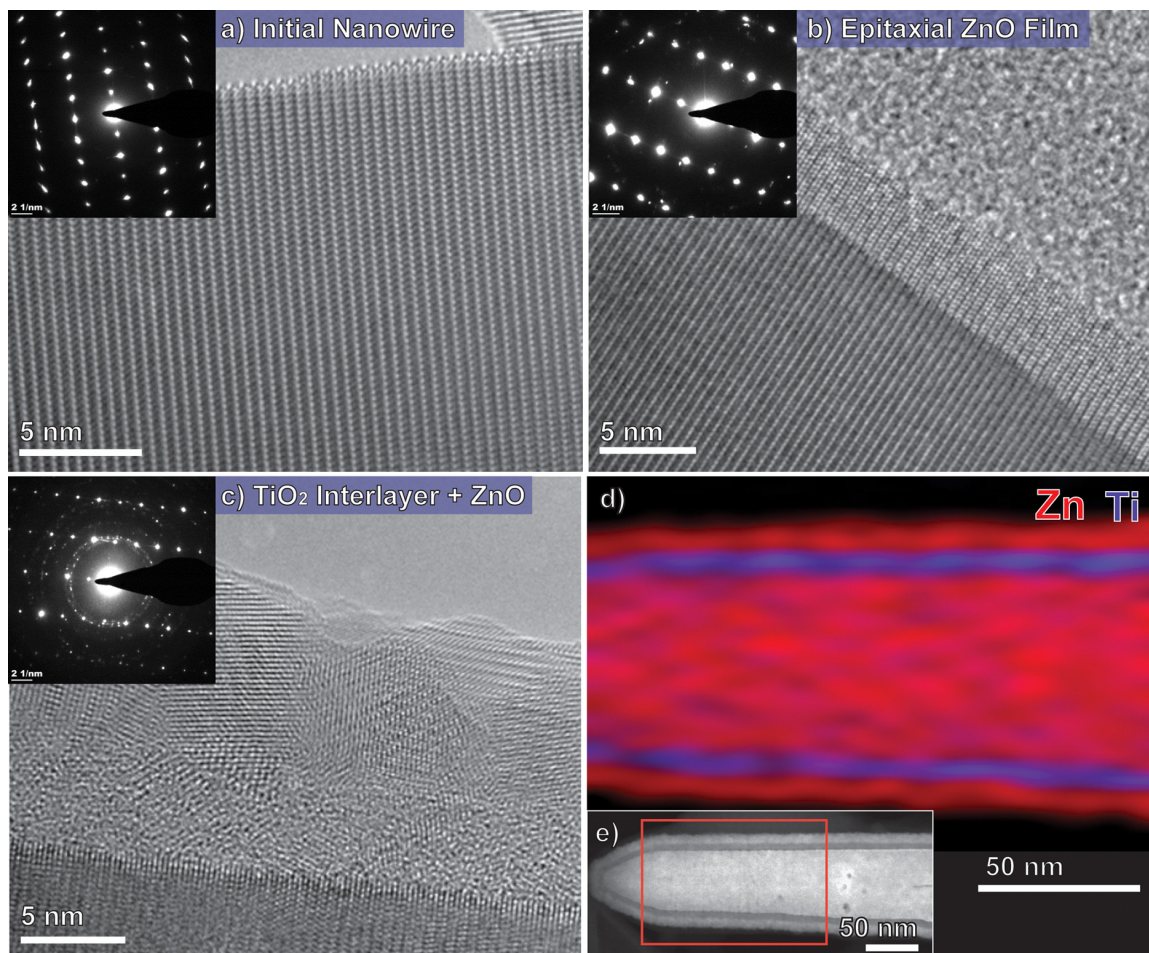


Figure 4.4: HRTEM and annular diffraction patterns (inset) of (a) single-crystalline ZnO NW, (b) ZnO NW with epitaxial ALD ZnO film growth, and (c) ZnO NW with amorphous ALD TiO₂ blocking layer and polycrystalline ALD ZnO seed layer. (d) Energy-dispersive X-ray analysis for element mapping and (e) dark-field scanning transmission electron microscopy (STEM) image of ZnO NW with ALD TiO₂ and ZnO films, where the red box shows the area analyzed in (d).

dark-field STEM image of a ZnO NW with coaxial TiO₂-ZnO shells, and Figure 4.4d shows energy-dispersive X-ray elemental mapping for the boxed region of that NW. Figure 4.4d,e shows that the ALD films coat the NW conformally and that the shell interfaces remain distinct.

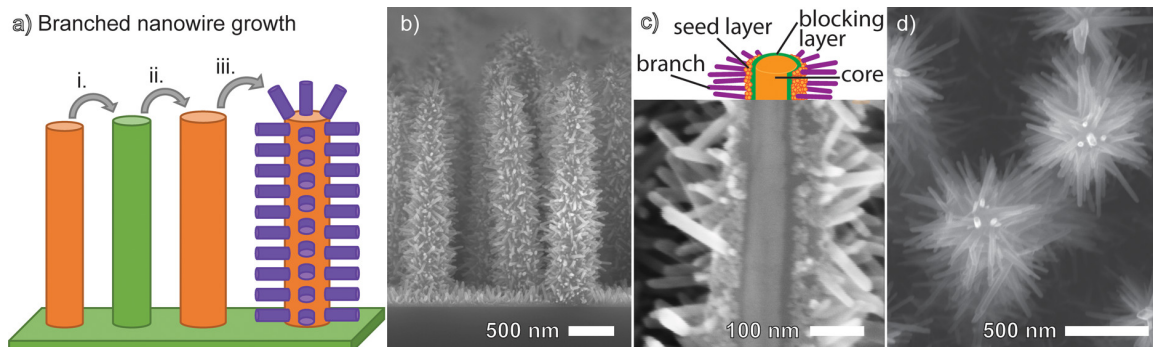


Figure 4.5: (a) Diagram of ALD interlayer procedure for branched NW seeding starting with an array of low-density ZnO NWs, then (i) adding an ALD TiO₂ blocking layer, (ii) adding an ALD ZnO seed layer, and (iii) hydrothermal NW growth. (b) Cross-section SEM of branched ZnO NWs. (c) Cross-section SEM and diagram of a split branched NW and showing the NW core, ALD TiO₂ blocking layer, ALD ZnO seed layer, and ZnO branches. (d) SEM top-down view of branched ZnO NWs.

Using this disrupted epitaxy approach, in combination with partial blocking of the initial ZnO seed layer to form perpendicularly oriented NW arrays with large inter-NW spacing, we demonstrated the ability to form branched ZnO NW arrays, where the initial trunk geometry (R_2 , D_2 , and θ_2) is programmed using the ZnO/partial TiO₂ overcoat strategy, and the branch geometry (R_3 , D_3 , and θ_3) is programmed using the TiO₂ interlayer/ZnO overcoat strategy. The size, density, and orientation of the branches can be tuned by simply varying the number of ZnO ALD cycles in the outer shell layer, following our previous report. SEM images of branched ZnO NWs with large inter-trunk spacing are shown in Figure 4.5. Figure 4.5c shows a cross-sectional SEM image of a single branched NW that fractured along its axis, in

which the core NW, amorphous TiO₂ blocking layer, nanocrystalline ZnO shell seed layer, and ZnO branches can all be clearly resolved.

As we previously demonstrated for ALD seeded ZnO NW growth, branched ZnO NWs can be grown on a variety of surfaces including structured Si, glass, polyamide film, and cotton fibers.⁴ SEM images of branched nanowires on these substrates are shown in Figure 4.6. This illustrates that the use of ALD for interfacial control in multilevel hierarchical structures has versatile application potential. Figure 4.7 shows SEM images of branched NWs grown perpendicular to the surface of Si microposts. The SEM images demonstrate that the synthesis method described above for branched NWs with controlled density is suitable for growth on textured substrates with high aspect ratios and is not line-of-sight dependent. These posts were synthesized using standard photolithography and anisotropic dry etching for simplicity; however, the substrate versatility of this approach allows for conformal coating of virtually any micro- or nanostructured surface. Figure 4.7b,c shows that the control of NW size, orientation, and inter-NW density can be independently controlled and maintained along the entire surface of these textured structures. For example, by increasing the number of ALD TiO₂ overlayer cycles before the ZnO NW trunk layer growth, Figure 4.7c demonstrates that a larger inter-NW spacing of the trunks can be conformally achieved along the micropost surface. SEM images of single layers of NWs on Si microposts are included in Figure 4.8. The resulting hyperbranched structures thus allow for individual control of each level of hierarchy in this three-level structure, as proposed in Figure 4.1, enabling the design and optimization of surface texture for structural omniphobicity, which is described in Chapter IV.

4.2 Super Omniphobicity

Superomniphobic surfaces display contact angles of $\theta^* > 150^\circ$ and low contact angle hysteresis with virtually all high and low surface tension liquids, including wa-

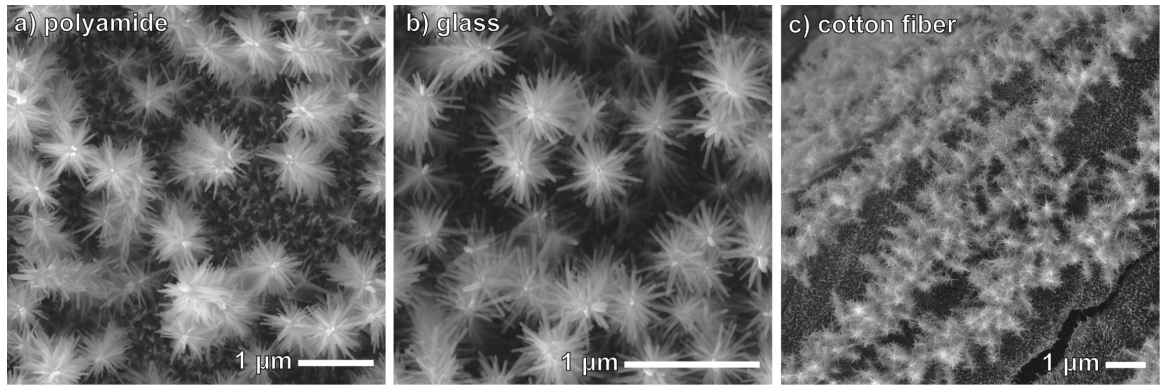


Figure 4.6: SEM micrographs of branched nanowires grown with 5 cycle ALD TiO_2 overlayers on a) polyamide film, b) glass slide, and c) cotton fiber filter paper.

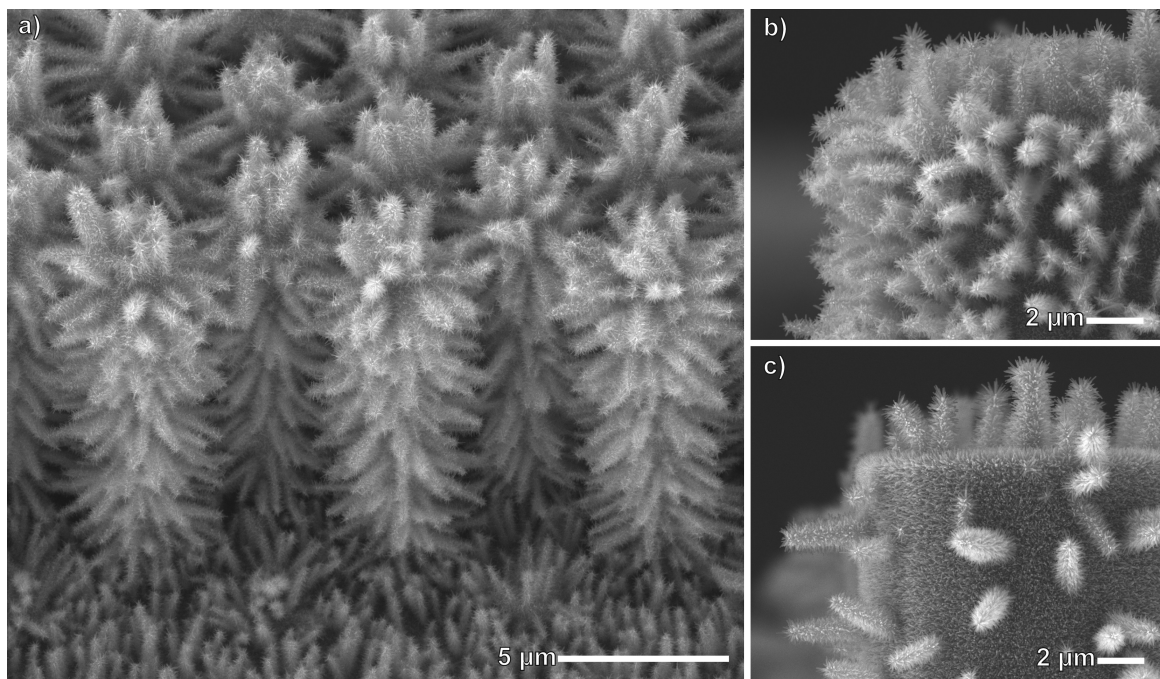


Figure 4.7: SEM images of hyperbranched structures with three levels of hierarchy (a) 45° view of branched ZnO NWs on Si microposts (seeded by a 4 cycle TiO_2 overlayer), (b) branched NWs grown with higher density trunks (seeded by a 4 cycle TiO_2 overlayer), and (c) branched NWs grown with lower density trunks (seeded by a 5 cycle TiO_2 overlayer).

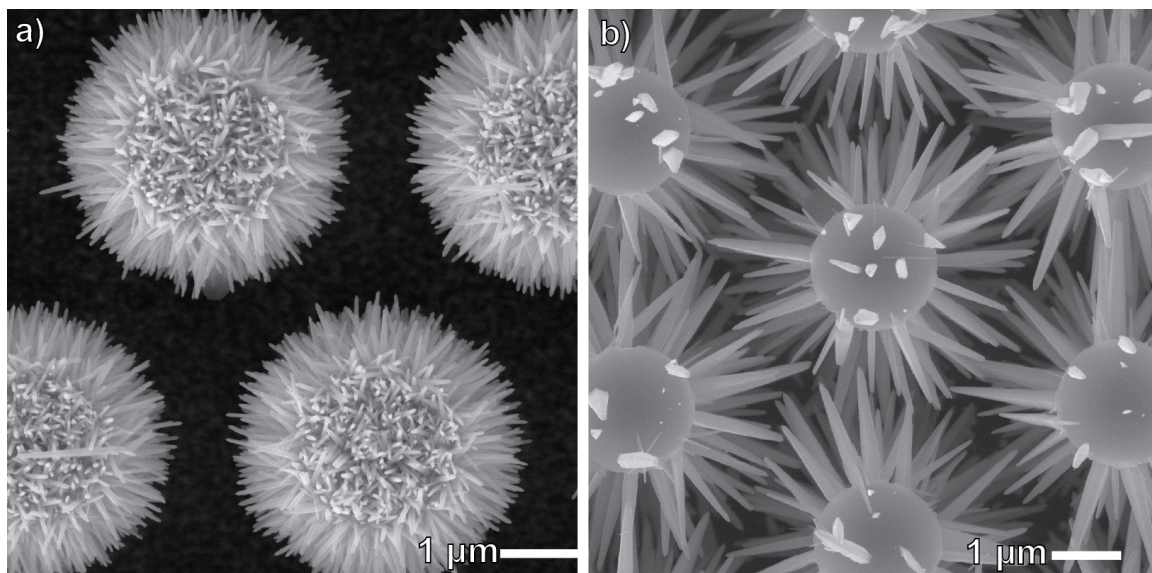


Figure 4.8: a,b) SEM showing nanowires of different densities grown on Si micropost arrays.

ter, different oils, solvents, acids, bases, and alcohols. Over the past decade, such surfaces have attracted immense commercial and academic interest due to their potential to impact a large number of applications such as self-cleaning surfaces,¹⁴⁵ nonfouling surfaces,¹⁴⁶ stain-free clothing and chemical-resistant protective wear,¹⁴⁷ drag reduction,¹⁴⁸ corrosion prevention,¹⁴⁹ and separation of liquids.¹⁵⁰ Previous work has discussed the significance of surface energy, roughness, and the critical role of re-entrant texture in obtaining surfaces that can repel low surface tension liquids such as oils, solvents, and alcohols.^{101,102,151,152} Previous work has also discussed how hierarchical scales of texture (i.e., texture on two or more length scales) can yield high contact angles and decrease the contact angle hysteresis of superomniphobic surfaces by reducing the solid-liquid contact area.^{100,153,154} However, thus far, it has not been possible to fabricate superomniphobic surfaces with three or more hierarchical scales of texture where the size, spacing, and angular orientation of features within each scale of texture can be independently varied and rationally controlled.^{155,156}

There is also significant interest in the field of materials by design, which requires new methods to rationally control the geometric parameters of complex three-dimensional assemblies across multiple length scales.^{1,157–159} This is inspired by nature, which manipulates hierarchical ordering to produce properties including superhydrophobicity, structural coloration, and high strength in composites.^{160–162} However, while there has been significant progress in fabricating bio-inspired materials, the ability to rationally synthesize hierarchical structures in three dimensions, spanning length scales from atoms to centimeters, remains challenging using traditional patterning and assembly processes. In particular, the sequential assembly of heterogeneous components into integrated systems with independent control of the size, orientation, and feature spacing for each level of hierarchy requires new approaches.

We demonstrate here the power of ALD to rationally control the hydrothermal synthesis of hyperbranched nanostructures on nonplanar surfaces. The atomic scale control of thickness, composition, and crystal structure provided by ALD enables independently programmable control of feature size, density, and orientation within each level of the hierarchical structure, as shown in Figure 4.1. This level of control allows fine optimization of super omniphobicity directed by theoretical parameters. Furthermore, this low-temperature approach can be scaled to a wide range of substrates, including flexible plastics and paper.⁴ In the future, this versatile approach can be used to design 3D hierarchical material systems for a wide range of applications, representing a pathway toward programmable nanomanufacturing.

Next, we demonstrate the power of this approach for systematically tuning the wetting properties of superomniphobic surfaces. Control over both solid surface energy and texture is required to develop surfaces capable of repelling low surface tension liquids.^{94–97,163,164} The nanowire growth method demonstrated in this work is ideally suited to fabricate surfaces with multilevel hierarchical scales of texture, as discussed earlier.

Previous reports have shown that re-entrant or overhanging texture is also critical for enabling the Cassie-Baxter state with low surface tension liquids, such as different oils and organic solvents, for which the Youngs contact angle is $\theta \ll 90^\circ$.^{101,102,149} Again, hyperbranched NWs are well-suited to producing the re-entrant texture necessary for superomniphobic surfaces.

Ideally, achieving a composite interface with a low ϕ_s (projected area of the wetted solid divided by the total projected area, Eq. 2.4) also minimizes contact angle hysteresis, $\Delta\theta$, or the difference observed between the maximum or advancing contact angle (θ_{adv}^*) and the minimum or receding contact angle (θ_{rec}^*) measurable on different surfaces. This is because any contacting liquid has effectively no interaction with the entrapped air. Surfaces with minimal $\Delta\theta$ allow liquid droplets to easily roll or even bounce off.^{93,96,100} Our capability of adding multiple levels of branched nanowires, as illustrated in Figure 4.1, has the potential to significantly reduce ϕ_s , increase (θ^*), and decrease $\Delta\theta$ simultaneously, without increasing the largest length scale of porosity, which would compromise the robustness of the composite interface. By controlling the individual geometric parameters of each level of hierarchical texture in this study, we demonstrate that model-based design of materials with tunable contact angles, contact angle hysteresis, and Cassie-Baxter state robustness is feasible. Overall, this technique can prove to be a powerful platform for the investigation of structural omniphobicity.

4.2.1 Hierarchical ZnO Nanostructures for Tunable Contact Angles

To demonstrate the application of these structures as a platform for systematically designing superomniphobic surfaces, we performed a series of experiments to establish the relationship between hierarchical scales of texture and liquid repellency. In all cases, the outer surface of structures was modified by surface functionalization with a perfluorinated monolayer (see Appendix A). This allowed for a consistent surface

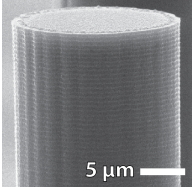
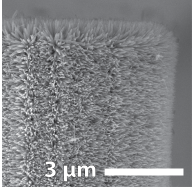
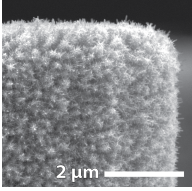
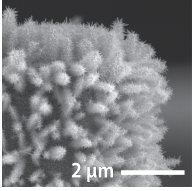
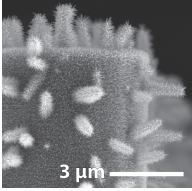
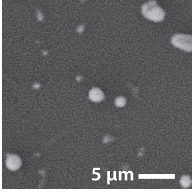
energy for all of the fabricated samples, enabling quantitative comparison of purely geometric effects on the obtained contact angles. On smooth planar samples, this perfluorinated monolayer treatment yielded advancing and receding contact angles with water, hexadecane, octane, and heptane of $117^\circ/92^\circ$, $67^\circ/54^\circ$, $51^\circ/41^\circ$, and $43^\circ/39^\circ$ respectively, consistent with a highly fluorinated surface. Subsequent modification of the surface geometry using the aforementioned technique allowed us to rationally design surfaces with hierarchical scales of texture that maximize the robustness of the composite interface (allowing lower surface tension liquids to be supported in the Cassie-Baxter state) and minimize the contact angle hysteresis (allowing liquid droplets to easily roll from the surface).

A complete list of measured contact angles on the different surfaces fabricated in this work is reported in Table 4.1. The nanostructures were deposited on both planar Si and Si microposts of varying dimensions, hereafter specified by the post diameter \times the edge-to-edge spacing in micrometers. The deep reactive ion etching (DRIE) fabrication method for the microposts produced a characteristic scalloped profile on the vertical surfaces, Figure 4.9.¹⁶⁵ The nanotextures include planar ALD films, unbranched NWs, and branched NWs with decreasing trunk density, as shown in Figures 4.1 and 4.5; hereafter referred to as BNW-3, BNW-4, BNW-5, and BNW-7, with the number referring to the number of TiO_2 cycles in the overlayer.

The spacing ratio, D^* , was calculated for the NWs, BNWs, and hyperbranched arrays. Here, the geometric parameters in Equation 2.5 refer to the size and spacing parameters shown in Figure 4.1. For each level of additional texture, the D^* parameter can be determined by multiplying the D^* values of each individual scale of texture,¹⁰⁰ for example, D^* values for NWs on a micropost array would be $D^*_{microposts} \times D^*_{NWs}$ (Figure 4.1).

Planar ALD-coated Si microposts with low values of D^* ($D^* < 20$) exhibit larger contact angle hysteresis even with the liquids that they are able to support in the

Table 4.1: Contact Angles on Fluorosilvanized Samples with Different Combinations of Microscale Geometries (Planar and Microposts with Varying Spacing) and Nanoscale Geometries (Planar ALD Coatings, Unbranched Nanowires, and Branched Nanowires with Increasing Inter-nanowire Spacing)

	Nanoscale Geometry	Microscale Geometry ¹	Contact Angles ($\theta_{adv}^*/\theta_{rec}^*$, °)			
			Water	Hexadecane	Octane	Heptane
	planar	planar	117/92	67/54	51/41	43/39
		post, 13x32	167/139	163/127	109/0	-
		post, 13x17	167/130	162/120	123/0	-
		post, 23x27	161/116	163/116	116/0	116/0
		post, 23x17	162/109	162/106	122/0	102/0
	NWs	planar	172/166	108/0	-	-
		post, 13x32	169/166	164/131	117/0	-
		post, 13x17	167/163	165/116	158/101	-
		post, 23x27	169/154	165/115	130/0	120/0
		post, 23x17	170/161	162/99	162/99	113/0
	BNW-3	planar	174/168	150/0	-	-
		post, 13x32	170/168	162/128	167/121	-
		post, 13x17	169/167	163/114	163/101	-
		post, 23x27	168/158	160/121	159/103	-
		post, 23x17	170/168	160/99	160/89	94/0
	BNW-4	planar	173/169	161/102	144/0	-
		post, 5x45	172/170	166/156	162/145	160/130
		post, 5x30	172/170	164/152	162/142	159/130
		post, 13x32	171/169	165/146	162/119	161/110
	BNW-5	planar	172/170	164/108	122/0	-
		post, 13x32	171/169	167/149	159/105	-
		post, 13x17	170/167	167/139	159/102	129/0
		post, 23x27	169/162	167/137	157/95	129/0
		post, 23x17	169/165	166/127	158/90	129/0
	BNW-7	planar	174/171	135/0	-	-

¹ Micropost dimensions listed as post radius × edge-to-edge spacing (μm)

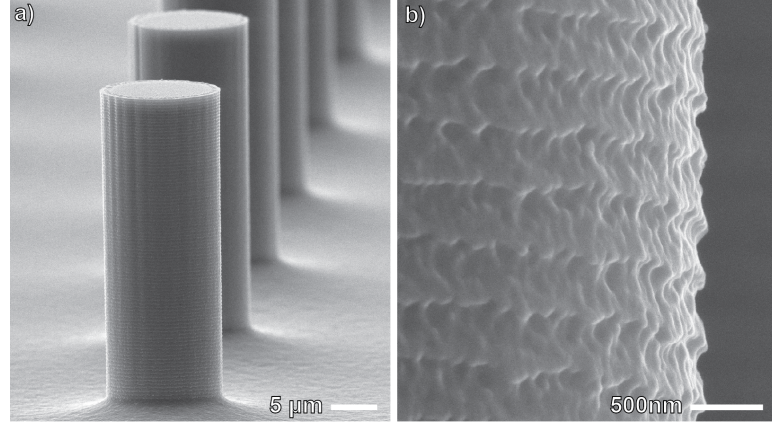


Figure 4.9: a,b) SEM images showing Si micropost arrays used as substrates. The scalloped texture from the cyclic deep reactive-ion etching (DRIE) Bosch process used to create the Si microposts can be seen on the post side walls.

Cassie-Baxter state. Their large planar tops are wetted by the liquids, resulting in a high values of ϕ_s and subsequently larger contact angle hysteresis (for example, $\Delta\theta > 28^\circ$ even for water). These samples are highlighted in Figure 4.10a,b within region i. Generally, contact angles increase and contact angle hysteresis decreases with increasing values of D^* as long as a composite interface is maintained. Samples may be separated into four groups based on their receding hexadecane contact angles, as highlighted in Figure 4.10: (i) contains microposts without nanowires, exhibiting a high hysteresis Cassie-Baxter state with water and hexadecane; (ii) contains nanowires on planar substrates with insufficient re-entrant texture or which are too sparse, exhibiting the Wenzel state with hexadecane; (iii) contains hierarchical structures with lower receding hexadecane contact angles than the nonhierarchical posts in (i), due to nanotexture with insufficient re-entrance being wetted by hexadecane; and (iv) contains hierarchical structures (mostly branched nanowires on microposts) with reduced hysteresis with hexadecane compared to (i).

Adding nonwetted, hierarchical texture significantly reduces the contact angle hysteresis due to the decreased ϕ_s . The optimal samples are those with three levels of hierarchy, including BNW-4s and BNW-5s on microposts, located in region iv

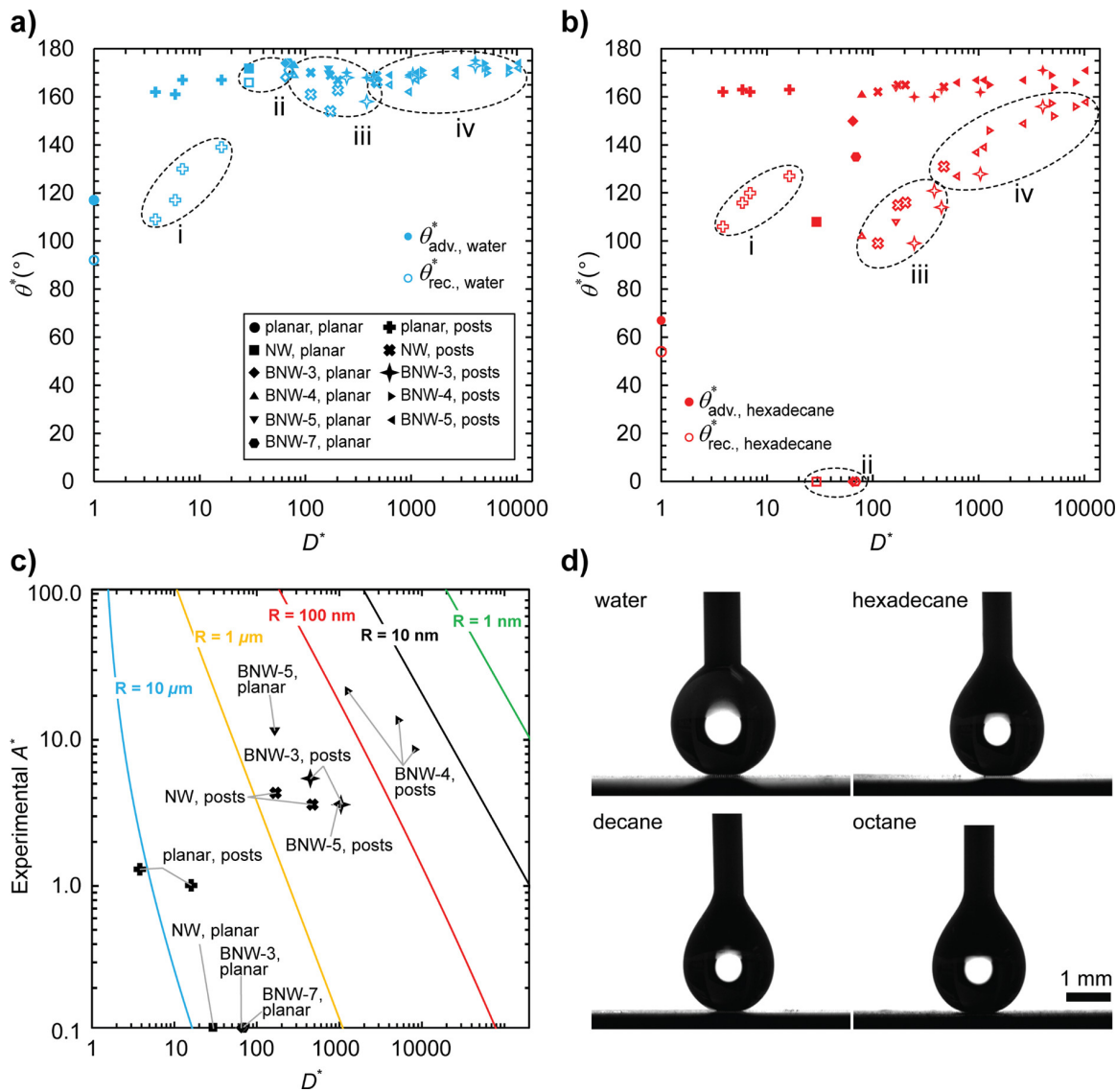


Figure 4.10: Advancing and receding contact angles with (a) water and (b) hexadecane versus the spacing ratio (D^*) for planar, unbranched, and branched NWs of varying density on planar and micropost substrates. (c) Robustness factor A^* measured with hexadecane droplet impact tests versus the spacing ratio D^* . The solid colored lines are theoretical A^* values for hexadecane calculated over varying inter-hoodoo spacing (D) for arrays of hoodoos, each corresponding to a fixed hoodoo cap radius, R (labeled on the plot). (d) Representative photographs from the contact angle goniometer of the advancing contact angles with water, hexadecane, decane, and octane on a sample of BNW-4s on 13×32 posts.

of Figure 4.10a,b. They produce significantly lower contact angle hysteresis with both water and hexadecane than planar ALD on posts ($\Delta\theta$ as low as $\sim 1^\circ$ and 10° , respectively). As a consequence, low surface tension liquids readily roll or even bounce from these surfaces (Figure 4.11b).

For samples with the same type of texture, e.g., planar ALD-coated posts of varying inter-post spacing D , increasing D^* decreases the robustness of the composite interface, following this theoretical trend. To obtain excellent super omniphobicity, it is critical to circumvent this trade-off and simultaneously maximize A^* and D^* . This is done by introducing hierarchical texture; e.g., unbranched nanowires on posts have increased A^* and D^* compared to planar ALD-coated posts, and the A^* and D^* values for BNW-4s on posts, with three levels of hierarchy, are increased even further.

For a hierarchical texture to improve contact angle hysteresis over the microposts alone, the nanotexture itself must exhibit a greater receding contact angle with the liquid than a planar surface. For these highly rough nanotextures, this is equivalent to whether or not they maintain a composite interface with the contacting liquid. Liquids in the Wenzel state on nanowires exhibit effectively zero θ_{rec}^* (e.g., arrays of NWs or BNW-3s on planar substrates in Figure 4.10a,b, region ii). Hierarchical arrays of NWs or BNW-3s on microposts, therefore, exhibit hexadecane contact angle hysteresis values greater than those of planar microposts despite their significantly higher D^* (samples in Figure 4.10a,b region iii). However, as NWs and BNW-3s exhibit a robust composite interface with water, these samples exhibit very low hysteresis and superhydrophobicity compared to that with planar-coated microposts. To achieve low hysteresis super omniphobicity, therefore, it is not sufficient to add nanowires of any arbitrary geometry to a microstructured substrate.

A robust composite interface with very high breakthrough pressure is predicted by high values of the robustness factor ($A^* \gg 1$), while $A^* < 1$ indicates complete wetting. In this work, A^* was determined experimentally by observing the lowest

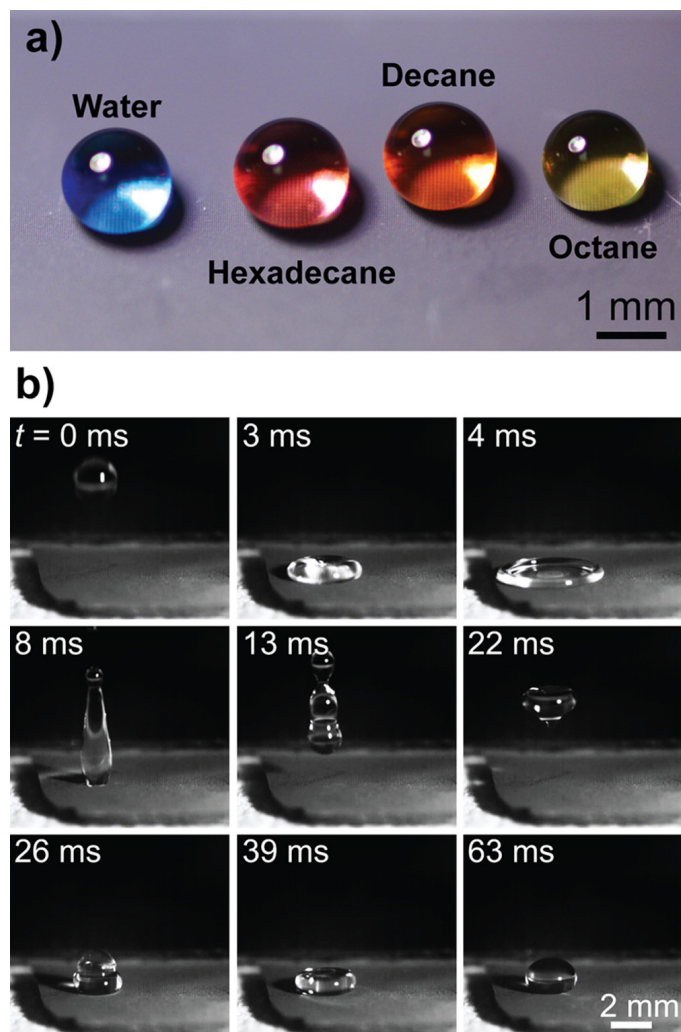


Figure 4.11: (a) Photograph of $\sim 3 \mu\text{L}$ dyed liquid droplets on a micropost array with branched NWs (BNW-4s on 13×32). (b) Frames from a high-speed video of a $\sim 10 \mu\text{L}$ hexadecane droplet completely bouncing from the sample in (a) after being dropped onto it from 5 cm.

surface tension liquid supported in the Cassie-Baxter state, as well as by measuring breakthrough pressures with impacting hexadecane droplets (see Appendix A). If the inherent Young's contact angle (θ) for the contacting liquid on the planar surface falls below the minimum texture angle for a given surface, Ψ_{min} , the Cassie-Baxter state is no longer possible, as the net surface traction points downward into the texture. For example, the unbranched NWs on a planar substrate have a Ψ_{min} close to 90° and therefore only maintain water in the Cassie-Baxter state. On the etched posts ($\Psi_{min} \sim 55^\circ$ due to the scalloped texture on the walls), water and hexadecane are supported in the Cassie-Baxter state, while lower surface tension liquids such as octane ($\gamma_{LV} = 21.6$ mN/m) are in the wetted state (e.g., octane $\theta_{adv}^*/\theta_{rec}^* = 109^\circ/0^\circ$ on 13×32 posts). Therefore, $A^* \gg 1$ for water and hexadecane, while $A^* < 1$ for lower surface tension liquids such as octane. To allow these liquids to be maintained in the Cassie-Baxter state, the Ψ_{min} values for the texture must be reduced.

The addition of a single level of NWs to the micropost arrays leads to an effective reduction in the average Ψ_{min} , as the nanowire tips point horizontally from the post walls. This leads to an increased robustness of the Cassie-Baxter state with lower surface tension liquids, though the contact angle hysteresis for some low surface tension liquids increased relative to the unmodified posts due to wetting of the vertically oriented nanowires on the post tops, as previously discussed. On relatively closely spaced post arrays (lower D^*) with NWs, octane was observed to be in the Cassie-Baxter state ($\theta_{adv}^*/\theta_{rec}^* = 158^\circ/101^\circ$ on 13×17 posts with NWs) but continued to wet sparser arrays ($\theta_{adv}^*/\theta_{rec}^* = 117^\circ/0^\circ$ on 13×32 posts with NWs).

Generally, a higher fraction of downward facing NWs enables the average Ψ_{min} to be closer to 0° , the value for a microfabricated hoodoo structure (on which all liquids with a finite contact should exhibit the Cassie-Baxter state). To demonstrate control over these geometric parameters, we demonstrate that branched NWs with sufficient spacing grown on microposts (Figure 4.7) yielded an increase in robustness

over unbranched NWs on microposts. All post arrays coated in branched NWs yielded the Cassie-Baxter state with octane and some even with heptane, whereas unbranched nanowires on posts with higher spacing were readily wet by octane. On samples with the optimum trunk spacing, (labeled as D_2 in Figure 4.1), even heptane could be supported in the Cassie-Baxter state with low enough hysteresis that it was mobile on the surface ($\gamma_{LV} = 20.1 \text{ mN/m}$, $\theta_{adv}^*/\theta_{rec}^* = 160^\circ/130^\circ$ on 5×45 posts with BNW-4s). However, branched nanowires with denser or sparser trunk spacing (BNW-3 or BNW-5, respectively) yielded reduced robustness, and heptane was found to wet in all cases, again highlighting the need for tunable control of the hierarchical geometry at each length scale.

The results of the hexadecane droplet impact tests correlate with the decreasing surface tension of the liquids supportable in the Cassie-Baxter state (Figure 4.10c). The robustness factor values generally increased from $A^* < 1$ for NWs and BNW-3s on planar substrates, to $A^* \sim 1$ for planar-coated posts, to $A^* > 1$ for the various geometries that were wet only with heptane (unbranched NWs, BNW-3s, and BNW-5s on microposts). The A^* values increased further still for samples with the optimal three levels of hierarchy, that is, with BNW-4 on microposts. Figure 4.11a shows the capability of this optimal surface to support a range of different low surface tension liquids in a robust Cassie-Baxter state. Figure 4.11b shows a hexadecane droplet bouncing completely from this surface, highlighting the low contact angle hysteresis (high D^* values) and high robustness to liquid breakthrough (high A^* values) obtained simultaneously on this optimal surface. The colored lines overlaid on Figure 4.10c are the theoretical A^* predictions for hexadecane calculated for arrays of hoodoos ($\Psi_{min} = 0^\circ$) with different fixed cap radii R , varying values of inter-hoodoo spacing D to yield varying spacing ratio D^* values, $H = 30\mu\text{m}$, and $R_{edge} = 25\text{nm}$. Note that for surfaces with a single scale of texture, such as the micro-hoodoo surface, A^* is inversely proportional to D^* . This is also reflected in the experimental data for

samples with varying micropost geometry but the same nanostructure (e.g., BNW-4s on varying micropost arrays with varying dimensions). Ultimately, Figure 4.10c highlights how careful design and controlled fabrication of hierarchical texture can allow one to overcome this inherent trade-off between contact angle and robustness on surfaces with a single scale of texture and thereby simultaneously maximize both A^* and D^* .

4.3 Conclusion

In conclusion, we demonstrated a method to programmably control individual geometric parameters in multilevel hierarchically branched nanostructures, using ALD to seed NW growth and modify material interfaces. This synthesis enables rational design and control of tunable superomniphobic surfaces, where the geometric parameters associated with feature size, separation, and orientation can be individually controlled for each level of hierarchy. While single-level NW arrays on planar substrates were sufficient to hold water in a Cassie-Baxter state and allow it to bounce off, additional levels of hierarchy were needed to design a surface that could also repel low surface tension liquids such as hexadecane, octane, and heptane. The tunable control over contact angle and contact angle hysteresis demonstrates the power of this synthesis approach for the design and optimization of hierarchical nanosystems, representing a pathway toward programmable nanomanufacturing.

CHAPTER V

Atomic Layer Deposition of Nanostructured Bismuth Vanadate Core-Shell Nanowire Photoanodes

Adapted with permission from Bielinski, A. R.; Lee, S.; Brancho, J. J.; Esarey, S. L.; Gayle, A. J.; Kazyak, E.; Sun, K.; Bartlett, B. M.; Dasgupta, N. P. Atomic Layer Deposition of Bismuth Vanadate Core-Shell Nanowire Photoanodes. *Chem. Mater.* 2019, 31 (9), 32213227. Copyright 2019 American Chemical Society.

5.1 Atomic Layer Deposition of Bismuth Vanadate

Metal oxide semiconductors are attractive for PEC photoelectrodes due to their stability. However, many binary metal oxide semiconductors have high band gaps and suffer from poor electronic properties. This has motivated the move from binary to more complex metal oxides, which increases the number of candidate semiconductors, and enables further tuning of material properties.^{166,167} Among the possible candidate materials, bismuth vanadate, BiVO_4 (BVO) is a promising n-type photoanode material with a 2.4 eV bandgap, an appropriately positive valence band edge for water oxidation, and moderate carrier diffusion lengths.^{168,169}

BVO performance in unmodified planar photoelectrodes is limited by poor carrier transport, surface recombination, and slow water oxidation kinetics.^{107,168,170} These challenges have been addressed using techniques such as doping, designing nanostructured architectures, and incorporating cocatalysts for the oxygen evolution reaction (OER).^{168,170–175} Core-shell nanostructures, in particular, enable increased light absorption through light trapping, and can decouple the length scales associated with absorption and charge separation.^{172,174,176} However, synthesis of rationally-controlled core-shell BVO nanostructures is challenging using traditional vapor deposition techniques, which may suffer from diffusion or line-of-sight limitations when depositing a thin coating layer onto high-aspect-ratio geometries.^{174,177}

To date, attempts to directly deposit BVO by ALD have been limited by the lack of an appropriate bismuth (Bi) precursor.¹⁷⁸ Prior studies used triphenylbismuth (BiPh_3), which has been shown to be unsuitable for depositing binary ALD bismuth oxide films, thus limiting the incorporation of Bi into the ternary BVO films.^{178,179} In order to achieve stoichiometric BVO, the vanadium (V) ALD growth was suppressed, resulting in a low overall film growth rate.¹⁸⁰

To overcome the limitations of BiPh_3 , we report the use of a Bi-alkoxide precursor that has been previously shown to be suitable for direct deposition of Bi_2O_3 by ALD.^{181,182} BVO films were deposited by combining the ALD processes for Bi_2O_3 and V_2O_5 as a nanolaminate of alternating layers using a super cycle approach, as shown in Figure 5.1a. By controlling the relative thicknesses of each layer, the Bi to V ratio can be rationally controlled over a wide range of compositions. The nanolaminate is subsequently annealed in air at 450°C for 2 hours to form crystalline BVO, as shown by the characteristic yellow color in Figure 5.1b. Figure 5.1c shows the high-angle annular dark field scanning transmission electron microscopy image (HAADF-STEM) of as-deposited nanolaminate. Each distinct layer was comprised of either Bi_2O_3 or V_2O_5 with negligible inter-diffusion as confirmed by the elemental map collected with

energy x-ray dispersive spectroscopy (EDS). Annealing the nanolaminate resulted in single-layer BVO grains, as shown in Figure 5.1d. The Bi and V cations in the BVO grains were homogeneously mixed after annealing, with no residual gradients from the original nanolaminate.

5.1.1 Super Cycle Approach to Depositing ALD BVO

ALD of Bi_2O_3 was performed using a bismuth alkoxide precursor, $\text{Bi}(\text{OCMe}_2^i\text{Pr})_3$, and water (further details in Appendix A). The $\text{Bi}(\text{OCMe}_2^i\text{Pr})_3$ was synthesized from BiCl_3 and 2,3-dimethyl-2-butanol following a published procedure.¹⁸² The binary Bi_2O_3 process exhibited a linear growth rate of $0.30 \text{ \AA}/\text{cycle}$. ALD of V_2O_5 was performed using vanadium(V) oxytriisopropoxide and water. A linear growth rate of $0.48 \text{ \AA}/\text{cycle}$ was measured (Figure 5.2). All ALD films were deposited at a substrate temperature of 150°C . The self-limiting ALD growth behavior of the binary oxides, Bi_2O_3 and V_2O_5 , for thermal deposition using these precursors with water as the oxidant has been previously established.^{181–183}

In many cases, the composition of ternary metal oxides deposited by ALD do not follow a simple rule of mixtures based on the growth rates of the binary oxides.¹⁸⁴ This may be attributed to the heterogeneous nucleation of one ALD material on the other, which is dependent on the underlying surface composition, crystal structure, and density of functional groups present. Once each individual layer has coalesced into a dense film, it will typically grow at a constant thickness per cycle, but the nucleation phase can exhibit either higher or lower growth rates than the bulk, leading to non-linearity in compositional mixing with cycle number.⁶³ Additionally, during post-annealing, some elements may be more mobile or volatile than others. This can lead to compositional gradients through the film thickness, as well as changes in overall stoichiometry.¹⁸⁴

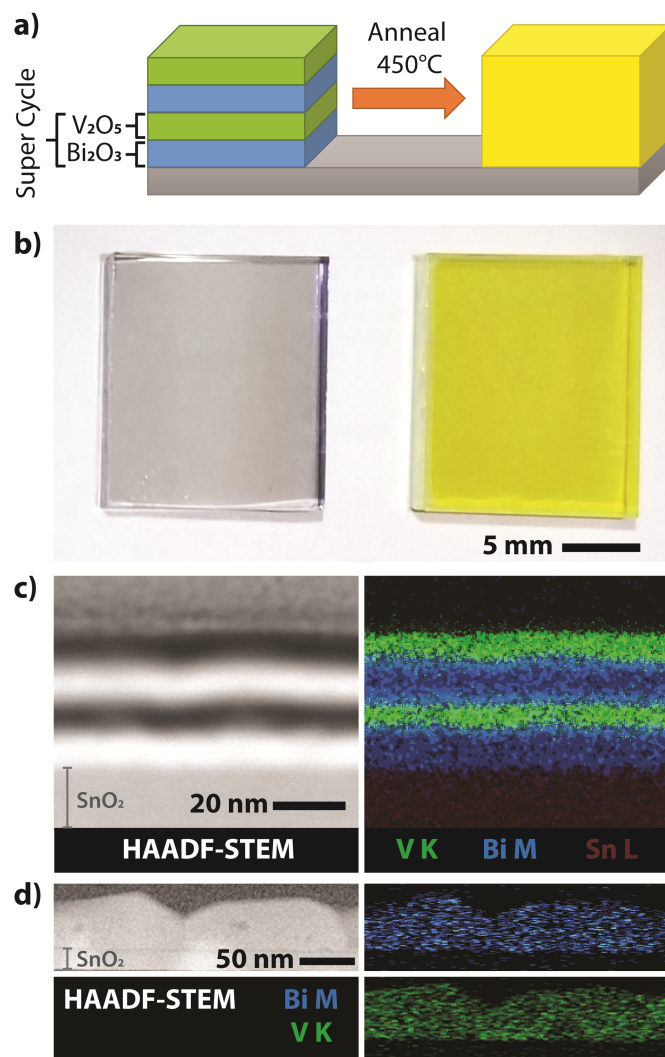


Figure 5.1: a) Super cycle deposition approach for ALD BVO showing the layered structure of binary oxides as-deposited and the post-annealed ternary oxide film. b) Photograph of as deposited (left) and annealed (right) BVO films. The annealed film shows a color transition to the characteristic yellow color of monoclinic BVO. c) Cross-sectional HAADF-STEM image of as deposited structure (left) and EDS elemental mapping (right). Each layer consists of 250 ALD cycles of the binary oxide. d) Cross-sectional HAADF-STEM image of annealed nanolaminate structure (left) and the corresponding EDS elemental mapping (right).

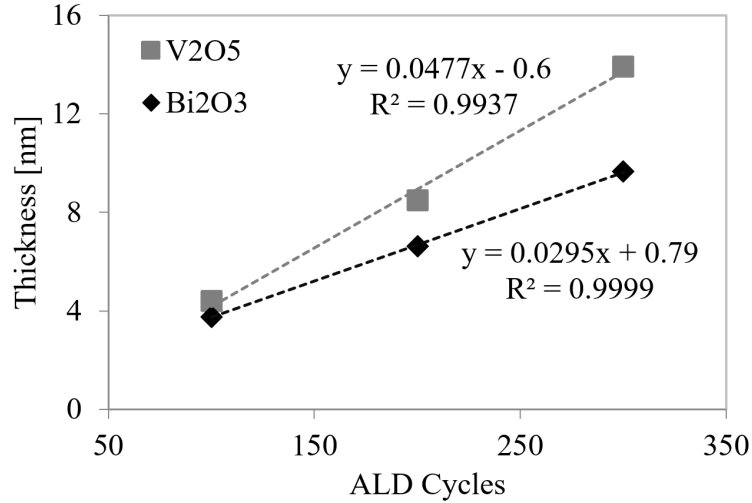


Figure 5.2: Thicknesses of ALD V_2O_5 and Bi_2O_3 films measured via spectroscopic ellipsometry. The linear fit of these data sets shows a growth rate of 0.48 $\text{\AA}/\text{cycle}$ for V_2O_5 and 0.30 $\text{\AA}/\text{cycle}$ for Bi_2O_3 .

Three samples were prepared with 1,000 total ALD cycles, half of which were V_2O_5 and half of which were Bi_2O_3 . However, the samples varied in the super cycle thickness. For the first sample a single super cycle consisted of 10 cycles Bi_2O_3 followed by 10 cycles V_2O_5 (10:10), the second sample was (50:50), and the third was (250:250). Figure 5.3a shows the composition of these samples, measured using XPS. Despite each sample containing 500 total cycles each of V_2O_5 and Bi_2O_3 , the samples with fewer cycles per super cycle contained significantly less Bi. This indicates that ALD Bi_2O_3 has a greater nucleation delay on V_2O_5 . Choosing a super cycle with a larger number of cycles minimizes the nonlinear effects of the nucleation delay when changing the ratio of V_2O_5 to Bi_2O_3 . Therefore, in order to minimize this non-linear effect and maximize overall growth rate, each layer in the nanolaminate film was deposited with sufficient thicknesses such that the Bi_2O_3 growth was predominantly in the steady-state growth regime.

Three film compositions were prepared with different ratios of Bi_2O_3 to V_2O_5 . In the text, these samples will be referred to by the ratio of Bi_2O_3 : V_2O_5 ALD cycles per super cycle. The films were 250:250, 270:230, and 290:210. Each film consisted of 2

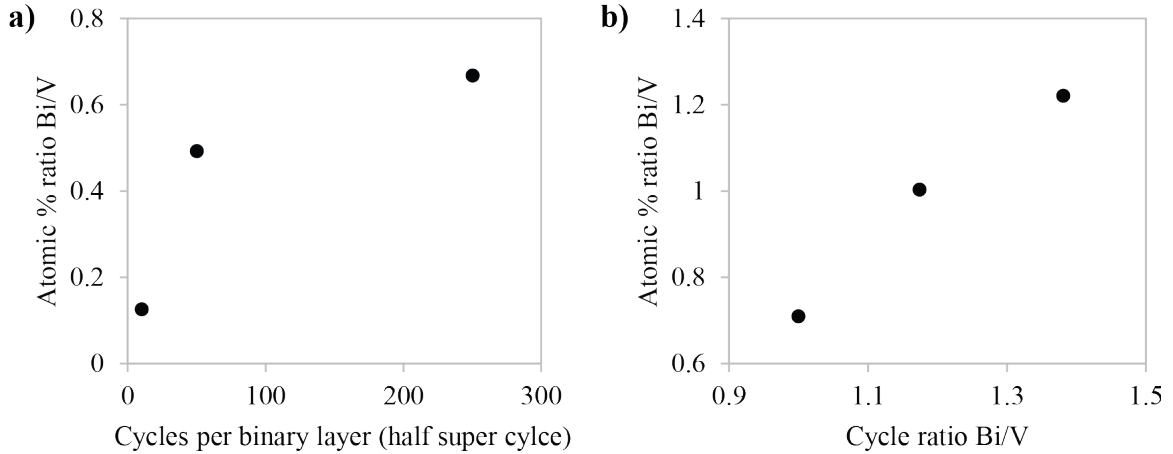


Figure 5.3: Material composition of ALD BVO films as determined by XPS for (a) BVO deposited with different super cycle thicknesses, 10:10, 50:50, 250:250, where all have net 1,000 cycles and (b) BVO deposited with different cycle ratios, 250:250, 270:230, and 290:210, where all have net 1,000 cycles.

super cycles for a total of 1,000 ALD cycles per film. This resulted in binary layers of approximately 6-12nm and total film thicknesses of 39.7 ± 2 nm. X-ray photoelectron spectroscopy (XPS) was used to determine the composition of the annealed films, Figure 5.3b. The 250:250 film was V-rich, the 270:230 film was close to stoichiometric, and the 290:210 film was Bi-rich.

For XPS quantification of the O 1s spectra in the BVO film, the adventitious carbon from the air must first be removed from the surface of the sample, because some of the measured oxygen on the surface is associated with the carbon rather than the BVO. This is typically done via Ar sputtering in the XPS chamber. Unfortunately, in agreement with previously documented observations on ternary bismuth oxide compounds,¹⁶⁷ we observed that Ar^+ ion sputtering inside of the UHV chamber resulted in reduction of Bi^{3+} to Bi^0 . This is observed as a splitting of the Bi 4f peaks as shown below. This may be attributed to either loss of oxygen during sputtering, or changes in the chemical state of oxygen within the material.^{185,186} We know that this is an artifact, as no metallic Bi was ever observed in any diffraction experiments, and

this shift was observed in all films, independent of composition (Bi rich or deficient). Thus, while caution was taken to minimize the sputtering and its effect on the film for the quantification of the Bi and V ratios, the changes in oxygen content in the films cannot be quantified with sufficient precision using XPS. As shown in Figure 5.4, to compliment the XPS spectra, cross-sectional STEM-EDS mapping shows that the oxygen content is uniform throughout the film. This supports that the shift in the Bi core scan during XPS depth profiling is an inevitable artifact of sputtering, and not a compositional gradient in the film itself.

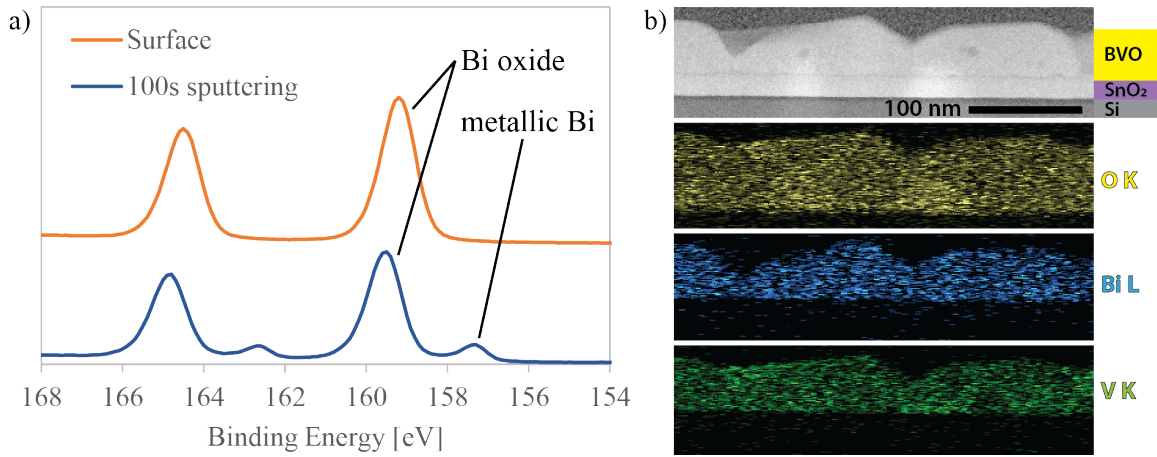


Figure 5.4: Left: XPS Bi 4f peaks (left: Bi 4f_{5/2} and right: Bi 4f_{7/2}) before and after Ar⁺ sputtering to remove adventitious carbon. Right: TEM EDS mapping of O K, Bi L, and V K in the annealed BVO film.

5.1.2 Characterization of ALD BVO

Figure 5.5c shows the optical absorption of the ALD BVO films, measured using UV-vis spectrophotometry. The band gap energy of each film was determined from the Tauc plots, shown in Figure 5.6 assuming an indirect allowed transition ($n = 1/2$) using the relationship in Eq 5.1:

$$(\alpha h\nu)^n = A(h\nu - E_g) \quad (5.1)$$

where α is the measured optical absorption coefficient, $h\nu$ is the photon energy, E_g is the band gap energy, and A is the proportionality constant. Although the band gap energy increased slightly as the Bi content in the films increased, the average transition occurred at 2.5 eV, consistent with the reported band gap of thin-film monoclinic BVO.¹⁸⁷ For 250:250 and 270:230 films, these ~ 40 nm planar ALD films were capable of absorbing more than 60% of photons in the allowed visible range while 290:210 absorbs only about 45% of photons in this range. Figure 5.5a,b shows the reflectance and transmittance spectra of each BVO film.

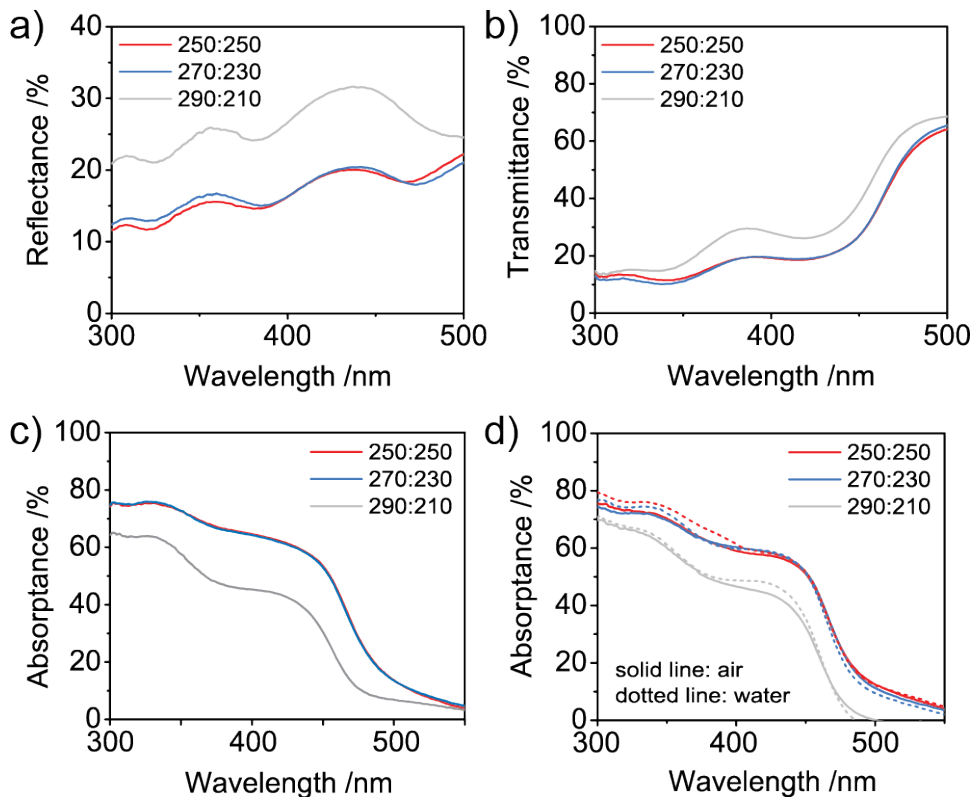


Figure 5.5: (a) Reflectance, (b) transmittance, and (c) absorptance spectra of ALD BVO films of various Bi/V compositions. (d) compares absorptance data of the BVO films collected at air/film (solid line) and at air/glass/water/film (dashed line) interface.

To investigate whether the reflectivity of the ALD BVO films would be different under operating conditions in a quartz cell filled with aqueous electrolyte, the absorptance data of the ALD BVO films were collected from both the air/film interface

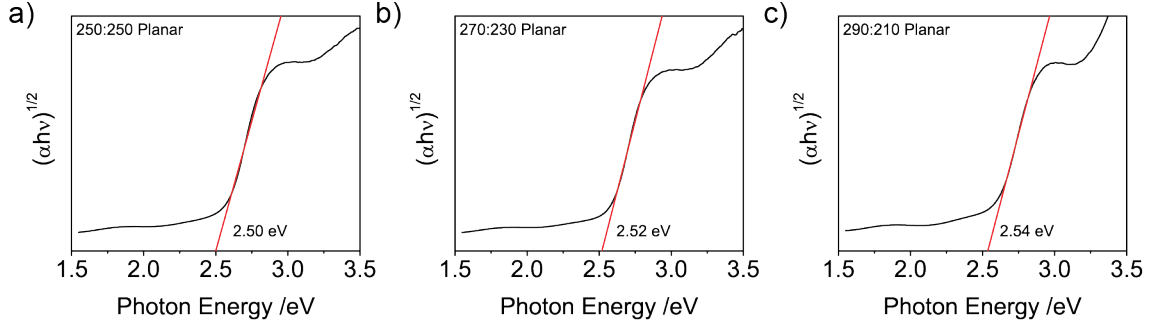


Figure 5.6: Tauc plots of (a) 250:250, (b) 270:230, and (c) 290:210 BVO photoelectrodes.

and a air/glass/water/film interface. The spectra of the air/glass/water/film interface were measured by placing a drop of DI water between the BVO surface and a quartz glass slide and loading the assembly onto the integrating sphere of the UV-vis spectrophotometer. As shown in Figure 5.5d, there were minimal differences in the absorbance of all three BVO films in air and in water.

Grazing incidence x-ray diffraction (GIXRD) measurements demonstrated that the films form the monoclinic phase of BVO after annealing (Figure 5.7), which is known to be the most photoactive phase.¹⁸⁸ In addition to the BVO peaks, the 250:250 film shows a peak associated with the V_2O_5 (010) plane at $20.3^\circ 2\theta$, indicating phase segregation of a V_2O_5 impurity phase. The same V_2O_5 (010) peak is significantly suppressed in the 270:230 sample, and is absent in the 290:210 sample, which is consistent with increasing bismuth content in the film. No peaks associated with crystalline Bi_2O_3 or $Bi_4V_2O_{11}$ phases were detected in the Bi-rich film.

AFM topography images, Figure 5.8a-c, show how composition affects the morphology of the BVO films. The AFM images were analyzed to measure the thickness, roughness, and average grain size of the annealed ALD BVO films on FTO glass substrates with SnO_2 interlayers, as listed in Table 5.1. Roughness and grain size were calculated over a $4 \mu m^2$ scan region. Thickness was calculated by etching a region of the sample with 1M HCl and then measuring the height difference between the

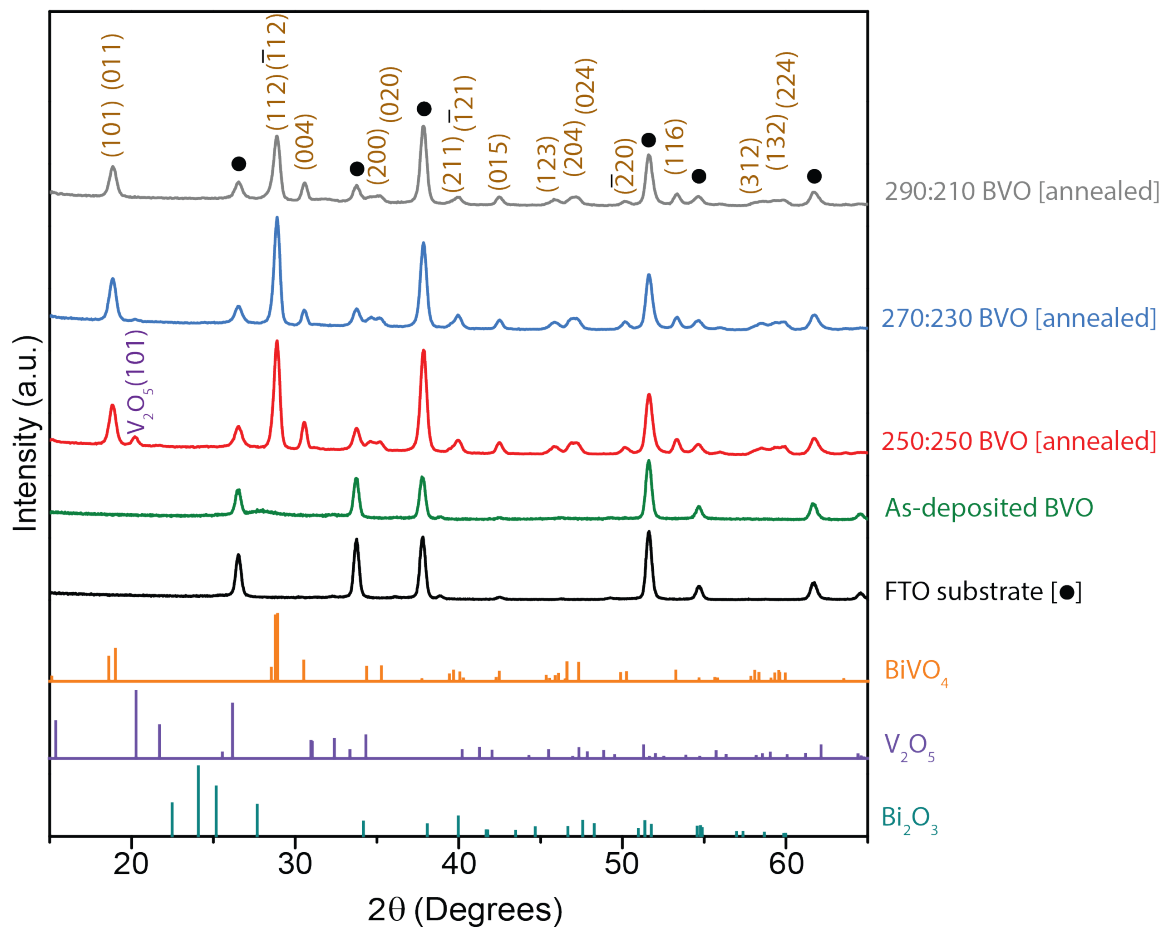


Figure 5.7: GIXRD patterns of 250:250 (red - annealed; green - as-deposited), 270:230 (blue), and 290:210 (gray) films with reference patterns for BVO, V_2O_5 , and Bi_2O_3 . The BVO, V_2O_5 and Bi_2O_3 references are from PDF no. 01-083-1698, 01-072-0598, and #ICSD 169686 respectively.

etched area and the area with the BVO film from an AFM line scan as shown in Figure 5.8e. The 270:230 film has the largest grain size and highest roughness. Additionally, the 250:250 and 270:230 films contain occasional pinholes, while the 290:210 film is continuous.

Table 5.1: Surface roughness, film thickness (height), and grain size of the ALD BVO films annealed on FTO glass substrates.

Sample	RMS Roughness (nm)	Height (nm)	Mean Grain Size (nm)	Standard Deviation Grain Size (nm)
250:250	15.7	37.8	69.3	18.7
270:230	21.6	41.8	86.6	23.2
290:210	12.1	39.4	93.3	24.1

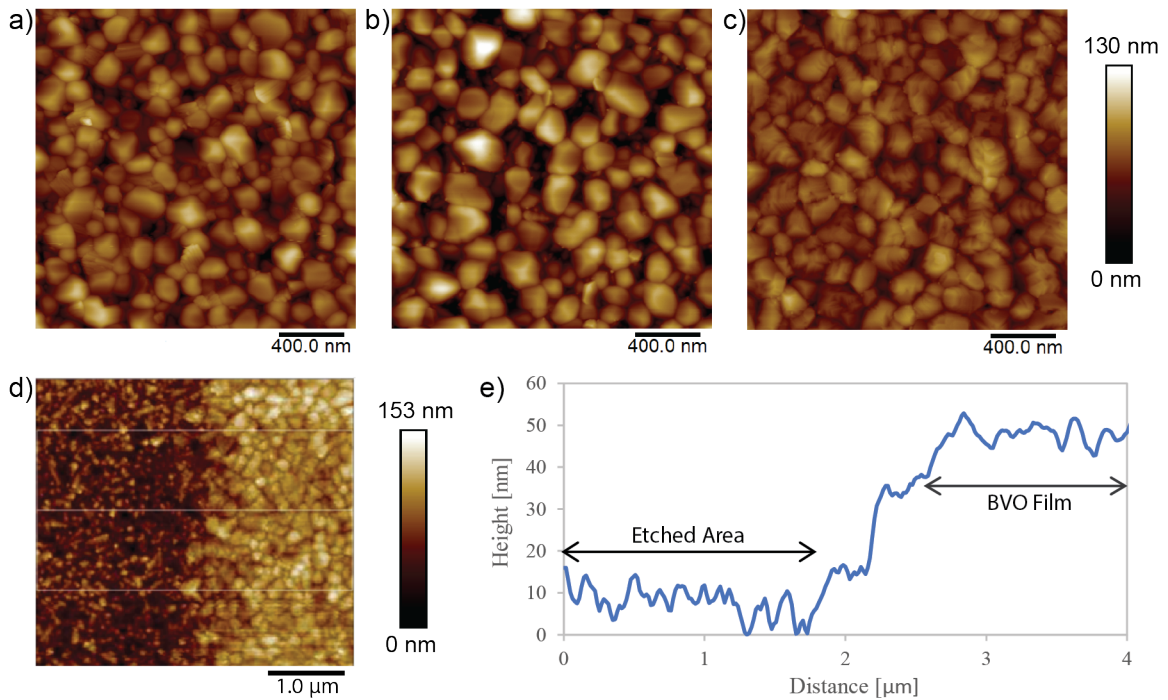


Figure 5.8: AFM for grain size and surface roughness characterization of planar ALD BVO on FTO substrates for BVO samples (a) 250:250, (b) 270:230, and (c) 290:210. AFM (d) area and (e) line scan measurements of 290:210 ALD BVO demonstrating the film thickness measurements.

5.1.3 Photoelectrochemical Performance of ALD BVO

The photoelectrochemical (PEC) performance of the ALD BVO films was evaluated under simulated AM 1.5G illumination in 0.25 M potassium borate buffer (pH 9.2) with 1.0 M Na_2SO_3 as a hole scavenger. SO_3^{2-} ions are thermodynamically and kinetically more facile to oxidize than water. This enables assessment of the BVO films independent from surface recombination losses due to sluggish water oxidation kinetics.^{173,175,189,190} Linear sweep voltammetry (LSV) measurements were performed in a three-electrode configuration with Ag/AgCl as the reference electrode and a Pt wire as the counter electrode. Figure 5.9a shows the current-voltage (J-V) responses of 250:250, 270:230, and 290:210 ALD BVO photoelectrodes.

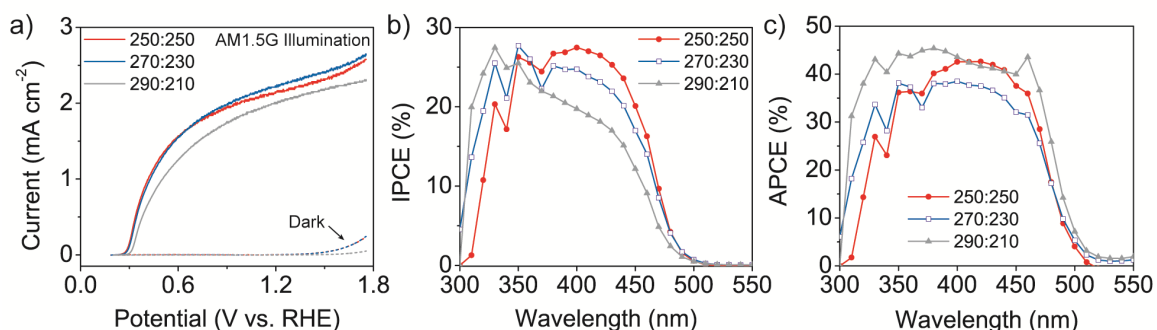


Figure 5.9: Current-voltage (J-V) responses of planar ALD BVO photoelectrodes for sulfite oxidation. (a) Dark (solid line) and illuminated (dashed line) J-V responses of an ALD BVO photoelectrode with 250:250, 270:230, and 290:210 Bi:V pulse ratio collected under AM1.5G front illumination. (b) IPCE and (c) APCE of the same ALD BVO photoelectrodes collected at 0.6 V vs. RHE. The data was obtained under AM1.5 G illumination in 0.25 M potassium borate buffer with 1 M Na_2SO_3 at pH 9.2.

A thin 3nm ALD SnO_2 interlayer was shown to improve the fill factor (FF) in the $j - V$ responses of the ALD BVO photoanodes, Figure 5.10a. The SnO_2 film reduces recombination pathways due to surface defects in the FTO substrate and suppresses dark current due to pinholes in the annealed BVO films.¹⁹¹⁻¹⁹⁴

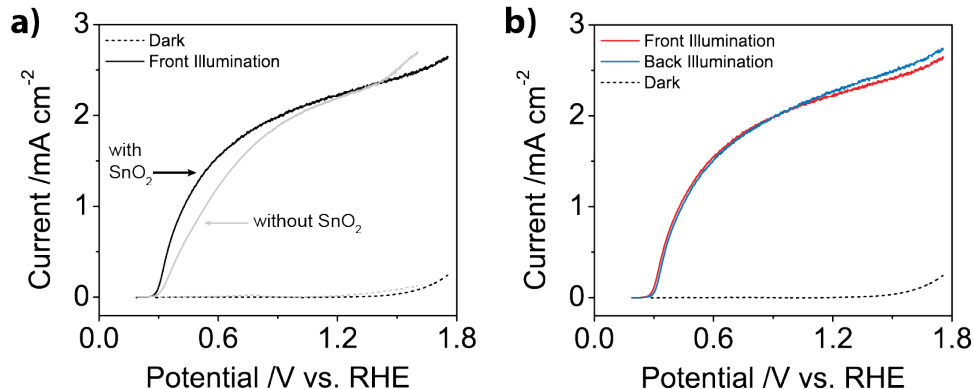


Figure 5.10: LSV of ALD BVO photo electrodes (a) comparing with and without an ALD SnO₂ interlayer and (b) comparing front and back illumination of the working electrode. The data was obtained under AM1.5 G illumination in 0.25 M potassium borate buffer with 1 M Na₂SO₃ at pH 9.2.

The photocurrent density of the 250:250, 270:230, and 290:210 BVO films reached 2.16 mA cm⁻², 2.24 mA cm⁻², and 2.03 mA cm⁻² at a potential of 1.23 V vs. RHE, respectively. The performance of the ALD BVO photoelectrodes in this study is comparable to the photoresponses of planar undoped single-junction BVO in the literature, Table 5.2.^{6,173,175,178,180,195–200} This is the highest photocurrent reported to date in any ALD-deposited photoanode, Table 5.3.^{6,178,180,194,201–208}

BVO is often limited by electron diffusion (electron diffusion length, L_D , <70 nm for single crystal),¹⁶⁹ this typically results in higher photocurrent from back-side illumination through the FTO rather than front-side illumination of the BVO surface.^{178,189,191} However, since the ALD BVO films in this study were on average 40 nm thick, similar photocurrent values were measured from illuminating through the FTO and BVO side, Figure 5.10b, indicating that electron diffusion is not a limiting factor. This illustrates the potential to integrate nanoscale thin films of ALD BVO with photocathode materials, enabling many possible configurations of fully integrated Z-scheme architectures.

To understand the implication of varying the Bi:V ratio in the BVO films, incident photon-to-current efficiency (IPCE) was measured from each BVO electrode.

Table 5.2: Tabulated PEC responses of planar undoped single-junction BVO photoelectrodes.

Type of Preparation	Deposition Method	Test Electrolyte	Film Thickness (nm)	Photocurrent at 1.23 V vs. RHE, AM1.5 G (mA cm ⁻²)	Reference
Vapor phase synthesis	ALD	0.25 M KBi + 1 M Na ₂ SO ₃ (pH 9.2)	~40	2.24	Bielinski et al. 2019 ⁶
		0.5 M KPi + 1 M Na ₂ SO ₃ (~pH 6.8)	55.6	1.17	Stefik et al. 2016 ¹⁷⁸
		1 M KBi + 0.2 M Na ₂ SO ₃ (pH 9.36)	75	1.21	Lamm et al. 2017 ¹⁸⁰
	Reactive ballistic deposition (RBD) in O ₂ ambient	0.5 M Na ₂ SO ₄ + 0.5 M Na ₂ SO ₃	500	~0.4	Berglund et al. 2011 ¹⁹⁵
	Reactive sputtering of Bi ₂ O ₃ and V	1.1 M KPi + 0.5 M Na ₂ SO ₄ (pH 7)	100	0.45	Chen et al. 2013 ¹⁹⁶
	Chemical vapor deposition (CVD) via V ₂ O ₅ and Bi	KPi + 0.1 M Na ₂ SO ₃ (pH 7)	~200	~0.8	Alarcón-Lladó et al. 2014 ¹⁹⁷
Solution phase synthesis	Spin-coating	1 M KPi + 0.1 M Na ₂ SO ₃ (pH 6.8) and 1 M KPi + 0.1 M Na ₂ SO ₃ (pH 12.3)	51.6 ± 3.2	2.2 1.8	Toma et al. 2016 ¹⁹⁸
		0.5 M Na ₂ SO ₄ (pH 6.8)	1500	0.94	Kim et al. 2016 ¹⁹⁹
	Spray pyrolysis	0.5 M K ₂ SO ₄ , KPi + 0.5 M H ₂ O ₂ (pH 5.6)	100	1.8	Abdi et al. 2012 ²⁰⁰
Electrochemical synthesis	Electrodeposition	0.1 M KPi + 0.1 M Na ₂ SO ₃ (pH 7)	~480	1.8-1.9	Seabold et al. 2012 ¹⁷⁵
	Electrodeposition (Nanoporous)	0.5 M KPi + 1 M Na ₂ SO ₃ (~pH 7)	~740	~4	Kim et al. 2014 ¹⁷³

Table 5.3: Tabulated PEC responses of ALD photoanodes.

Photoelectrode	Test Electrolyte	Film Thickness (nm)	Photocurrent at 1.23 V vs. RHE, AM1.5 G (mA cm^{-2})	Reference
BVO	0.25 M KBi + 1 M Na_2SO_3 (pH 9.2)	~40	2.24 (planar)	Bielinski et al. 2019 ⁶
	0.25 M KBi + 1 M Na_2SO_3 (pH 9.2)	~40	2.9 (nanostructure)	Bielinski et al. 2019 ⁶
	0.5 M KPi + 1 M Na_2SO_3 (~pH 6.8)	55.6	1.17 (planar)	Stefik et al. 2016 ¹⁷⁸
	0.25 M KBi + 1 M Na_2SO_3 (pH 9.2)	75	1.21 (planar)	Lamm et al. 2017 ¹⁸⁰
	1 M KBi + 0.2 M Na_2SO_3 (pH 9.36)	30	2.1 (nanostructure)	Lamm et al. 2019 ¹⁹⁴
α -Fe ₂ O ₃	1 M KOH + 0.2 M KCl + H ₂ O ₂ (pH 13.6)	20	0.6 (planar)	Zandi et al. 2014 ²⁰⁶
	0.1 M KPi, 0.2 M KCl + 0.2 M $[\text{Fe}(\text{CN})_6]^{3-/4-}$ (pH 6.9)	60	0.35 (planar)	Klahr et al. 2012 ²⁰¹
	1 M NaOH (pH 13.6)	25	0.5 (planar) 1.6 (nanostructure)	Lin et al. 2011 ²⁰²
	1 M NaOH (pH 13.6)	<10	0.3 (planar)	Steier et al. 2015 ²⁰⁷
WO ₃	1 M KCl/HCl (pH 4)	180	1.8 (planar)	Liu et al. 2011 ²⁰³
	0.1 M Na_2SO_4 (pH 1)	20	0.15 (nanostructure)	Tang et al. 2017 ²⁰⁸
CuWO ₃	0.2 M KCl/KBi (pH 9)	80	0.11 (planar)	Gao et al. 2016 ²⁰⁴

Figure 5.9b shows the IPCE of the BVO films at an applied potential of 0.6 V vs. RHE. In the short wavelength regions (300-350 nm), the quantum efficiency increased as the Bi:V ratio increased, indicating lower surface charge recombination. This could result from differences in the surface roughness (Figure 5.8a-c) and/or improved passivation due to Bi-rich surfaces.^{198,209}

The opposite trend was observed in the long wavelength region (460-500 nm), where the quantum efficiency decreased as the Bi content in the film increased. To further our understanding of the low quantum efficiencies in the long wavelength region, absorbed photon-to-current efficiency (APCE) was calculated from each BVO electrode, taking into account the losses from reflectance and transmittance. Figure 5.9c shows the APCE of the same BVO electrodes, after accounting for light absorption. Interestingly, the 250:250 and 270:230 films preserved the same trend, while the internal quantum efficiency improved for the 290:210 film. This shows that the 290:210 electrode was absorption-limited, which is a result of both higher reflectance and transmittance in the 290:210 sample (Figure 5.5). The thickness of all the BVO films were similar, and there was only a slight decrease in roughness in the 290:210 sample (Table 5.1). Therefore the absorption limitation of the 290:210 film is likely due to differences in chemical composition in the Bi-rich regime, rather than morphology. The ALD BVO photoanodes exhibited moderate stability in borate buffer containing sulfite ions, with a 26% reduction in photocurrent after 2 h illumination, Figure 5.11.

5.2 Nanowire ALD BVO Core-Shell Photoanodes

To demonstrate the potential of ALD to synthesize rationally-designed nanostructured photoelectrodes, core-shell nanowire electrodes were prepared by deposition of ALD BVO onto hydrothermally-grown ZnO nanowire (NW) templates.⁴ ZnO was selected due to simplicity of fabrication, as well as a favorable band alignment to form

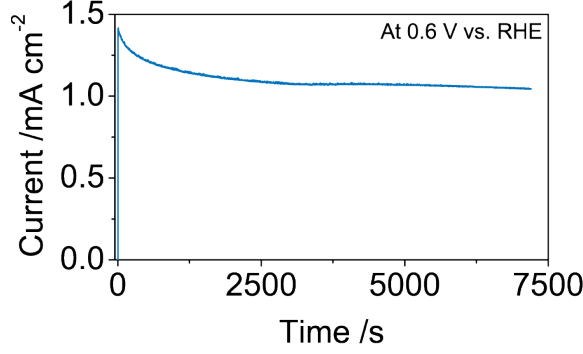


Figure 5.11: Chronoamperometry data collected from a 250:250 BVO photoanode under AM 1.5G illumination in 0.25 M potassium borate buffer containing 1 M Na_2SO_3 (pH 9.2) with an applied potential of 0.6V vs. RHE.

type II heterojunction with BVO, which facilitates electron transfer from the conduction band of BVO to ZnO.^{177,210} The flat band potential (E_{FB}) is generally close to the conduction band edge (E_{CB}) and the Fermi level for n-type semiconductors. Based on the E_{FB} reported for BVO,²¹¹ SnO_2 ,²¹¹ and ZnO,²¹⁰ and the band gap of each material, we constructed a band diagram for the ZnO/ SnO_2 /BVO composite. As shown in the band alignment in Figure 5.12, the SnO_2 is an effective hole-blocking layer for preventing photogenerated holes in BVO from transferring to the valence band (VB) of ZnO and vice versa. The ZnO and SnO_2 used in this work are highly doped in nature, so we do not anticipate a large interfacial resistance for electron transfer from ZnO into FTO.

Furthermore, we do not anticipate a significant contribution to photocurrent from hole injection from ZnO into BVO, due to the large valence band offset between ZnO and SnO_2 , which effectively blocks hole injection across the ZnO- SnO_2 interface. In order to assess the origin of the photocurrent enhancement, the dark as well as illuminated $j - V$ responses of the ZnO nanowire and ZnO nanowire/ SnO_2 photoanodes were compared and contrasted to the nanostructured ALD BVO photoanode, as shown in Figure 5.13a. The maximum photocurrent density obtained from the plain ZnO nanowires was less than 0.5 mA cm⁻² and the value was even lower for the

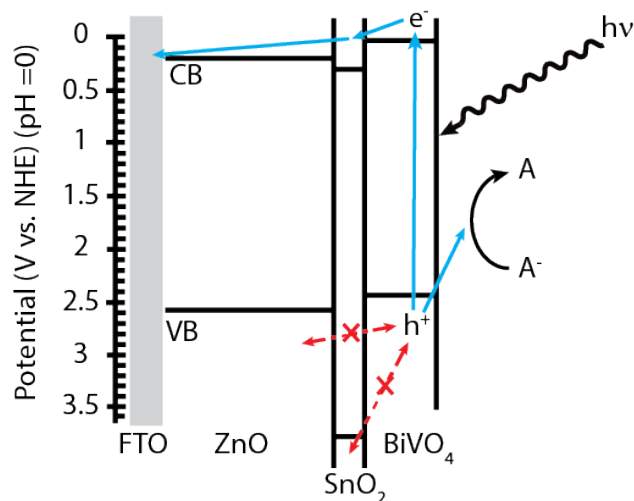


Figure 5.12: Energy diagram of a ZnO/SnO₂/BVO system and the photogenerated charge carrier pathways under solar irradiation.

ZnO nanowire/SnO₂ photoanode under the same experimental conditions. While the long-term stability of ZnO nanowire/SnO₂ improved, Figure 5.13b, the SnO₂ shell also prevented photogenerated holes in ZnO to diffuse to the electrode/electrolyte interface. Within 15 minutes, the photocurrent of the plain ZnO NWs quickly decayed to 85% of the initial value while the photocurrent of ZnO NW/SnO₂ photoanode remained constant. Hence, the contribution from the underlying nanowire template was minimal, and the enhancement observed in the nanostructured ALD BVO was mainly attributed to the 3-D photoelectrode architecture.

Figure 5.14a shows the schematic of an ALD BVO electrode on ZnO NWs with an ALD SnO₂ interlayer. The corresponding SEM and TEM images of this architecture are shown in Figure 5.14b and c, respectively. In the core-shell NW architecture, the ALD SnO₂ interlayer played an additional important role in preventing photocorrosion of underlying ZnO NWs, which further illustrates the power of ALD for interfacial engineering. The nanostructured photoelectrode achieved a photocurrent of 2.9 mA cm⁻² at 1.23 V vs. RHE, a 30% increase relative to the planar architecture.

The increased photocurrent in the core-shell NW geometry is a direct result of increased light absorption, without increasing the required distance for charge carrier

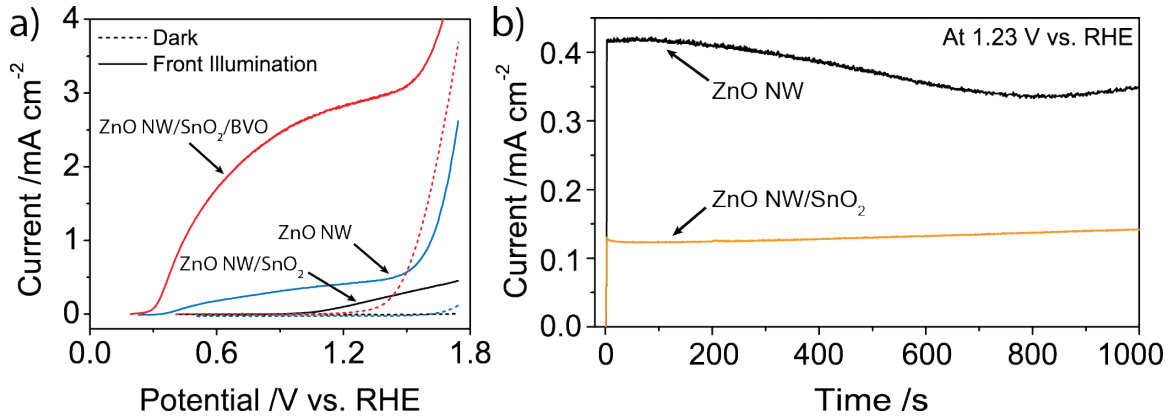


Figure 5.13: (a) Current-voltage ($j-V$) responses of plain, unoptimized ZnO nanowire photoelectrode (blue), ZnO nanowires with 3 nm ALD SnO₂ interlayer (black), and ZnO nanowires/SnO₂/ALD BVO (red) in dark and under AM 1.5G illumination in 0.25 M potassium borate buffer with 1 M Na₂SO₃ (pH 9.2). (b) Chronoamperometry of plain ZnO NW (black) and ZnO NW with 3 nm ALD SnO₂ interlayer (orange) under AM 1.5G illumination in 0.25 M potassium borate buffer with 1 M Na₂SO₃ (pH 9.2)

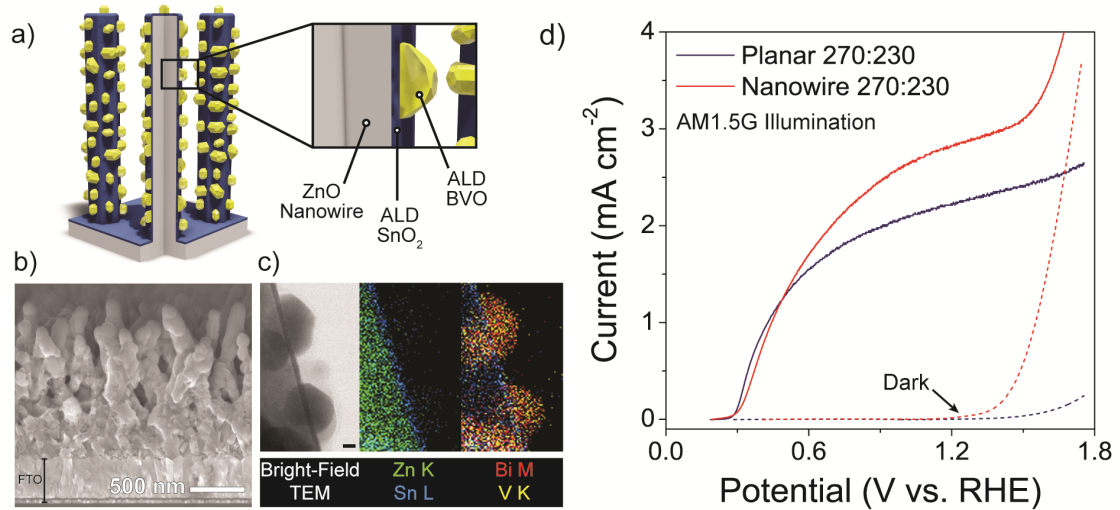


Figure 5.14: a) Diagram of BVO/ZnO nanostructured photoelectrodes with SnO₂ interlayer, b) SEM micrograph of BVO/ZnO photoelectrode, c) Bright-field TEM and EDS mapping of BVO/ZnO photoelectrode, scale bar is 50nm, and d) J-V response of planar BVO and nanostructured BVO/ZnO photoelectrodes under AM1.5G front illumination.

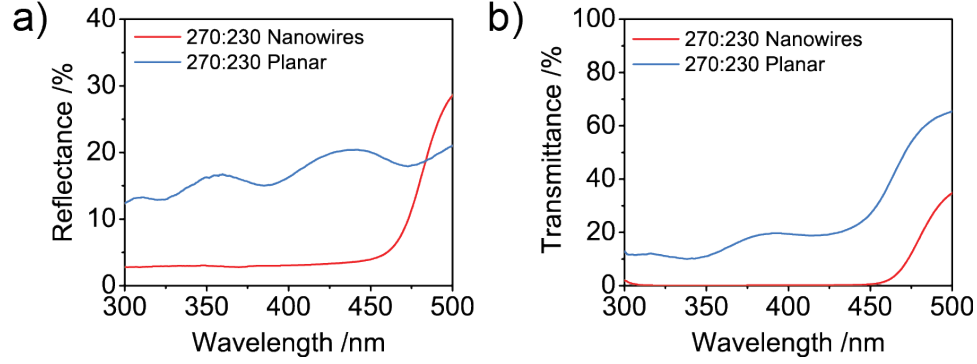


Figure 5.15: (a) Reflectance and (b) transmittance spectra of a planar ALD BVO film and ALD BVO film deposited on ZnO nanowires.

extraction.¹⁶ As shown by UV-vis spectrophotometry, both the reflectance and transmittance of the photoanode decrease in the core-shell NW geometry (Figure 5.15). This highlights the benefits of ALD to decouple the length scales associated with charge extraction and light absorption via highly conformal deposition on 3-D template surfaces.

We note that the ZnO NW and BVO employed in the nanostructured electrode in this study was not optimized in terms of geometry (e.g. NW length and spacing, ALD film thickness) and electronic properties (e.g. dopant concentration). Optimization of the ZnO NW/ALD BVO architecture could be performed to boost light absorption and charge carrier extraction, thus further enhancing the overall PEC performance. Furthermore, the annealed BVO film on the NW surfaces exhibited a slightly larger separation between grains than the planar thin films, despite having the same chemical interface due to the ALD SnO₂ interlayer. At the nanoscale, a curved substrate geometry can influence the nucleation behavior of crystallites, which can affect the morphology of the final film. This can be attributed to several effects, including differences in surface energy, interfacial strain and surface diffusion.^{212,213} This can be seen directly when ALD BVO is annealed on larger ZnO NWs with clear facets from the hexagonal cross-section, as shown in Figure 5.16. The larger ZnO NWs have a hexagonal cross-section due to the wurtzite crystal structure. The BVO can be seen

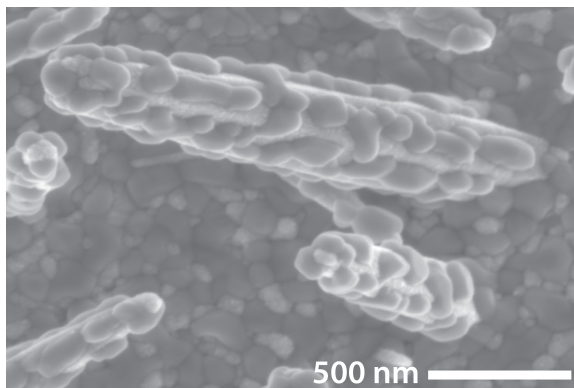


Figure 5.16: A faceted ZnO NW coated with 9 nm ALD SnO₂ and 1 super cycle ALD BVO. The BVO preferentially crystallizes on the flat facets rather than the high curvature edges.

to crystallize preferentially on the flat facets compared to the high curvature edges. We note that similar trends have previously been observed for ALD PbS islands deposited on nanowire surfaces.⁸⁹ Additionally, in the future, integration of an OER co-catalyst materials by ALD will also be essential for uniform catalyst loading on these high aspect ratio structures.

5.3 Optimization of Nanostructure Geometry for Core-Shell ALD BVO Photoanodes

One of the limiting factors in the performance of BVO photoanodes is the electron diffusion length, L_D . For single crystalline BVO, L_D is ~ 70 nm.¹⁶⁹ However, in order to efficiently absorb incident light, the BVO must be many times thicker; to absorb 95% of the incident light the BVO thickness would need to be approximately $10 \times L_D$.^{187,214} To rationally design core-shell nanowire photoanodes, the thickness of the BVO film must be optimized to improve charge carrier collection and the length of the NWs must be optimized to maximize light absorption without detrimental increases in surface or interfacial recombination. Finally, NW array density can be optimized to balance the trade-offs between light absorption, solution mass transport,

and surface area. In addition to maximizing photocurrent, the rational control of these independent parameters will allow insight into the more general limiting factors of nanostructured BVO photoanodes.

Figure 5.17 shows some of the parameters that can be tuned for the ALD BVO core-shell NW photoanodes. Geometric parameters of the ZnO NW array such as length, L , and array density, D , can be controlled using the surface directed assembly approach outlined in chapters III and IV. The thickness of the BVO, t_{BVO} , can be tuned by adjusting the number of ALD super cycles used to deposit the BVO. Different interlayers can be employed to reduce interface recombination and improve charge separation.^{191–194} In this case we continued to use ALD SnO_2 and chose a thickness of $t_{\text{SnO}_2} = 9$ nm based on published results for ALD SnO_2 interlayers.¹⁹⁴ While no overlayers were used in the following electrode designs, overlayers could potentially be employed to suppress surface recombination or improve oxidation reaction kinetics via a co-catalyst.

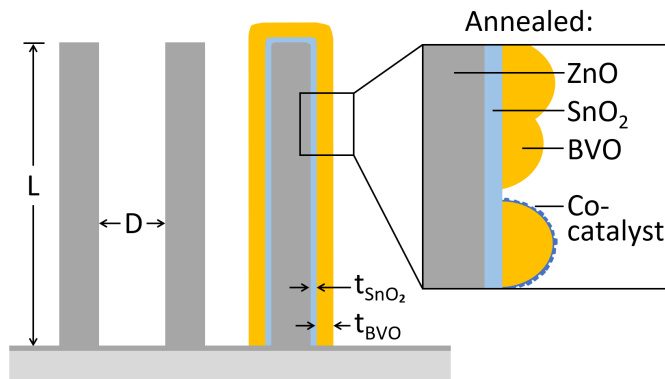


Figure 5.17: Design parameters for a core-shell BVO NW photoanode.

5.3.1 Optimization of BVO Film Thickness

The thickness of the BVO absorber layer was first investigated for planar and NW electrodes using the same NW arrays as used for the initial NW photoelectrode shown in Figure 5.14. Three different thicknesses were tested consisting of 1, 2, and 4 super

cycles which correspond to approximate as deposited thicknesses of 20, 40, and 80nm respectively. Each super cycle consisted of 270 cycles of Bi_2O_3 followed by 230 cycles of V_2O_5 , as optimized in section 5.1.3.

Figure 5.18a shows how the light absorption and photocurrent changes as a function of BVO film thickness. For the planar samples, the BVO light absorption increases with film thickness. As the light absorption increases in the planar samples, the photocurrent also increases, though at a diminishing rate, Figure 5.18b. This indicates that charge transport in the BVO is a limiting factor in the performance of planar BVO films and logically follows the previous discussions of the short average electron diffusion length.

In contrast, all of the NW photoanodes show approximately the same light absorption, though near-gap absorption increases with BVO film thickness. Despite the efficient absorption of the NW photoanode samples and higher number of near-gap photons absorbed by the thicker core-shell BVO films, the photocurrent actually decreases with increasing BVO thickness for the nanowire photoanodes. While as-deposited BVO thickness scales with the number of ALD super cycles, Figure 5.18 c-e shows that the post-annealed BVO films show slightly more complex trends in thickness and morphology. In all cases the BVO forms discrete grains as shown in Figure 5.14 c. The main difference between 1 and 2 super cycles of BVO on the NW substrate is the increase of BVO grain density. The 4 super cycle samples maintains a high grain density similar to the 2 super cycle sample, but the grains increase in size. Additionally, the larger grains in the 4 super cycle NW BVO sample begin to fill in the space between the nanowires. This reduces the surface area in contact with the electrolyte and results in longer transport distances through the BVO, as holes that are generated deeper in the structure must diffuse vertically through the BVO along the length of the NW to reach the top sections that are exposed to the electrolyte. This may contribute to the lower observed photocurrent. This data

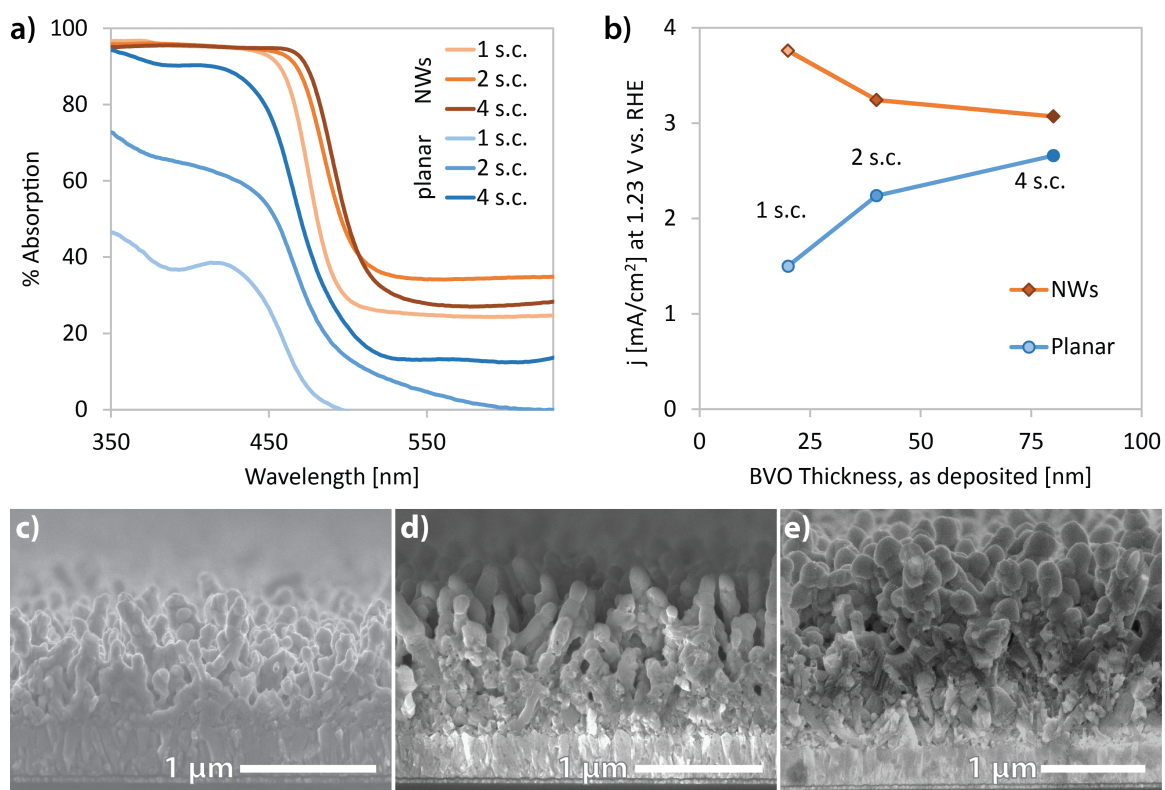


Figure 5.18: a) UV-vis light absorption for planar and NW photoelectrodes with 1, 2, and 4 super cycles of ALD BVO. Each super cycle consisted of 270 cycles of Bi_2O_3 followed by 230 cycles of V_2O_5 . b) Photocurrent at 1.23 V vs. RHE for sulfite oxidation as a function of BVO film thickness for planar and nanowire photoanodes. c-e) Cross-section SEM of ZnO NWs with 1, 2, and 4 super cycles of ALD BVO, respectively.

demonstrates that the core-shell nanowire geometry can overcome the light absorption limitations of thin film ALD BVO and that when utilizing a nanostructured geometry it is beneficial to reduce the BVO film thickness to improve charge transport.

Additionally, ALD is a relatively slow deposition process when compared to other film deposition techniques such as solution based deposition or CVD. It is ideal for very thin films in the range of angstroms to 10's of nanometers, but it is impractical for thicker films. For this reason, it is also important to optimize the film thickness to minimize unnecessary processing time. The main limitation of thinner films is reduced light absorption. Nanostructure optimization can be used to improve light absorption, potentially enabling the use of thinner ALD BVO films with greater or equal performance to thicker planar films.

5.3.2 Optimization of Nanowire Length

Changing the NW length primarily controls light absorption by tuning the light absorption path length through the BVO shell. Growing longer NWs can help overcome light absorption limitations, but longer NWs also increase surface and interface areas, which could potentially increase recombination at those locations. Figure 5.19a shows the light absorption properties and photocurrent response for ALD BVO core-shell NW photoanodes with different NW lengths. The NW length was tuned by changing the hydrothermal growth time ranging from 2 to 255 minutes. The longest, 2.85 μm , NWs were grown with a solution refresh after the first 2.5 hours because the NW growth rate slows as the hydrothermal growth reaction proceeds due to solution depletion.

The light absorption, measured by UV-vis spectroscopy, shows that light absorption first increases with NW length and then saturates. In Figure 5.19a, the near-gap absorption and overall absorption between the BVO and ZnO band gaps increases with NW length up to the 1.41 μm NW sample. After that point the nanowires all

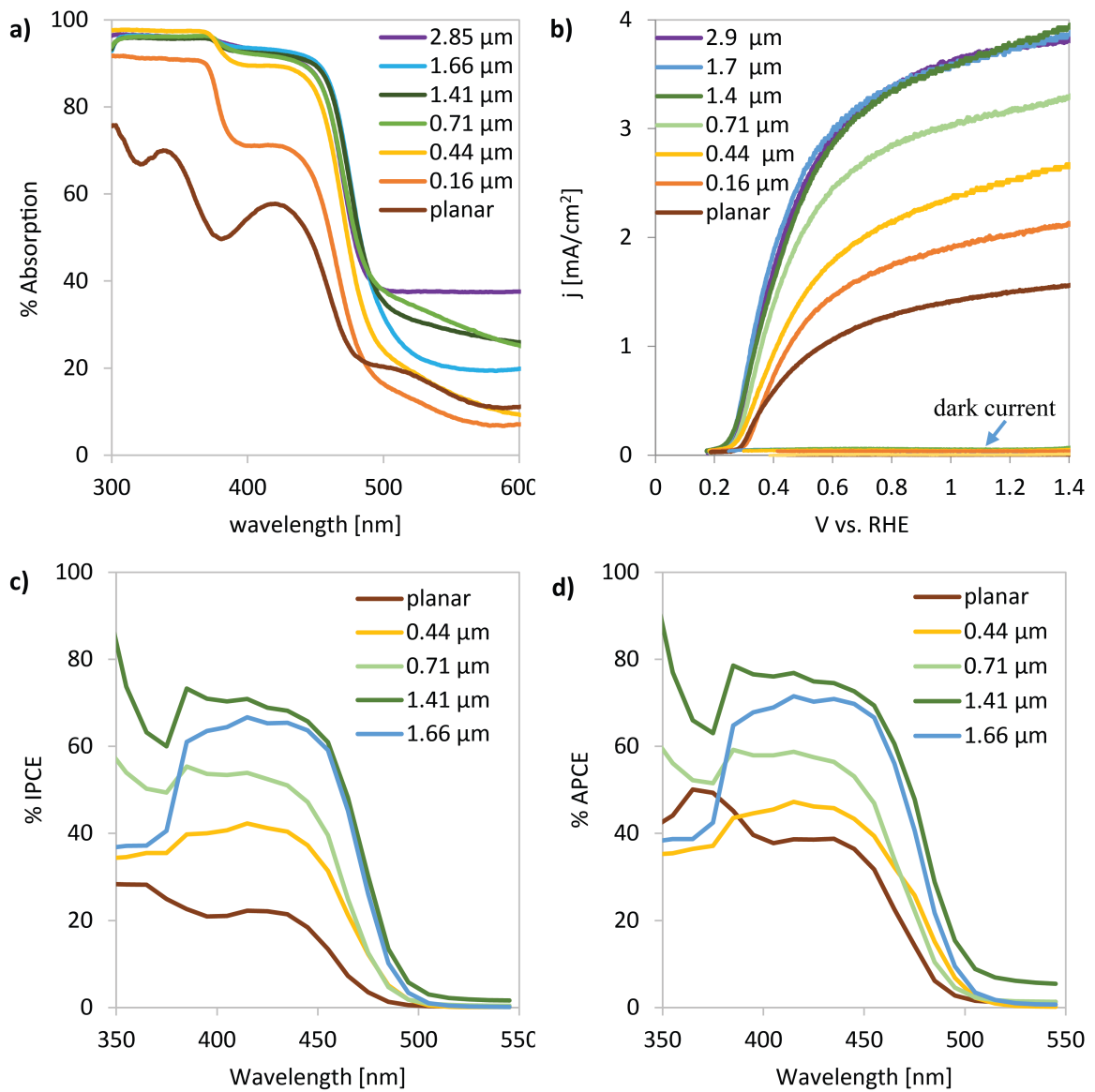


Figure 5.19: a) BVO NW photoelectrode absorption as a function of NW length. b) BVO NW photocurrent as a function of nanowire length for 1-sun illumination and sulfite oxidation (borate buffer, pH 9.2). c) External quantum efficiency, or IPCE, and d) internal quantum efficiency, or APCE, of different length NWs.

show similar light absorption with small deviations likely due to differences in light scattering. As the NWs grow longer they also become more perpendicularly aligned. NWs that deviate from perpendicular alignment terminate due to steric hindrance as the hydrothermal growth procedure progresses. This can be seen in Figure 5.20c-d.

The photocurrent shows a similar trend to the light absorption where the photocurrent first increases with length and then plateaus, Figure 5.19b. However, while there is little increase in light absorption for the 0.71 μm and longer NWs, the photocurrent continues to increase steadily until the next longer sample, 1.41 μm NWs. In addition to overall increased photocurrent, the initial photocurrent onset is shifted to slightly lower potentials for longer NWs. The reduction in overpotential corresponds to the increased surface area. This is in agreement with the Butler-Volmer equation where a reduced exchange current density corresponds to a reduced activation overpotential.¹⁶

Quantum efficiency measurements were performed to further investigate the impact of NW length on photocurrent, Figures 5.19c-d. The external quantum efficiency, or IPCE, shows that the electrodes increase their incident photon to current conversion efficiency as the NWs get longer up to the 1.4 μm NW electrode. This is consistent with the increased photocurrents observed in the j-V data. Additionally, long wavelength IPCE increases with increased NW length, which is consistent with the near-band gap light absorption data. However, while a major benefit of longer NWs is overcoming the light absorption limitation, the internal quantum efficiency, or APCE, data indicates that light absorption is not the only factor contributing to the photocurrent trends. If light absorption was the only factor affecting the performance of the electrodes with different NW lengths, the APCE, which accounts only for absorbed photons, would converge for all electrodes. The differences in APCE between electrodes are smaller than the differences between IPCE for the same electrodes showing that light absorption does play an important role, but the increase in

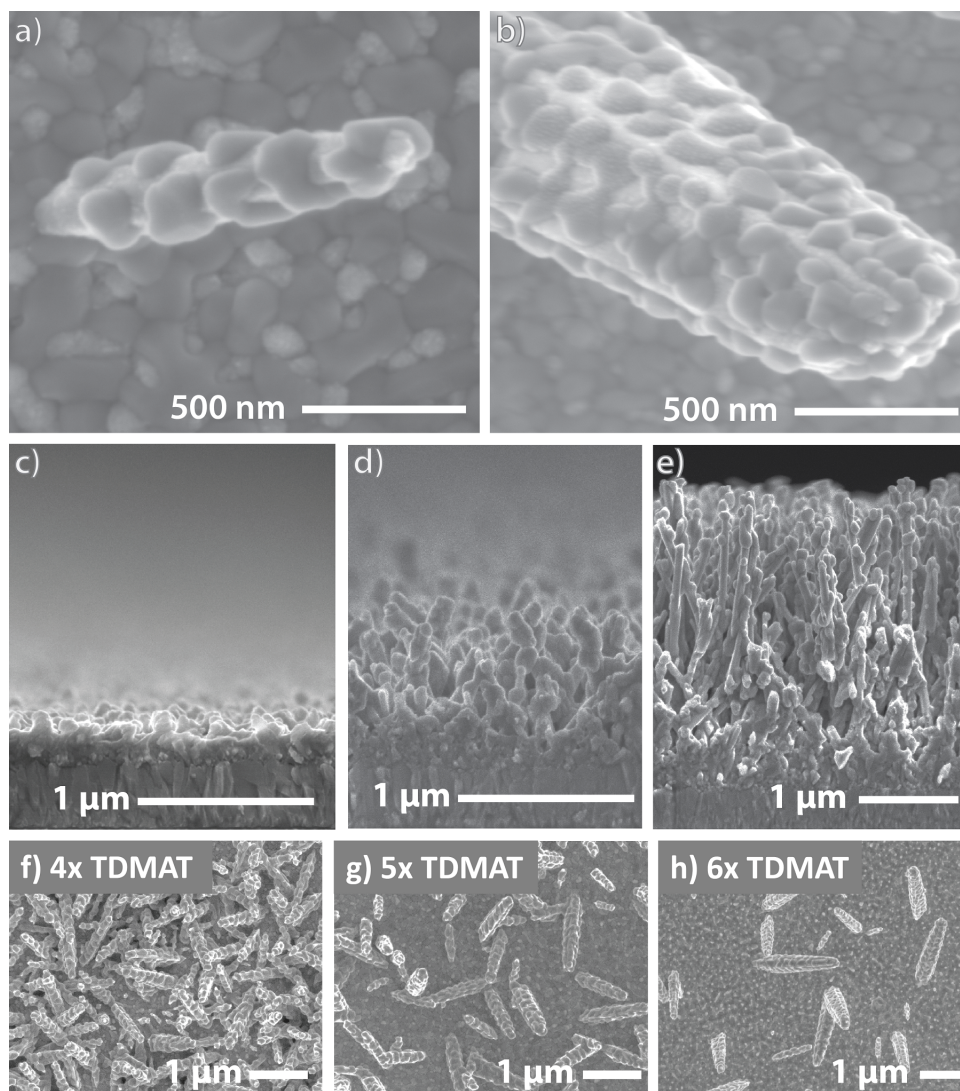


Figure 5.20: a,b) SEM of individual NWs of different sizes showing how the ALD BVO grain morphology differs depending on the NW diameter and faceting. c-e) Cross-section SEM images of 0.16, 0.71, and 2.85 μm ZnO NWs with ALD BVO, as examples of the NW electrodes with different length NWs. f-h) ALD BVO on ZnO NWs with different densities. The NW density was controlled with 4, 5, and 6 cycles TDMAT over the ALD ZnO seed layer, respectively.

APCE with electrode length indicates that another factor such as increased surface area is also a contributing factor. Higher surface area reduces local electron flux. This lowered flux may contribute to effects such as lower surface or interface recombination with longer NW lengths.

The highest photocurrent at 1.23V vs. RHE was 3.76 mA/cm², which is 2.5× higher than the photocurrent for the 1 super cycle planar sample. This is also 1.4× higher than the highest photocurrent achieved with the planar ALD BVO photoanodes. Based on the 2.52 eV band gap for the 270:230 ALD BVO, Figure 5.6, this corresponds to 61% of the maximum theoretical photocurrent under 1 sun illumination. There are some variations in the photocurrent due to the output spectrum of the Xe arc-lamp used to illuminate the samples. While the lamp and electrode position are calibrated to 1-sun intensity, even with a AM 1.5G optical filter, there are some variations in the spectral intensity of the lamp vs. the sun. There are also three potential sources of photocurrent reduction due to charge carrier recombination. First, despite the fast sulfite reaction, there may still be carrier recombination at the electrode surface or interfaces. Second, despite the thin 1 super cycle BVO, electron transport through the BVO is slow and may result in bulk recombination. Third, high energy photons may be absorbed by the ZnO NWs. Due to the band alignment, Figure 5.12, holes generated in the ZnO are unlikely to overcome the potential barrier posed by the SnO₂ valence band to diffuse to the electrode-electrolyte interface. This can be seen in the quantum efficiency measurements where the short wavelength IPCE and APCE decreases for electron energies above the ZnO bandgap at 3.4 eV (365 nm).

5.3.3 Optimization of Nanowire Density

In high density NWs, the BVO can begin to fill in the space between NWs as shown in Figure 5.18e. Additionally, the trade-offs between increased light absorption with

NW length, lower over potentials due to higher surface area, and differences in surface and interface recombination due to higher surface area motivates the independent control of NW density. Lower density NW arrays potentially provide more space for BVO and offer an option for controlling surface area without changing NW length.

Core-shell BVO photoanodes were grown on ZnO NW arrays with different densities. The array density was controlled using TiO₂ overlayers as demonstrated in section 4.1.1. High density NWs were compared to NW arrays prepared with 4, 5, and 6 cycles of ALD TiO₂ deposited with TDMAT and water. Figure 5.21 a,b shows the light absorption and photocurrent for the different NW array density BVO core-shell photoanodes.

The light absorption and photocurrent decrease with decreasing NW array density. Figures 5.20f-h show that for low density arrays, substantial planar regions are exposed. The low density NW arrays absorb light and produce photocurrent at intermediate points between the performance of planar electrodes and high density NW electrodes of the same NW length. Additionally, as a side effect of reducing array density using ALD TiO₂ overlayers, the NW diameter increases with decreasing array density. As discussed in section 5.2, the curvature of the NW affects the morphology of the BVO grains. This also results in slight differences in the BVO morphology on NWs of different diameters as seen in Figure 5.20 a,b.

Quantum efficiency data, Figure 5.21 c,d, show that the external quantum efficiency follows the trend observed in the photocurrent measurements. However, the internal quantum efficiency shows much less variation between the low density NW samples. Compared to the APCE variation for NW electrodes of different lengths, the similarity of the APCE for the NWs of different densities shows that differences in light absorption is a stronger factor for the low density NW photoanodes. The slightly lower APCE for the lowest density 6 cycle ALD TiO₂ NW photoanode could be due to lower surfaces area due to the sparse NW array or it could also be influenced

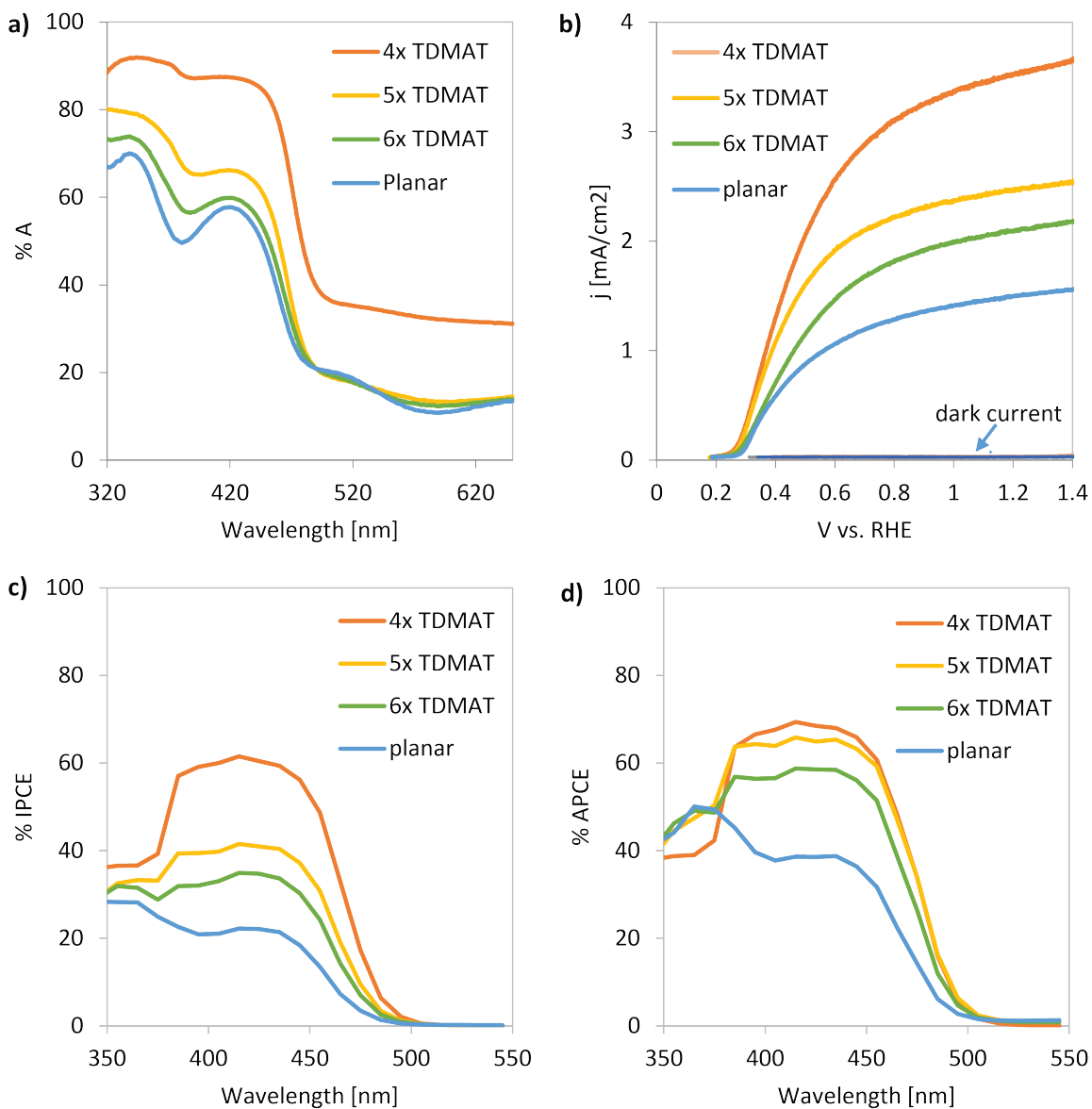


Figure 5.21: a) BVO NW photoelectrode absorption as a function of NW array density. b) BVO NW photocurrent as a function of nanowire array density for 1-sun illumination and sulfite oxidation (borate buffer, pH 9.2). c) External quantum efficiency, or IPCE, and d) internal quantum efficiency, or APCE, of different NW array densities. The legend notation refers to the array density by the number of ALD TDMAT TiO_2 cycles deposited over the ZnO seed layer in the NW synthesis. See Figure 5.20 f-h for a reference of the resultant array density.

by differences in the BVO grain morphology. The larger NWs in this lowest density array have larger flat facets where most of the BVO grains crystallize in a morphology that is similar to that observed on planar samples, Figure 5.20b. In contrast, the intermediate and higher density NWs have small facets that are often smaller than the diameter of the BVO grains. This leads to a slightly different morphology where the BVO grains wrap around the sharp edges of the ZnO NW, Figure 5.20a. Together, light absorption, surface area, and BVO morphology all impact the photocurrent performance of the low density NW photoanodes.

While lower density NWs do not improve performance for sulfite oxidation, they may provide a route to tuning surface area for water oxidation. Future work may also explore low density NWs for branched NW arrays. Branched NWs have even greater surface area and their hierarchical structure may impact light scattering and absorption.

5.4 Conclusion

In conclusion, BVO was deposited by ALD with control of composition and phase. Planar and core-shell nanowire photoanodes were manufactured using ALD BVO absorber layers with integrated SnO₂ buffer layers. The use of a Bi(OCMe₂ⁱPr)₃ precursor resulted in control of the film stoichiometry, and results in an increased overall film growth rate compared to previous studies that have used triphenylbismuth. A photocurrent density of 2.24 mA cm⁻² at 1.23V vs. RHE was observed with a 42nm film, which was increased by an 30% (2.9 mA cm⁻² at 1.23V vs. RHE) on an unoptimized nanowire template. Core-shell nanowire design parameters including BVO film thickness, NW length, and NW geometry were independently varied to investigate their impact on the NW photoanode performance. The optimized geometry resulted in a photocurrent of 3.76 mA cm⁻² at 1.23V vs. RHE. Further increases in the photocurrent could be achieved by doping the BVO film to improve charge transport

and exploring other nanostructured scaffold materials to improve charge separation. Understanding how geometry impacts the performance of BVO photoanodes enables the rational design of electrode geometry for improved performance. The results of this study could be expanded through computational modeling to predict optimal geometries for related photoanode designs such as doped photoanodes with different electronic properties or BVO photoanodes for solar water oxidation.

CHAPTER VI

Conclusions and Future Work

6.1 Conclusions

Tunable thin films and nanostructures allow us to determine how different geometric parameters play a role in device performance. ALD is a powerful tool for modifying surfaces and interfaces. This work demonstrates how, together, ALD directed nanostructure synthesis and ALD surface and interface modification can be used to design functional surfaces for a range of applications including surface wettability and solar energy conversion. This work has contributed the following advancements to the fields of nanostructure synthesis, structural omniphobicity, and visible light photoelectrochemistry:

1. Geometric control of heterogeneous nanostructures using ALD surface modification. This study represents a platform to expand our ability to manufacture integrated systems at the nanoscale, with programmable and scalable synthesis of complex geometries and relative component orientations. Furthermore, by extending a simple and powerful technique such as hydrothermal ZnO NW synthesis to a wide range of flexible, 3-D, high-aspect-ratio, and low-cost substrates, we open up the possibility of engineering these nanoscale systems in useful products that can be scalably manufactured with improved control.

2. A method was developed to programmably control individual geometric parameters in multilevel hierarchically branched nanostructures, using ALD to seed NW growth and modify material interfaces. This synthesis enabled rational design and control of tunable superomniphobic surfaces, where the geometric parameters associated with feature size, separation, and orientation can be individually controlled for each level of hierarchy. The tunable control over contact angle and contact angle hysteresis demonstrates the power of this synthesis approach for the design and optimization of hierarchical nanosystems, representing a pathway toward programmable nanomanufacturing.
3. Thin film deposition of bismuth vanadate, a promising mid-bandgap semiconductor for solar water oxidation, was developed using atomic layer deposition. Charge carrier diffusion is one of the main challenges limiting BVO performance and nanostructuring has been shown to be essential in improving BVO performance. ALD can be used to deposit BVO films with control of composition at thicknesses not limited by carrier diffusion. ALD allows for deposition of BVO on independently controlled nanostructures. This enabled the study of how different geometric parameters affect BVO photoelectrode performance through light absorption, charge transport, and recombination.

6.2 Future Work

This work has provided a toolkit for control of ZnO nanowires and functional ALD films for tunable liquid contact angles and visible light photoelectrochemistry. There are many opportunities to expand on these results. Control of liquid contact angles could be applied to a range of applications such as microfluidics,^{215,216} anti biofouling,^{217,218} or antimicrobial coatings.²¹⁹ Control of geometric parameters such as nanowire size, length, and array density along with control of surface chemistry

could be used to selectively pattern the contact angle and adhesion of different liquids on a substrate. Similarly they could be used to investigate inhibition of different stages of biofouling from microbes to algae colonies.

Rational design of nanostructures by ALD surface modification could also be expanded to other material systems. Many bottom-up nanowire growth processes start with some sort of nucleation layer.⁷ ALD could be investigated for inhibiting, encouraging, or directing the morphology of other solution-based nanowire growth processes. Similarly, processes such as vapor-liquid-solid growth also depend on a patterned catalyst surface. ALD has the potential to control the formation of the catalyst sites such as their size and density by changing the surface wetting properties.

Efforts to further optimize ALD BVO photoanodes could be guided by computational modeling.²²⁰⁻²²² A model encompassing light interactions, electronic properties, and interfacial chemical reactions could be used to help extract the influence of properties such as charge separation, recombination at different locations, mass transport, and light absorption and focusing. This could also direct electrode modifications for the transition from sulfite to water oxidation, which has lower reaction rates and requires different co-catalysts. The development of ALD co-catalysts for nanostructured photoelectrodes would provide a method of evenly loading catalysts on complex 3D structures.^{90,223} ALD processes exist for common catalyst elements and their oxides such as Pt, Ru, Co, Fe, and Ni.

APPENDIX

APPENDIX A

Experimental Methods

Methodology: Analysis Techniques

X-ray Photoelectron Spectroscopy

XPS data was collected on a Kratos Axis Ultra with a delay line detector (Chapter III) or an 8 channel detector (Chapter V) and a monochromated Al source. In Chapter III we report the surface composition of the annealed films as measured after a 60s argon plasma etch step to remove the adventitious surface carbon. Data was analyzed using CasaXPS software.

Ultraviolet-Visible Spectrophotometry

The transmission (%T) and reflectance (%R) spectra of the ALD BVO films were collected in a Shimadzu UV-2600 UV-VIS Spectrophotometer equipped with an integrating sphere. Spectra were referenced to BaSO₄. The absorbance (A%) spectra were then calculated from the transmission and reflectance spectra using Eq. A.1.

$$A\% = 100 - T\% - R\% \tag{A.1}$$

X-ray Diffraction

Synchrotron X-ray Diffraction, Chapters III and IV

Synchrotron x-ray diffraction was performed at the Advanced Photon Source at Argonne National Laboratory using beamline 33-BM. The samples were mounted on a Huber 6-circle diffractometer and the x-ray source was monochromated with an energy of 9.8 keV or 9.4 keV, which is equivalent to wavelengths of 1.265Å or 1.319Å, respectively. The diffracted x-rays were collected with a Pilatus 100K 2D area detector.

GIXRD, Chapter V

GIXRD patterns were collected on a Rigaku SmartLab x-ray diffractometer with an incident angle of 1° and a 2θ range of 15° to 65°. BVO samples for GIXRD were prepared on FTO glass substrates with ALD SnO₂ interlayers to ensure that the crystallization and morphology of the BVO films were the same as the electrodes.

Spectroscopic Ellipsometry

A J.A. Woollam M-2000 ellipsometer was used to measure the thickness of ALD films deposited on Si substrates. Samples were measured from 360-1600nm at 55°, 65°, and 75°. The data was fit to a Cauchy model to calculate film thickness using the J.A. Woollam CompleteEASE[®] software.

Atomic Force Microscopy

Atomic force microscopy (AFM) was performed using a Veeco Dimension Icon AFM to map surface topography. A PeakForce Tapping[®] technique (ScanAsyst[®]) in air was used, in which the AFM probe periodically taps on the sample with a maximum load of tens to hundreds of piconewtons.

For AFM thickness measurements of BVO, a section of the sample was masked using clear Sally Hansen Insta-Dri nail polish color 106 and then allowed to cure for 2+ hours. 1M HCl was used to etch the interface between the masked and unmasked regions of the sample, which was then rinsed with DI water and dried. Acetone was used to remove the nail polish leaving a clean step interface.

Electron Microscopy

Scanning electron micrographs (SEM) were collected on a Tescan Mira 3, a FEI Nova 200 Nanolab, a FEI Helios 650 Nanolab, or a Hitachi SU8000 In-Line SEM.

Planar TEM samples were prepared by using focus ion beam (FIB) in-situ lift-out method performed using a FEI Helios SEM/FIB dual beam system. Nanowire samples were prepared by drop casting a solution of nanowires in ethanol on lacy-carbon film coated TEM grid. For the ZnO seedlayer samples in Figures 3.5 and 3.6, bright-field TEM (BFTEM), high resolution TEM (HRTEM), fast Fourier transform (FFT), and selected area diffraction (SAD) were conducted on ALD ZnO films deposited directly on 18 nm SiO₂ TEM grids using a Cs-corrected JEOL ARM 200cF (cold FEG) producing sub-Å STEM probe with high electron current. CrystalMaker[®] and CrystalDiffract[®] were utilized to simulate interplanar d-spacings of a crystal structure with specific lattice parameters obtained from SAD pattern measurement and corresponding powder diffraction (ring-type for TEM) respectively. For the BVO samples, a JEOL JEM-3100R05 equipped with a cold field emission gun (C-FEG) and double-Cs correctors operated at 300kV in scanning transmission microscopy mode (STEM) and a JEOL TEM F200 with two SDD detectors operated in STEM mode at 200kV were used for both annular dark field (ADF) and bright-field (BF) imaging and EDS element mapping. A 60 mm² SDD detector was used for EDS spectrum and element maps collections.

Photoelectrochemical Experiments

Electrode Preparation

ALD BVO photoelectrodes were fabricated by attaching a tinned-copper wire to and exposed FTO contact area with silver paint (Ted Pella, Inc.). The exposed FTO was prepared by physically removing any nanowires in the contact section with a razor blade and then etching the ALD films with 1M HCl. The etched samples were then rinsed with DI water and dried with compressed air. After the silver paint had dried for 30 minutes, a layer of clear Sally Hansen Insta-Dri nail polish color 106 was applied over the contact section to provide mechanical support to the wire-FTO contact. The nail polish was then allowed to cure for 2+ hours. The wire, contact area and sample edges were sealed with inert epoxy (HysolTM EA, LoctiteTM) to expose approximately 0.6 to 0.7 cm² active area. The epoxy was cured for 24 h at room temperature before the electrodes were used. The curing epoxy often left a small solvent ring around the boarder of the electrode active area. This was removed by rinsing with methanol and then water. A quartz three-electrode cell was used for photoelectrochemical measurements, as shown in Figure 2.9. Ag/AgCl immersed in 3M NaCl (CH Instruments, Inc.) and a coiled Pt wire (23 cm, CH Instruments, Inc.) were used as the reference and counter electrode, respectively.

Electrolyte

An aqueous solution of 0.25 M potassium borate buffered at pH 9.2 (Sigma-Aldrich, Inc.) and 1 M Na₂SO₂ (ACS Reagent, Sigma-Aldrich, Inc.) was used as the test electrolyte. The pH of the electrolyte was measured with a digital pH meter (Mettler-Toledo, Inc.) calibrated with pH 4.00, 7.00 and 10.01 standard buffers.

PEC Linear Sweep Voltammetry Measurements

The linear sweep voltammograms (LSV) were collected with an Interface 1000 Potentiostat (Gamry Instruments, Inc.). A 300 W Xe arc lamp (Newport, Co.) equipped with an AM1.5 G filter (Newport, Co.) and a quartz diffuser (Newport, Co.) was used as the white light source. The illumination intensity was calibrated with a Si photodiode (Hamamatsu Photonics K.K.). The solution iR-drop was compensated at 85% through positive feedback using the Gamry software, which should represent an extrinsic limitation of the electrochemical cell geometry and not an inherent property of the photoelectrodes. The potentials reported in the main text were converted to reversible hydrogen electrode (RHE) using Eq. 2.12a for ease of comparison with the H₂ and O₂ redox levels. The reference electrode potential for a Ag/AgCl electrode in 3M NaCl is $E_{(\text{Ag}/\text{AgCl}, 3\text{M NaCl})} = 0.209 \text{ V vs. NHE at } 25^\circ\text{C}$.

Photoelectrode Quantum Efficiency

The incident photon-to-current conversion efficiency (IPCE) was collected with a lab-built system consisted of a 300 W Xe arc lamp (Newport, Co.) and a $\frac{1}{4}$ -turn single-grating monochromator (Newport, Co.) with a micrometer-adjustable slits. The intensity of the incident light was measured by a Si photodiode (Newport, Co.), and the potential of the BVO photoelectrodes and the absolute current were controlled and measured with an Interface 1000 Potentiostat (Gamry Instruments, Inc.). The readings from the Si photodiode and potentiostat were then fed into a custom-built LabVIEW interface to calculate the IPCE values, as shown in Eq. 2.13. APCE was calculated from the measured IPCE using Eq. 2.14 and the absorbance spectra as calculated from UV-vis using Eq. A.1.

ZnO Nanowire Growth

ALD ZnO Nanowire Seeding

All seedlayers were deposited via ALD using a customized lab-built ALD tool with diethylzinc (Sigma-Aldrich, Inc., 52 wt.% Zn basis) and DI water as the precursors. The reaction chamber was maintained at 150°C and a base pressure of 0.9 Torr. The diethyl zinc was pulsed for 0.05 seconds and the DI water was pulsed for 0.1 seconds. Each pulse was followed by a 30 second Ar purge.

Si substrates were prepared by cleaning Si wafers with Nano-strip[®] (a commercial stabilized mixture of sulfuric acid and hydrogen peroxide, similar to piranha solution) for 10 minutes at 60° and then rinsing and drying thoroughly. ALD ZnO seed layer films on silicon (100) wafers were prepared for subsequent hydrothermal growth with nine different thicknesses of 10, 15, 20, 30, 50, 100, 200, 300, and 600 ALD cycles. The ALD ZnO process has a growth rate of 1.92 Å/cycle as determined by spectroscopic ellipsometry (Appendix A), Figure A.1, so the corresponding film thicknesses are 1.9, 2.9, 3.8, 5.8, 9.6, 19.2, 38.4, 57.6, and 115.2 nm respectively.

ZnO Nanowire Growth Solution Preparation

The zinc oxide NWs were grown using a hydrothermal method⁴⁶, as outlined in section 2.2.2 A solution was prepared by mixing 25 mM zinc nitrate hexahydrate (Sigma-Aldrich, Inc., 98%), 25 mM hexamethylenetetramine (HMTA) (Sigma-Aldrich, Inc., 99%), and 5 mM polyethylenimine (PEI) (Sigma-Aldrich, Inc., average Mw ~25,000 by LS) in DI water. The solution was heated and mixed at 95°C for 30 minutes and then cooled for 45 minutes before filtering. The solution was vacuum filtered at 8, 2, and 0.22 μm consecutively to remove ZnO precipitates before NW growth.

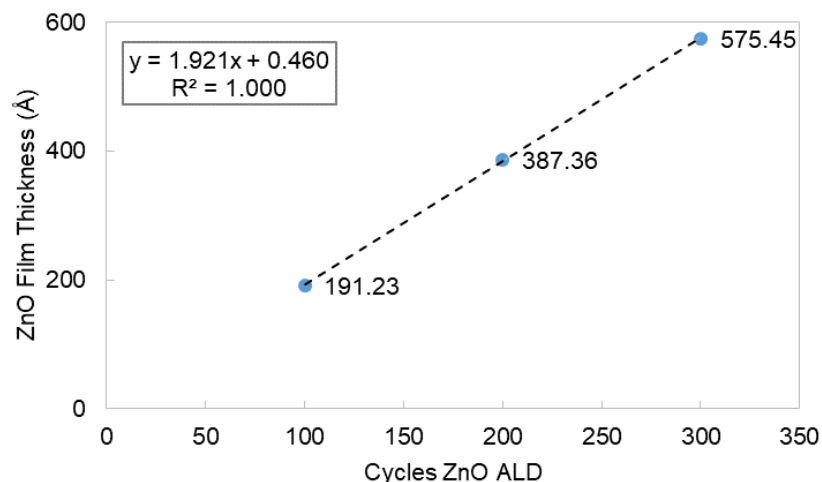


Figure A.1: Ellipsometry on 100, 200, and 300 cycles was used to determine the average growth rate for the ZnO ALD. The growth rate was calculated as $1.92\text{\AA}/\text{cycle}$. The fit was linear least squares with an R value of 1.000 indicating that there is very little variation in the growth rate across cycles and samples.

ZnO Nanowire Growth

Sample substrates were mounted face down on angled PTFE holders and placed in a glass crystallization dish, which was filled with room temperature growth solution and placed on a hotplate, as shown in Figure A.2. Unless a specific growth time or temperature was specified, the NW growth proceeded at 90°C for 1 hour with mixing at 600 rpm. The time was started when the solution reached 90°C . At the end of the growth time the substrates were immediately removed and rinsed with ethanol and then DI water before drying with N_2 or compressed air.

Super Omniphobicity Measurements

Silanization

A final overlayer of 50 cycles of ALD Al_2O_3 was deposited on each sample to prepare the surface for silanization. The samples were then cleaned and activated with oxygen plasma for 30 min (30W, Harrick Plasma PDC-001). To silanize the

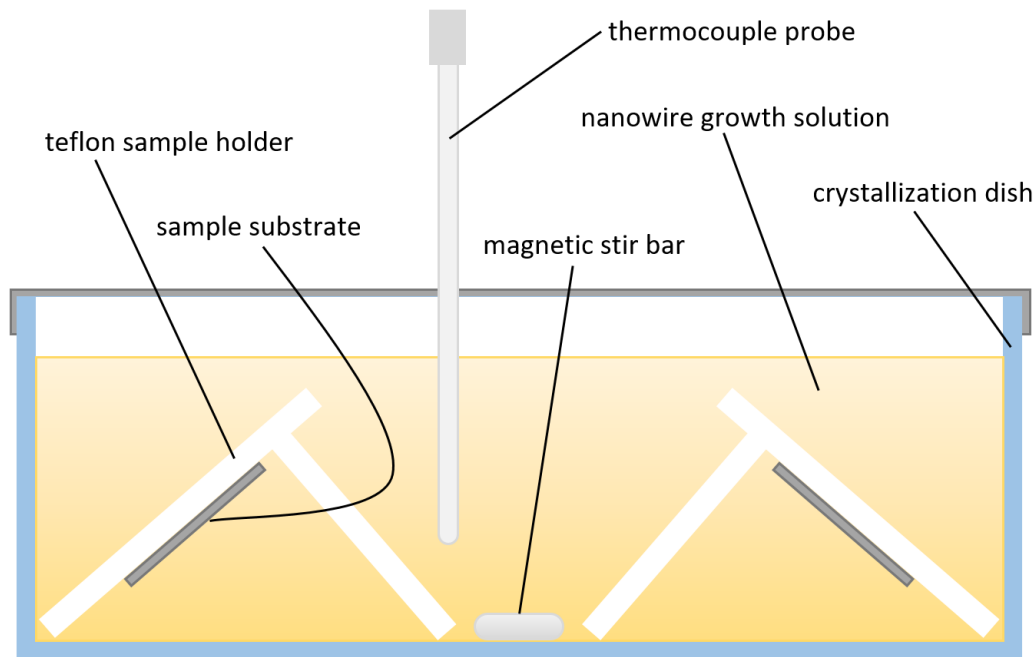


Figure A.2: Diagram of hydrothermal ZnO nanowire growth.

surface, (heptadecafluoro-1,1,2,2-tetrahydrodecyl)-1-trichlorosilane was reacted with the surface via a simple vapor-phase deposition process on a hot plate at 125°C for 2 h while covered. Samples were then rinsed with 2,3-dihydrodecafluoropentane (Dupont Vertrel XF) and isopropyl alcohol (Fisher Scientific) and dried with compressed air prior to measurement.

Contact Angle Measurements

Contact angle measurements were performed with a Ramé-Hart 200-F1 contact angle goniometer using the sessile drop technique. DI water, hexadecane, decane, octane, hexane, and heptane (Fisher Scientific) were used as probe liquids. Advancing and receding contact angles were obtained by measuring the angle while the liquid was slowly added to or removed from a $\sim 3 \mu\text{L}$ droplet in contact with the sample and a micrometer syringe. At least three measurements were performed per sample, and the standard error is $\pm 2^\circ$.

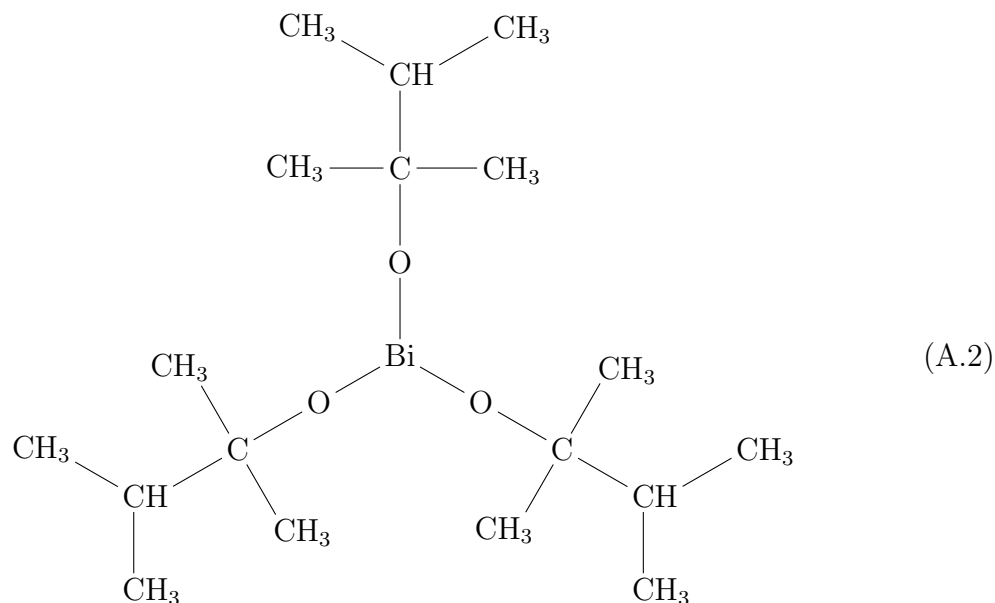
Breakthrough Pressure Measurement

Droplets of hexadecane were released from a measured height above the sample from a micrometer syringe. The droplet impact was recorded with a high-speed camera (Fastec Imaging HiSpec 1). Droplets that did not rebound completely were considered to have exceeded the breakthrough pressure and partially wetted the texture. The minimum pressure exerted by an impinging droplet released from a height h may be estimated by the Bernoulli pressure $P = \rho gh$, where ρ is the density of hexadecane (770 kg/m^3) and g is the acceleration due to gravity. The highest pressure at which droplets completely rebounded was normalized with P_{ref} to yield an experimentally measured robustness parameter A^* for hexadecane on each surface.

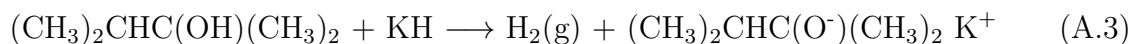
ALD Bismuth Vanadate

Synthesis of $\text{Bi}(\text{OCMe}_2^i\text{Pr})_3$

$\text{Bi}(\text{OCMe}_2^i\text{Pr})_3$, (A.2), was used as the Bi ALD precursor. It was synthesized following the published reactions from Hatanpää et al.¹⁸² The following procedure was developed and refined for increased yield. The $\text{Bi}(\text{OCMe}_2^i\text{Pr})_3$ was synthesized in a N_2 glovebox from 20 mmol BiCl_3 , 60 mmol KH, and 60 mmol 2,3-dimethyl-2-butanol, using anhydrous tetrahydrofuran (THF) as a solvent. Before use, the 2,3-dimethyl-2-butanol was distilled to remove any water.



First the KH was suspended in THF. While mixing continuously, the 2,3-dimethyl-2-butanol was slowly added along the sidewall of the flask and allow to mix for at least 2 hours. This process deprotonates the 2,3-dimethyl-2-butanol and produces H₂ gas and 2,3-dimethyl-2-butoxide, as shown in Equation A.3.



Next, BiCl₃ is suspended in THF. While continuously mixing the BiCl₃, the alkoxide solution is slowly added. The mixture is allowed to react overnight and then a vacuum is applied to expedite the evaporation of the THF. This second reaction step follows Eq. A.4



After the solvent was evaporated, the crude product was sublimated under vacuum at 130°C. The refined product was sublimated a second time to improve purity.

To improve the yield, The KH was added in a slight deficit to ensure that all the KH was consumed in the first step of the reaction. Similarly, the BiCl₃ was added in slight excess to ensure that the alkoxide was fully consumed. Any excess alcohol and BiCl₃ are removed during the evaporation or sublimation steps along with the reaction byproducts such as KCl. This process achieved a 36% yield on average.

ALD Process Conditions

Substrate Preparation: Fluorine-doped tin oxide on glass (FTO, Delta Technologies, $R_s \leq 14\Omega$) was used as a transparent conductive substrate. The FTO was cleaned by sonicating for ten minutes each, once in acetone, twice in isopropanol, and three times in DI water. The FTO was treated with air plasma (Harrick Plasma) for 10 minutes or oxygen plasma for 5 minutes immediately before deposition.

BVO films were deposited in a custom lab-built hot-walled, cross-flow ALD reactor using vanadium(V) oxytriisopropoxide (VTIP, Sigma Aldrich), Bi(OCMe₂ⁱPr)₃, and DI water as the precursors. The VTIP was held at 55°C, the Bi(OCMe₂ⁱPr)₃ was held at 90°C, and the water was held at room temperature. The deposition temperature was 150°C. A vapor boost system was implemented to use argon gas to improve mass transport of the metal precursors into the deposition chamber. The VTIP and Bi(OCMe₂ⁱPr)₃ precursors were exposed to a 0.1s Ar gas pulse as part of the vapor boost system and then dosed for 0.2s into the reactor manifold. After each pulse the system was purged with Ar gas at 300 sccm for 30s for the VTIP and 60s for the Bi(OCMe₂ⁱPr)₃. The water was pulsed for 0.1s and purged with Ar for 30s at 70 sccm. After deposition, the samples were annealed at 450°C. The temperature was ramped up over 30 minutes, held for 2 hours, and then the samples were allowed to cool naturally over the course of approximately 1.5 hours in the closed furnace. SnO₂ films were deposited at 150°C using Tetrakis(dimethylamino)tin(IV) at 65°C and DI water at room temperature as the precursors. The SnO₂ films were annealed at 450°C

for 15 minutes with an 85 minute ramp up time and natural cooling over the course of approximately 1.5 hours.

The uniformity of the ALD Bi_2O_3 was found to be dependent on the purge step in the ALD process. Purge volumes (carrier gas flow rate in sccm multiplied by the purge time) of $60\times$ the typical purge volume for other precursors were found to be necessary to achieve relative uniformity. Due to this limitation, a system with a smaller volume, or optimized purge dynamics would greatly improve the throughput of the ALD BVO process.

BIBLIOGRAPHY

BIBLIOGRAPHY

- [1] Peidong Yang and Jean-Marie Tarascon. Towards systems materials engineering. *Nature Materials*, 11(7):560–563, 2012.
- [2] K. J. Kuhn. Considerations for Ultimate CMOS Scaling. *IEEE Transactions on Electron Devices*, 59(7):1813–1828, 2012.
- [3] Heike Riel, Lars-Erik Wernersson, Minghui Hong, and Jesús A. del Alamo. III–V compound semiconductor transistors from planar to nanowire structures. *MRS Bulletin*, 39(8):668–677, 2014.
- [4] Ashley R. Bielinski, Eric Kazyak, Christian M. Schlepütz, Hee Joon Jung, Kevin N. Wood, and Neil P. Dasgupta. Hierarchical zno nanowire growth with tunable orientations on versatile substrates using atomic layer deposition seeding. *Chemistry of Materials*, 27(13):4799–4807, 2015.
- [5] Ashley R. Bielinski, Mathew Boban, Yang He, Eric Kazyak, Duck Hyun Lee, Chongmin Wang, Anish Tuteja, and Neil P. Dasgupta. Rational design of hyperbranched nanowire systems for tunable superomniphobic surfaces enabled by atomic layer deposition. *ACS Nano*, 11(1):478–489, 2017.
- [6] Ashley R. Bielinski, Sudarat Lee, James J. Brancho, Samuel L. Esarey, Andrew J. Gayle, Eric Kazyak, Kai Sun, Bart M. Bartlett, and Neil P. Dasgupta. Atomic layer deposition of bismuth vanadate core–shell nanowire photoanodes. *Chemistry of Materials*, 31(9):3221–3227, 2019.
- [7] Neil P. Dasgupta, Jianwei Sun, Chong Liu, Sarah Brittman, Sean C. Andrews, Jongwoo Lim, Hanwei Gao, Ruoxue Yan, and Peidong Yang. 25th Anniversary Article: Semiconductor Nanowires – Synthesis, Characterization, and Applications. *Advanced Materials*, 26(14):2137–2184, 2014.
- [8] Ruoxue Yan, Daniel Gargas, and Peidong Yang. Nanowire photonics. *Nature Photonics*, 3(10):569–576, 2009.
- [9] Erik Garnett and Peidong Yang. Light trapping in silicon nanowire solar cells. *Nano Letters*, 10(3):1082–1087, 2010.
- [10] Jinguang Cai and Limin Qi. Recent advances in antireflective surfaces based on nanostructure arrays. *Mater. Horiz.*, 2:37–53, 2015.

- [11] Nicklas Anttu. Absorption of light in a single vertical nanowire and a nanowire array. *Nanotechnology*, 30(10):104004, 2019.
- [12] A. J. Bard and L. R. Faulkner. *Kinetics of Electrode Reactions*, pages 87–134. John Wiley & Sons, Inc., 2001.
- [13] Chong Liu¹, Jinyao Tang, Hao Ming Chen, Bin Liu, and Peidong Yang. A fully integrated nanosystem of semiconductor nanowires for direct solar water splitting. *Nano Letters*, 13(6):2989–2992, 2013.
- [14] Brendan M. Kayes, Harry A. Atwater, and Nathan S. Lewis. Comparison of the device physics principles of planar and radial p-n junction nanorod solar cells. *Journal of Applied Physics*, 97(11):114302, 2005.
- [15] Shu Hu, Matthew R. Shaner, Joseph A. Beardslee, Michael Lichterman, Bruce S. Brunschwig, and Nathan S. Lewis. Amorphous TiO₂ coatings stabilize Si, GaAs, and GaP photoanodes for efficient water oxidation. *Science*, 344(6187):1005–1009, 2014.
- [16] Chong Liu, Neil P. Dasgupta, and Peidong Yang. Semiconductor nanowires for artificial photosynthesis. *Chemistry of Materials*, 26(1):415–422, 2014.
- [17] Liming Zhang, Xiaofei Ye, Madhur Bloor, Andrey Poletayev, Nicholas A. Melosh, and William C. Chueh. Significantly enhanced photocurrent for water oxidation in monolithic Mo:BiVO₄/SnO₂/Si by thermally increasing the minority carrier diffusion length. *Energy & Environmental Science*, 9(6):2044–2052, 2016.
- [18] Y. Xia, P. Yang, Y. Sun, Y. Wu, B. Mayers, B. Gates, Y. Yin, F. Kim, and H. Yan. One-Dimensional Nanostructures: Synthesis, Characterization, and Applications. *Advanced Materials*, 15(5):353–389, 2003.
- [19] T. Thurn-Albrecht, J. Schotter, G. A. Kästle, N. Emley, T. Shibauchi, L. Krusin-Elbaum, K. Guarini, C. T. Black, M. T. Tuominen, and T. P. Russell. Ultrahigh-Density Nanowire Arrays Grown in Self-Assembled Diblock Copolymer Templates. *Science*, 290(5499):2126–2129, 2000.
- [20] Zheng Wei Pan, Zu Rong Dai, and Zhong Lin Wang. Nanobelts of Semiconducting Oxides. *Science*, 291(5510):1947–1949, 2001.
- [21] Jing Yu Lao, Jian Guo Wen, and Zhi Feng Ren. Hierarchical ZnO Nanostructures. *Nano Letters*, 2(11):1287–1291, 2002.
- [22] Lincoln J. Lauhon, Mark S. Gudixsen, Deli Wang, and Charles M. Lieber. Epitaxial core-shell and core-multishell nanowire heterostructures. *Nature*, 420(6911):57–61, 2002.
- [23] Charles M. Lieber. Nanoscale Science and Technology: Building a Big Future from Small Things. *MRS Bulletin*, 28(07):486–491, 2003.

- [24] Lori E. Greene, Matt Law, Joshua Goldberger, Franklin Kim, Justin C. Johnson, Yanfeng Zhang, Richard J. Saykally, and Peidong Yang. Low-temperature wafer-scale production of ZnO nanowire arrays. *Angewandte Chemie - International Edition*, 42(26):3031–3034, 2003.
- [25] Bin Liu and Hua Chun Zeng. Fabrication of ZnO Dandelions via a Modified Kirkendall Process. *Journal of the American Chemical Society*, 126(51):16744–16746, 2004.
- [26] Kimberly A. Dick, Knut Deppert, Magnus W. Larsson, Thomas Mårtensson, Werner Seifert, L. Reine Wallenberg, and Lars Samuelson. Synthesis of branched ‘nanotrees’ by controlled seeding of multiple branching events. *Nature Materials*, 3(6):380–384, 2004.
- [27] Wei Lu and Charles M. Lieber. Nanoelectronics from the bottom up. *Nature Materials*, 6(11):841–850, 2007.
- [28] Matthew J. Bierman, Y. K. Albert Lau, Alexander V. Kirt, Andrew L. Schmitt, Song Jin, Alexander V. Kvit, Andrew L. Schmitt, and Song Jin. Dislocation-Driven Nanowire Growth and Eshelby Twist. *Science*, 320(5879):1060–1063, 2008.
- [29] Jia Zhu, Hailin Peng, A. F. Marshall, D. M. Barnett, W. D. Nix, and Yi Cui. Formation of chiral branched nanowires by the Eshelby Twist. *Nature Nanotechnology*, 3(8):477–481, 2008.
- [30] Bin Liu and Eray S. Aydil. Growth of Oriented Single-Crystalline Rutile TiO₂ Nanorods on Transparent Conducting Substrates for Dye-Sensitized Solar Cells. *Journal of the American Chemical Society*, 131(11):3985–3990, 2009.
- [31] Peidong Yang. Semiconductor nanowire building blocks: From flux line pinning to artificial photosynthesis. *MRS Bulletin*, 37(09):806–813, 2012.
- [32] Lori E. Greene, Matt Law, Dawud H. Tan, Max Montano, Josh Goldberger, Gabor Somorjai, and Peidong Yang. General Route to Vertical ZnO Nanowire Arrays Using Textured ZnO Seeds. *Nano Letters*, 5(7):1231–1236, 2005.
- [33] Zhengrong R. Tian, James A. Voigt, Jun Liu, Bonnie Mckenzie, Matthew J. Mcdermott, Mark A. Rodriguez, Hiromi Konishi, and Huifang Xu. Complex and oriented ZnO nanostructures. *Nature Materials*, 2(12):821–826, 2003.
- [34] Yi Cui, Lincoln J. Lauhon, Mark S. Gudiksen, Jianfang Wang, and Charles M. Lieber. Diameter-controlled synthesis of single-crystal silicon nanowires. *Applied Physics Letters*, 78(15):2214–2216, 2001.
- [35] Zhong Lin Wang. From nanogenerators to piezotronics A decade-long study of ZnO nanostructures. *MRS Bulletin*, 37(09):814–827, 2012.

- [36] Matt Law, Lori E. Greene, Justin C. Johnson, Richard Saykally, and Peidong Yang. Nanowire dye-sensitized solar cells. *Nature Materials*, 4(6):455–459, 2005.
- [37] Michael H. Huang, Samuel Mao, Henning Feick, Haoquan Yan, Yiyang Wu, Hannes Kind, Eicke Weber, Richard Russo, and Peidong Yang. Room-temperature ultraviolet nanowire nanolasers. *Science*, 292(5523):1897–1899, 2001.
- [38] Z.L. Wang and J. Song. Piezoelectric nanogenerators based on zinc oxide nanowire arrays. *Science*, 312(5771):242–246, 2006.
- [39] Hannes Kind, Hao Quan Yan, Benjamin Messer, Matthew Law, and Pei Dong Yang. Nanowire ultraviolet photodetectors and optical switches. *Advanced Materials*, 14(2):158–160, 2002.
- [40] Q. Wan, Q. H. Li, Y. J. Chen, T. H. Wang, X. L. He, J. P. Li, and C. L. Lin. Fabrication and ethanol sensing characteristics of ZnO nanowire gas sensors. *Applied Physics Letters*, 84(18):3654–3656, 2004.
- [41] Lionel Vayssieres. Growth of arrayed nanorods and nanowires of ZnO from aqueous solutions. *Advanced Materials*, 15(5):464–466, 2003.
- [42] Yangyang Zhang, Manoj K. Ram, Elias K. Stefanakos, and D. Yogi Goswami. Synthesis, characterization, and applications of ZnO nanowires. *Journal of Nanomaterials*, 2012:e624520, 2012.
- [43] P. Yang, H. Yan, S. Mao, R. Russo, J. Johnson, R. Saykally, N. Morris, J. Pham, R. He, and H.-J. Choi. Controlled Growth of ZnO Nanowires and Their Optical Properties. *Advanced Functional Materials*, 12(5):323–331, 2002.
- [44] Yanfeng Zhang, Richard E. Russo, and Samuel S. Mao. Femtosecond laser assisted growth of ZnO nanowires. *Applied Physics Letters*, 87(13):1–3, 2005.
- [45] Y. Li, G. W. Meng, L. D. Zhang, and F. Phillipp. Ordered semiconductor ZnO nanowire arrays and their photoluminescence properties. *Applied Physics Letters*, 76(15):2011–2013, 2000.
- [46] Lori E. Greene, Benjamin D. Yuhas, Matt Law, David Zitoun, and Peidong Yang. Solution-Grown Zinc Oxide Nanowires. *Inorganic Chemistry*, 45(19):7535–7543, 2006.
- [47] Zhong Lin Wang. Zinc oxide nanostructures: growth, properties and applications. *Journal of Physics: Condensed Matter*, 16(25):R829, 2004.
- [48] M. H. Huang, Y. Wu, H. Feick, N. Tran, E. Weber, and P. Yang. Catalytic Growth of Zinc Oxide Nanowires by Vapor Transport. *Advanced Materials*, 13(2):113–116, 2001.

- [49] Bin Liu and Hua Chun Zeng. Hydrothermal Synthesis of ZnO Nanorods in the Diameter Regime of 50 nm. *Journal of the American Chemical Society*, 125(15):4430–4431, 2003.
- [50] Jason B. Baxter and Eray S. Aydil. Epitaxial growth of ZnO nanowires on a- and c-plane sapphire. *Journal of Crystal Growth*, 274(3–4):407–411, 2005.
- [51] Sheng Xu, Yaguang Wei, Melanie Kirkham, Jin Liu, Wenjie Mai, Dragomir Davidovic, Robert L. Snyder, and Zhong Lin Wang. Patterned Growth of Vertically Aligned ZnO Nanowire Arrays on Inorganic Substrates at Low Temperature without Catalyst. *Journal of the American Chemical Society*, 130(45):14958–14959, 2008.
- [52] Sheng Xu, Yong Ding, Yaguang Wei, Hao Fang, Yue Shen, Ashok K. Sood, Dennis L. Polla, and Zhong Lin Wang. Patterned Growth of Horizontal ZnO Nanowire Arrays. *Journal of the American Chemical Society*, 131(19):6670–6671, 2009.
- [53] Wen Jun Li, Er Wei Shi, Wei Zhuo Zhong, and Zhi Wen Yin. Growth mechanism and growth habit of oxide crystals. *Journal of Crystal Growth*, 203(1):186–196, 1999.
- [54] Romain Parize, Jérôme Daniel Garnier, Estelle Appert, Odette Chaix-Pluchery, and Vincent Consonni. Effects of Polyethylenimine and Its Molecular Weight on the Chemical Bath Deposition of ZnO Nanowires. *ACS Omega*, 3(10):12457–12464, 2018.
- [55] Steven M. George. Atomic Layer Deposition: An Overview. *Chemical Reviews*, 110(1):111–131, 2009.
- [56] J. W. Elam, D. Routkevitch, P. P. Mardilovich, and S. M. George. Conformal Coating on Ultrahigh-Aspect-Ratio Nanopores of Anodic Alumina by Atomic Layer Deposition. *Chemistry of Materials*, 15(18):3507–3517, 2003.
- [57] Neil P. Dasgupta, Xiangbo Meng, Jeffrey W. Elam, and Alex B. F. Martinson. Atomic Layer Deposition of Metal Sulfide Materials. *Accounts of Chemical Research*, 48(2):341–348, 2015.
- [58] Ville Miikkulainen, Markku Leskelä, Mikko Ritala, and Riikka L. Puurunen. Crystallinity of inorganic films grown by atomic layer deposition: Overview and general trends. *Journal of Applied Physics*, 113(2):021301, 2013.
- [59] Paul Poodt, David C. Cameron, Eric Dickey, Steven M. George, Vladimir Kuznetsov, Gregory N. Parsons, Fred Roozeboom, Ganesh Sundaram, and Ad Vermeer. Spatial atomic layer deposition: A route towards further industrialization of atomic layer deposition. *Journal of Vacuum Science & Technology A*, 30(1):010802, 2012.

- [60] Neil P. Dasgupta, Han-Bo-Ram Lee, Stacey F. Bent, and Paul S. Weiss. Recent advances in atomic layer deposition. *Chemistry of Materials*, 28(7):1943–1947, 2016.
- [61] Riikka L. Puurunen. Surface chemistry of atomic layer deposition: A case study for the trimethylaluminum/water process. *Journal of Applied Physics*, 97(12):121301, 2005.
- [62] Markku Leskelaänd Mikko Ritala. Atomic layer deposition (ALD): from precursors to thin film structures. *Thin Solid Films*, 409(1):138–146, 2002.
- [63] Christoph W. Wiegand, Rene Faust, Alexander Meinhardt, Robert H. Blick, Robert Zierold, and Kornelius Nielsch. Understanding the growth mechanisms of multilayered systems in atomic layer deposition process. *Chemistry of Materials*, 30(6):1971–1979, 2018.
- [64] Riikka L. Puurunen and Wilfried Vandervorst. Island growth as a growth mode in atomic layer deposition: A phenomenological model. *Journal of Applied Physics*, 96(12):7686–7695, 2004.
- [65] Zsófia Baji, Zoltán Lábadi, Zsolt E. Horváth, György Molnár, János Volk, István Bársony, and Péter Barna. Nucleation and growth modes of ALD ZnO. *Crystal Growth & Design*, 12(11):5615–5620, 2012.
- [66] Raul Zazpe, Martin Knaut, Hanna Sopha, Ludek Hromadko, Matthias Albert, Jan Prikryl, V. Gärtnerová, Johann W. Bartha, and Jan M. Macak. Atomic Layer Deposition for Coating of High Aspect Ratio TiO₂ Nanotube Layers. *Langmuir*, 32(41):10551–10558, 2016.
- [67] Oili M.E. Ylivaara, Xuwen Liu, Lauri Kilpi, Jussi Lyytinen, Dieter Schneider, Mikko Laitinen, Jaakko Julin, Saima Ali, Sakari Sintonen, Maria Berdova, Eero Haimi, Timo Sajavaara, Helena Ronkainen, Harri Lipsanen, Jari Koskinen, Simo-Pekka Hannula, and Riikka L. Puurunen. Aluminum oxide from trimethylaluminum and water by atomic layer deposition: The temperature dependence of residual stress, elastic modulus, hardness and adhesion. *Thin Solid Films*, 552:124 – 135, 2014.
- [68] Jiyeon Kim, Tomi Iivonen, Jani Hämäläinen, Marianna Kemell, Kristoffer Meinander, Kenichiro Mizohata, Lidong Wang, Jyrki Räisänen, Radim Beranek, Markku Leskelä, and Anjana Devi. Low-temperature atomic layer deposition of cobalt oxide as an effective catalyst for photoelectrochemical water-splitting devices. *Chemistry of Materials*, 29(14):5796–5805, 2017.
- [69] Chaiya Prasittichai, Jason R. Avila, Omar K. Farha, and Joseph T. Hupp. Systematic Modulation of Quantum (Electron) Tunneling Behavior by Atomic Layer Deposition on Nanoparticulate SnO₂ and TiO₂ Photoanodes. *Journal of the American Chemical Society*, 135(44):16328–16331, 2013.

- [70] Wenjing Dong, Chanyan Huang, Tiaoxing Wei, Yun Zhang, Kenan Zhang, Yan Sun, Xin Chen, and Ning Dai. Nondestructively decorating surface textured silicon with nanorod arrays for enhancing light harvesting. *physica status solidi (a)*, 210(12):2542–2549, 2013.
- [71] Jeong-Seok Na, Bo Gong, Giovanna Scarel, and Gregory N. Parsons. Surface Polarity Shielding and Hierarchical ZnO Nano-Architectures Produced Using Sequential Hydrothermal Crystal Synthesis and Thin Film Atomic Layer Deposition. *ACS Nano*, 3(10):3191–3199, 2009.
- [72] Mikhail Ladanov, Paula Algarin-Amaris, Pedro Villalba, Yusuf Emirov, Garrett Matthews, Sylvia Thomas, Manoj K. Ram, Ashok Kumar, and Jing Wang. Effects of the physical properties of atomic layer deposition grown seeding layers on the preparation of ZnO nanowires. *Journal of Physics and Chemistry of Solids*, 74(11):1578–1588, 2013.
- [73] Jn Ding, Yb Liu, Cb Tan, and Ny Yuan. Investigations into the impact of various substrates and ZnO ultra thin seed layers prepared by atomic layer deposition on growth of ZnO nanowire array. *Nanoscale Research Letters*, 7(1):368, 2012.
- [74] Chuanwei Cheng, Bin Yan, She Mein Wong, Xianglin Li, Weiwei Zhou, Ting Yu, Zexiang Shen, Hongyu Yu, and Hong Jin Fan. Fabrication and SERS Performance of Silver-Nanoparticle-Decorated Si/ZnO Nanotrees in Ordered Arrays. *ACS Applied Materials & Interfaces*, 2(7):1824–1828, 2010.
- [75] X. L. Li, C. Li, Y. Zhang, D. P. Chu, W. I. Milne, and H. J. Fan. Atomic Layer Deposition of ZnO on Multi-walled Carbon Nanotubes and Its Use for Synthesis of CNT–ZnO Heterostructures. *Nanoscale Research Letters*, 5(11):1836–1840, 2010.
- [76] Richard W. Johnson, Adam Hultqvist, and Stacey F. Bent. A brief review of atomic layer deposition: From fundamentals to applications. *Materials Today*, 17(5):236–246, 2014.
- [77] Jeffrey W. Elam, Neil P. Dasgupta, and Fritz B. Prinz. ALD for clean energy conversion, utilization, and storage. *MRS Bulletin*, 36(11):899–906, 2011.
- [78] Eric Kazyak, Kevin N. Wood, and Neil P. Dasgupta. Improved cycle life and stability of lithium metal anodes through ultrathin atomic layer deposition surface treatments. *Chemistry of Materials*, 27(18):6457–6462, 2015.
- [79] JA Van Delft, D Garcia-Alonso, and WMM Kessels. Atomic layer deposition for photovoltaics: applications and prospects for solar cell manufacturing. *Semiconductor Science and Technology*, 27(7):074002, 2012.
- [80] Do Han Kim, Mark D. Losego, Qing Peng, and Gregory N. Parsons. Atomic layer deposition for sensitized solar cells: Recent progress and prospects. *Advanced Materials Interfaces*, 3(21):1600354, 2016.

- [81] Ching Lin, Feng-Yu Tsai, Min-Hsueh Lee, Chia-Hua Lee, Ta-Chang Tien, Lih-Ping Wang, and Song-Yeu Tsai. Enhanced performance of dye-sensitized solar cells by an Al_2O_3 charge-recombination barrier formed by low-temperature atomic layer deposition. *J. Mater. Chem.*, 19:2999–3003, 2009.
- [82] Liisa J. Antila, Mikko J. Heikkilä; Viivi Aumanen, Marianna Kemell, Pasi Myllyperki, Markku Leskela; and Jouko E. I. Korppi-Tommola. Suppression of Forward Electron Injection from $\text{Ru}(\text{dcbpy})_2(\text{NCS})_{22}$ to Nanocrystalline TiO_2 Film As a Result of an Interfacial Al_2O_3 Barrier Layer Prepared with Atomic Layer Deposition. *The Journal of Physical Chemistry Letters*, 1(2):536–539, 2010.
- [83] Nicolas Třreault, Éric Arsenault, Leo-Philipp Heiniger, Navid Soheilnia, Jérémie Brillet, Thomas Moehl, Shaik Zakeeruddin, Geoffrey A. Ozin, and Michael Grätzel. High-efficiency dye-sensitized solar cell with three-dimensional photoanode. *Nano Letters*, 11(11):4579–4584, 2011.
- [84] Xianfeng Gao, Junhong Chen, and Chris Yuan. Enhancing the performance of free-standing TiO_2 nanotube arrays based dye-sensitized solar cells via ultra-precise control of the nanotube wall thickness. *Journal of Power Sources*, 240: 503 – 509, 2013.
- [85] Alex BF Martinson, Jeffrey W Elam, Joseph T Hupp, and Michael J Pellin. ZnO nanotube based dye-sensitized solar cells. *Nano letters*, 7(8):2183–2187, 2007.
- [86] Do Han Kim, Mark D. Losego, Kenneth Hanson, Leila Alibabaei, Kyoungmi Lee, Thomas J. Meyer, and Gregory N. Parsons. Stabilizing chromophore binding on TiO_2 for long-term stability of dye-sensitized solar cells using multi-component atomic layer deposition. *Phys. Chem. Chem. Phys.*, 16:8615–8622, 2014.
- [87] Ho-Jin Son, Chaiya Prasittichai, Joseph E. Mondloch, Langli Luo, Jinsong Wu, Dong Wook Kim, Omar K. Farha, and Joseph T. Hupp. Dye Stabilization and Enhanced Photoelectrode Wettability in Water-Based Dye-Sensitized Solar Cells through Post-assembly Atomic Layer Deposition of TiO_2 . *Journal of the American Chemical Society*, 135(31):11529–11532, 2013.
- [88] Neil P. Dasgupta, Chong Liu, Sean Andrews, Fritz B. Prinz, and Peidong Yang. Atomic layer deposition of platinum catalysts on nanowire surfaces for photoelectrochemical water reduction. *Journal of the American Chemical Society*, 135(35):12932–12935, 2013.
- [89] Neil P. Dasgupta, Hee Joon Jung, Orlando Trejo, Matthew T. McDowell, Aaron Hryciw, Mark Brongersma, Robert Sinclair, and Fritz B. Prinz. Atomic layer deposition of lead sulfide quantum dots on nanowire surfaces. *Nano Letters*, 11(3):934–940, 2011.

- [90] Brandon J. O'Neill, David H. K. Jackson, Jechan Lee, Christian Canlas, Peter C. Stair, Christopher L. Marshall, Jeffrey W. Elam, Thomas F. Kuech, James A. Dumesic, and George W. Huber. Catalyst design with atomic layer deposition. *ACS Catalysis*, 5(3):1804–1825, 2015.
- [91] Kun Cao, Jiaming Cai, Xiao Liu, and Rong Chen. Catalysts design and synthesis via selective atomic layer deposition. *Journal of Vacuum Science & Technology A: Vacuum, Surfaces, and Films*, 36(1):010801, 2018.
- [92] Thomas Young. An essay on the cohesion of fluids. *Philosophical Transactions of the Royal Society of London*, 95:65–87, 1805.
- [93] Arun K. Kota, Gibum Kwon, and Anish Tuteja. The design and applications of superomniphobic surfaces. *NPG Asia Materials*, 6(6):e109, 2014.
- [94] Robert N. Wenzel. Resistance of solid surfaces to wetting by water. *Industrial & Engineering Chemistry*, 28(8):988–994, 1936.
- [95] A. B. D. Cassie and S. Baxter. Wettability of porous surfaces. *Trans. Faraday Soc.*, 40:546–551, 1944.
- [96] Michael Nosonovsky. Multiscale roughness and stability of superhydrophobic biomimetic interfaces. *Langmuir*, 23(6):3157–3161, 2007.
- [97] Abraham Marmur. Wetting on hydrophobic rough surfaces: To be heterogeneous or not to be? *Langmuir*, 19(20):8343–8348, 2003.
- [98] Rulon E. Johnson and Robert H. Dettre. *Contact Angle Hysteresis*, chapter 7, pages 112–135. American Chemical Society, Washington, D.C., 1964.
- [99] Neelesh A. Patankar. On the modeling of hydrophobic contact angles on rough surfaces. *Langmuir*, 19(4):1249–1253, 2003.
- [100] Arun K. Kota, Yongxin Li, Joseph M. Mabry, and Anish Tuteja. Hierarchically structured superoleophobic surfaces with ultralow contact angle hysteresis. *Advanced Materials*, 24(43):5838–5843, 2012.
- [101] A. Tuteja, W. Choi, J. M. Mabry, G. H. McKinley, and R. E. Cohen. Robust omniphobic surfaces. *Proc. Natl. Acad. Sci. U. S. A.*, 105:18200–18205, 2008.
- [102] A. Tuteja, W. Choi, M. Ma, J. M. Mabry, S. A. Mazzella, G. C. Rutledge, G. H. McKinley, and R. E. Cohen. Designing superoleophobic surfaces. *Science*, 318:1618–1622, 2007.
- [103] Paul Denholm and Robert M. Margolis. Evaluating the limits of solar photovoltaics (PV) in traditional electric power systems. *Energy Policy*, 35(5):2852–2861, 2007.

- [104] Takashi Hisatomi, Jun Kubota, and Kazunari Domen. Recent advances in semiconductors for photocatalytic and photoelectrochemical water splitting. *Chem. Soc. Rev.*, 43:7520–7535, 2014.
- [105] Laurence M. Peter. Chapter 1 photoelectrochemistry: From basic principles to photocatalysis. In *Photocatalysis: Fundamentals and Perspectives*, pages 1–28. The Royal Society of Chemistry, 2016.
- [106] Michael G. Walter, Emily L. Warren, James R. McKone, Shannon W. Boettcher, Qixi Mi, Elizabeth A. Santori, and Nathan S. Lewis. Solar water splitting cells. *Chemical Reviews*, 110(11):6446–6473, 2010.
- [107] Carolin Zachaüs, Fatwa F. Abdi, Laurence M. Peter, and Roel Van De Krol. Photocurrent of BiVO_4 is limited by surface recombination, not surface catalysis. *Chemical Science*, 8(5):3712–3719, 2017.
- [108] F Garcia-Moliner and F Flores. Theory of electronic surface states in semiconductors. *Journal of Physics C: Solid State Physics*, 9(9):1609–1634, 1976.
- [109] Florian Le Formal, Nicolas Tetreault, Maurin Cornuz, Thomas Moehl, Michael Grätzel, and Kevin Sivula. Passivating surface states on water splitting hematite photoanodes with alumina overlayers. *Chemical Science*, 2(4):737–743, 2011.
- [110] Allen J Bard, Andrew B Bocarsly, Fu Ren F Fan, Erick G Walton, and Mark S Wrighton. The concept of fermi level pinning at semiconductor/liquid junctions. consequences for energy conversion efficiency and selection of useful solution redox couples in solar devices. *Journal of the American Chemical Society*, 102(11):3671–3677, 1980.
- [111] NREL. Reference solar spectral irradiance: Air mass 1.5, 2019. URL <https://rredc.nrel.gov/solar//spectra/am1.5/>.
- [112] A.J. Nozik. pn photoelectrolysis cells. *Applied Physics Letters*, 29(3):150–153, 1976.
- [113] Jaejin Song and Sangwoo Lim. Effect of Seed Layer on the Growth of ZnO Nanorods. *The Journal of Physical Chemistry C*, 111(2):596–600, 2007.
- [114] Sheng Xu and Zhong Lin Wang. One-dimensional ZnO nanostructures: Solution growth and functional properties. *Nano Research*, 4(11):1013–1098, 2011.
- [115] Lionel Vayssieres, Karin Keis, Sten-Eric Lindquist, and Anders Hagfeldt. Purpose-Built Anisotropic Metal Oxide Material: 3D Highly Oriented Microrod Array of ZnO. *The Journal of Physical Chemistry B*, 105(17):3350–3352, 2001.
- [116] Birkholz, Mario. *Thin Film Analysis by X-Ray Scattering*. Wiley-VCH Verlag GmbH & Co. KGaA, 2006.

- [117] J. W. Elam, Z. A. Sechrist, and S. M. George. ZnO/Al₂O₃ nanolaminates fabricated by atomic layer deposition: growth and surface roughness measurements. *Thin Solid Films*, 414(1):43–55, 2002.
- [118] Q. Jiang, L. H. Liang, and D. S. Zhao. Lattice Contraction and Surface Stress of fcc Nanocrystals. *The Journal of Physical Chemistry B*, 105(27):6275–6277, 2001.
- [119] L. H. Liang, J. C. Li, and Q. Jiang. Size-dependent melting depression and lattice contraction of Bi nanocrystals. *Physica B: Condensed Matter*, 334(1–2): 49–53, 2003.
- [120] S. Neeleshwar, C. L. Chen, C. B. Tsai, Y. Y. Chen, C. C. Chen, S. G. Shyu, and M. S. Seehra. Size-dependent properties of CdSe quantum dots. *Physical Review B*, 71(20):201307, 2005.
- [121] P. Bindu and Sabu Thomas. Estimation of lattice strain in ZnO nanoparticles: X-ray peak profile analysis. *Journal of Theoretical and Applied Physics*, 8(4): 123–134, 2014.
- [122] Q Jiang, D. S Zhao, and M Zhao. Size-dependent interface energy and related interface stress. *Acta Materialia*, 49(16):3143–3147, 2001.
- [123] J. J. Chambers, B. W. Busch, W. H. Schulte, T. Gustafsson, E. Garfunkel, S. Wang, D. M. Maher, T. M. Klein, and G. N. Parsons. Effects of surface pre-treatments on interface structure during formation of ultra-thin yttrium silicate dielectric films on silicon. *Applied Surface Science*, 181(1–2):78–93, 2001.
- [124] Sanny Verma and Suman L. Jain. Nanosized zinc peroxide (ZnO₂): a novel inorganic oxidant for the oxidation of aromatic alcohols to carbonyl compounds. *Inorganic Chemistry*, 1(7):534–539, 2014.
- [125] T. David, S. Goldsmith, and R. L. Boxman. Dependence of zinc oxide thin film properties on filtered vacuum arc deposition parameters. *Journal of Physics D: Applied Physics*, 38(14):2407, 2005.
- [126] Guangyuan Zheng, Yi Cui, Erdem Karabulut, Lars Wågberg, Hongli Zhu, and Liangbing Hu. Nanostructured paper for flexible energy and electronic devices. *MRS Bulletin*, 38(04):320–325, 2013.
- [127] Jesse. S. Jur, William J. Sweet, Christopher J. Oldham, and Gregory N. Parsons. Atomic Layer Deposition of Conductive Coatings on Cotton, Paper, and Synthetic Fibers: Conductivity Analysis and Functional Chemical Sensing Using All-Fiber Capacitors. *Advanced Functional Materials*, 21(11):1993–2002, 2011.
- [128] Lianbing Zhang and Mato Knez. Chapter 16 - atomic layer deposition for biomimicry. In Akhlesh Lakhtakia and Raúl J. Martín-Palma, editors, *Engineered Biomimicry*, pages 399 – 428. Elsevier, Boston, 2013.

- [129] Di Zhang. *Morphology Genetic Materials Templated from Nature Species*. Springer, 2012.
- [130] Jiajun Gu, Wang Zhang, Huilan Su, Tongxiang Fan, Shenmin Zhu, Qinglei Liu, and Di Zhang. Biomimetics: Morphology Genetic Materials Templated from Natural Species. *Advanced Materials*, 27(3):394–394, 2015.
- [131] Peng Tao, Wen Shang, Chengyi Song, Qingchen Shen, Fangyu Zhang, Zhen Luo, Nan Yi, Di Zhang, and Tao Deng. Bioinspired Engineering of Thermal Materials. *Advanced Materials*, 27(3):428–463, 2015.
- [132] R. G. Hobbs, N. Petkov, and J. D. Holmes. Semiconductor nanowire fabrication by bottom-up and top-down paradigms. *Chem. Mater.*, 24:1975–1991, 2012.
- [133] P. Yang, R. Yan, and M. Fardy. Semiconductor nanowire: Whats next? *Nano Lett.*, 10:1529–1536, 2010.
- [134] Z. Ren, Y. Guo, C.-H. Liu, and P.-X. Gao. Hierarchically nanostructured materials for sustainable environmental applications. *Front. Chem.*, 1:18, 2013.
- [135] S. H. Ko, D. Lee, H. W. Kang, K. H. Nam, J. Y. Yeo, S. J. Hong, C. P. Grigoriopoulos, and H. J. Sung. Nanoforest of Hydrothermally Grown Hierarchical ZnO Nanowires for a High Efficiency Dye-Sensitized Solar Cell. *Nano Lett.*, 11: 666–671, 2011.
- [136] M. J. Bierman and S. Jin. Potential applications of hierarchical branching nanowires in solar energy conversion. *Energy Environ. Sci.*, 2:1050–1059, 2009.
- [137] H. J. Fan, P. Werner, and M. Zacharias. Semiconductor nanowires: From self-organization to patterned growth. *Small*, 2:700–717, 2006.
- [138] J. F. Conley, L. Stecker, and Y. Ono. Directed Assembly of ZnO Nanowires on a Si Substrate without a Metal Catalyst Using a Patterned ZnO Seed Layer. *Nanotechnology*, 16:292, 2005.
- [139] X. Jiang, B. Tian, J. Xiang, F. Qian, G. Zheng, H. Wang, L. Mai, and C. M. Lieber. Rational growth of branched nanowire heterostructures with synthetically encoded properties and function. *Proc. Natl. Acad. Sci. U. S. A.*, 108: 12212–12216, 2011.
- [140] D. J. Milliron, S. M. Hughes, Y. Cui, L. Manna, J. Li, L.-W. Wang, and A. Paul Alivisatos. Colloidal nanocrystal heterostructures with linear and branched topology. *Nature*, 430:190–195, 2004.
- [141] K. Miszta, J. de Graaf, G. Bertoni, D. Dorfs, R. Brescia, S. Marras, L. Ceseracciu, R. Cingolani, R. van Roij, M. Dijkstra, and L. Manna. Hierarchical self-assembly of suspended branched colloidal nanocrystals into superlattice structures. *Nat. Mater.*, 10:872–876, 2011.

- [142] I. S. Cho, Z. Chen, A. J. Forman, D. R. Kim, P. M. Rao, T. F. Jaramillo, and X. Zheng. Branched TiO₂ Nanorods for Photoelectrochemical Hydrogen Production. *Nano Lett.*, 11:4978–4984, 2011.
- [143] D. Wang, F. Qian, C. Yang, Z. Zhong, and C. M. Lieber. Rational growth of branched and hyperbranched nanowire structures. *Nano Lett.*, 4:871–874, 2004.
- [144] Y. Zhao, M. Wei, J. Lu, Z. L. Wang, and X. Duan. Biotemplated hierarchical nanostructure of layered double hydroxides with improved photocatalysis performance. *ACS Nano*, 3:4009–4016, 2009.
- [145] T. Sun, L. Feng, X. Gao, and L. Jiang. Bioinspired surfaces with special wettability. *Acc. Chem. Res.*, 38:644–652, 2005.
- [146] J. Genzer and K. Efimenko. Recent developments in superhydrophobic surfaces and their relevance to marine fouling: A review. *Biofouling*, 22:339–360, 2006.
- [147] B. Leng, Z. Shao, G. de With, and W. Ming. Superoleophobic cotton textiles. *Langmuir*, 25:2456–2460, 2009.
- [148] C. Lee and C.-J. Kim. Underwater restoration and retention of gases on superhydrophobic surfaces for drag reduction. *Phys. Rev. Lett.*, 106:014502, 2011.
- [149] S. Pan, A. K. Kota, J. M. Mabry, and A. Tuteja. Superomniphobic surfaces for effective chemical shielding. *J. Am. Chem. Soc.*, 135:578–581, 2013.
- [150] G. Kwon, A. K. Kota, Y. Li, A. Sohani, J. M. Mabry, and A. Tuteja. On-demand separation of oil-water mixtures. *Adv. Mater.*, 24:3666–3671, 2012.
- [151] A. Ahuja, J. A. Taylor, V. Lifton, A. A. Sidorenko, T. R. Salamon, E. J. Lobaton, P. Kolodner, and T. N. Krupenkin. Nanonails: A simple geometrical approach to electrically tunable superlyophobic surfaces. *Langmuir*, 24:9–14, 2008.
- [152] L. Cao, T. P. Price, M. Weiss, and D. Gao. Super water- and oil-repellent surfaces on intrinsically hydrophilic and oleophilic porous silicon films. *Langmuir*, 24:1640–1643, 2008.
- [153] K. Koch, H. F. Bohn, and W. Barthlott. Hierarchically sculptured plant surfaces and superhydrophobicity. *Langmuir*, 25:14116–14120, 2009.
- [154] Y. Su, B. Ji, K. Zhang, H. Gao, Y. Huang, and K. Hwang. Nano to micro structural hierarchy is crucial for stable superhydrophobic and water-repellent surfaces. *Langmuir*, 26:4984–4989, 2010.
- [155] D. Wu, J.-N. Wang, S.-Z. Wu, Q.-D. Chen, S. Zhao, H. Zhang, H.-B. Sun, and L. Jiang. Three-level biomimetic rice-leaf surfaces with controllable anisotropic sliding. *Adv. Funct. Mater.*, 21:2927–2932, 2011.

- [156] J.-Y. Lee, S. Pechook, D.-J. Jeon, B. Pokroy, and J.-S. Yeo. Three-Dimensional Triple Hierarchy Formed by Self-Assembly of Wax Crystals on CuO Nanowires for Nonwetable Surfaces. *ACS Appl. Mater. Interfaces*, 6:4927–4934, 2014.
- [157] D. L. McDowell and G. B. Olson. *Concurrent design of hierarchical materials and structures*, pages 207–240. Springer Netherlands, 2009.
- [158] G. B. Olson. Computational design of hierarchically structured materials. *Science*, 277:1237–1242, 1997.
- [159] R. Lakes. Materials with structural hierarchy. *Nature*, 361:511–515, 1993.
- [160] P. Fratzl and R. Weinkamer. Natures hierarchical materials. *Prog. Mater. Sci.*, 52:1263–1334, 2007.
- [161] C. Sanchez, H. Arribart, and M. M. Giraud Guille. Biomimetism and bioinspiration as tools for the design of innovative materials and systems. *Nat. Mater.*, 4:277–288, 2005.
- [162] U. G. K. Wegst, H. Bai, E. Saiz, A. P. Tomsia, and R. O. Ritchie. Bioinspired structural materials. *Nat. Mater.*, 14:23–36, 2015.
- [163] M. Callies and D. Que re. On water repellency. *Soft Matter*, 1:55, 2005.
- [164] D. Que re. Rough ideas on wetting. *Phys. A*, 313:32–46, 2002.
- [165] H. Zhao, K.-C. Park, and K.-Y. Law. Effect of surface texturing on superoleophobicity, contact angle hysteresis, and robustness. *Langmuir*, 28:14925–12935, 2012.
- [166] Qimin Yan, Jie Yu, Santosh K. Suram, Lan Zhou, Aniketa Shinde, Paul F. Newhouse, Wei Chen, Guo Li, Kristin A. Persson, John M. Gregoire, and Jeffrey B. Neaton. Solar fuels photoanode materials discovery by integrating high-throughput theory and experiment. *Proceedings of the National Academy of Sciences*, 114(12):3040–3043, 2017.
- [167] Kevin Sivula and Roel Van De Krol. Semiconducting materials for photoelectrochemical energy conversion. *Nature Reviews Materials*, 1(2):15010, 2016.
- [168] Yiseul Park, Kenneth J. McDonald, and Kyoung-Shin Choi. Progress in bismuth vanadate photoanodes for use in solar water oxidation. *Chemical Society Reviews*, 42(6):2321–2337, 2013.
- [169] Fatwa F Abdi, Tom J Savenije, Matthias M May, Bernard Dam, and Roel van de Krol. The origin of slow carrier transport in bivo 4 thin film photoanodes: A time-resolved microwave conductivity study. *The Journal of Physical Chemistry Letters*, 4:2752–2757, 2013.

- [170] Diane K. Zhong, Sujung Choi, and Daniel R. Gamelin. Near-Complete Suppression of Surface Recombination in Solar Photoelectrolysis by Co-Pi Catalyst-Modified W:BiVO₄. *Journal of the American Chemical Society*, 133(45):18370–18377, 2011.
- [171] Fatwa F. Abdi, Lihao Han, Arno H.M. Smets, Miro Zeman, Bernard Dam, and Roel Van De Krol. Efficient solar water splitting by enhanced charge separation in a bismuth vanadate-silicon tandem photoelectrode. *Nature Communications*, 4(1):ncomms3195, 2013.
- [172] Pratap M. Rao, Lili Cai, Chong Liu, In Sun Cho, Chi Hwan Lee, Jeffrey M. Weisse, Peidong Yang, and Xiaolin Zheng. Simultaneously Efficient Light Absorption and Charge Separation in WO₃/BiVO₄ Core/Shell Nanowire Photoanode for Photoelectrochemical Water Oxidation. *Nano Letters*, 14(2):1099–1105, 2014.
- [173] Tae Woo Kim and Kyoung Shin Choi. Nanoporous bivo₄ photoanodes with dual-layer oxygen evolution catalysts for solar water splitting. *Science*, 343(6174):990–994, 2014.
- [174] Lite Zhou, Chenqi Zhao, Binod Giri, Patrick Allen, Xiaowei Xu, Hrushikesh Joshi, Yangyang Fan, Lyubov V. Titova, and Pratap M. Rao. High Light Absorption and Charge Separation Efficiency at Low Applied Voltage from Sb-Doped SnO₂/BiVO₄ Core/Shell Nanorod-Array Photoanodes. *Nano Letters*, 16(6):3463–3474, 2016.
- [175] Jason A. Seabold and Kyoung-Shin Choi. Efficient and stable photo-oxidation of water by a bismuth vanadate photoanode coupled with an iron oxyhydroxide oxygen evolution catalyst. *Journal of the American Chemical Society*, 134(4):2186–2192, 2012.
- [176] Neil P. Dasgupta and Peidong Yang. Semiconductor nanowires for photovoltaic and photoelectrochemical energy conversion. *Frontiers of Physics*, 9(3):289–302, 2013.
- [177] Jih Sheng Yang and Jih Jen Wu. Low-potential driven fully-depleted BiVO₄/ZnO heterojunction nanodendrite array photoanodes for photoelectrochemical water splitting. *Nano Energy*, 32(October 2016):232–240, 2017.
- [178] Morgan Stefik. Atomic layer deposition of bismuth vanadates for solar energy materials. *ChemSusChem*, 9(13):1727–1735, 2016.
- [179] Mikael Schuisky, Kaupo Kukli, Mikko Ritala, Anders Hrsta, and Markku Leskela. Atomic layer CVD in the Bi-Ti-O system. *Chemical Vapor Deposition*, 6(3):139–145, 2000.
- [180] B. Lamm, A. Sarkar, and M. Stefik. Surface functionalized atomic layer deposition of bismuth vanadate for single-phase scheelite. *Journal of Materials Chemistry A*, 5(13):6060–6069, 2017.

- [181] Dustin Z. Austin, Derryl Allman, David Price, Sallie Hose, Mark Saly, and John F. Conley. Atomic layer deposition of bismuth oxide using $\text{Bi}(\text{OCMe}_2\text{iPr})_3$ and H_2O . *Journal of Vacuum Science & Technology A: Vacuum, Surfaces, and Films*, 32(1):01A113, 2014.
- [182] Timo Hatanpää; Marko Vehkamäki, Mikko Ritala, and Markku Leskela: Study of bismuth alkoxides as possible precursors for ALD. *Dalton Transactions*, 39(13):3219–3226, 2010.
- [183] J. Musschoot, D. Deduytsche, R. L. Van Meirhaeghe, and C. Detavernier. ALD of vanadium oxide. *ECS Transactions*, 25(4):29–37, 2009.
- [184] Eric Kazyak, Kuan Hung Chen, Kevin N. Wood, Andrew L. Davis, Travis Thompson, Ashley R. Bielinski, Adrian J. Sanchez, Xiang Wang, Chongmin Wang, Jeff Sakamoto, and Neil P. Dasgupta. Atomic Layer Deposition of the Solid Electrolyte Garnet $\text{Li}_7\text{La}_3\text{Zr}_2\text{O}_{12}$. *Chemistry of Materials*, 29(8):3785–3792, 2017.
- [185] Kiyotaka Uchida and Akimi Ayame. Dynamic xps measurements on bismuth molybdate surfaces. *Surface Science*, 357-358:170 – 175, 1996.
- [186] R. Holm and S. Storp. Esca studies on changes in surface composition under ion bombardment. *Applied physics*, 12(1):101–112, 1977.
- [187] Jason K Cooper, Sheraz Gul, Francesca M Toma, Le Chen, Yi Sheng Liu, Jinghua Guo, Joel W Ager, Junko Yano, and Ian D Sharp. Indirect bandgap and optical properties of monoclinic bismuth vanadate. *Journal of Physical Chemistry C*, 119(6):2969–2974, 2015.
- [188] S. Tokunaga, H. Kato, and A. Kudo. Selective preparation of monoclinic and tetragonal BiVO_4 with scheelite structure and their photocatalytic properties. *Chemistry of Materials*, 13(12):4624–4628, 2001.
- [189] Vineet Nair, Craig L. Perkins, Qiyin Lin, and Matt Law. Textured nanoporous mo:bivo_4 photoanodes with high charge transport and charge transfer quantum efficiencies for oxygen evolution. *Energy and Environmental Science*, 9(4):1412–1429, 2016.
- [190] Benjamin Lamm, Bartek J Trzeniewski, Henning Dscher, Wilson A Smith, and Morgan Stefik. Emerging Postsynthetic Improvements of BiVO_4 Photoanodes for Solar Water Splitting. *ACS Energy Letters*, 3(1):112–124, 2018.
- [191] Yongqi Liang, Toshiki Tsubota, Lennard P. A. Mooij, and Roel van de Krol. Highly Improved Quantum Efficiencies for Thin Film BiVO_4 Photoanodes. *The Journal of Physical Chemistry C*, 115(35):17594–17598, 2011.
- [192] Pongkarn Chakthranont, Blaise A. Pinaud, Linsey C. Seitz, Arnold J. Forman, and Thomas F. Jaramillo. Improving the photoelectrochemical performance of

- hematite by employing a high surface area scaffold and engineering solid-solid interfaces. *Advanced Materials Interfaces*, 3(7):1–9, 2016.
- [193] Segi Byun, Bumsoo Kim, Seokwoo Jeon, and Byungha Shin. Effects of a SnO₂ hole blocking layer in a BiVO₄-based photoanode on photoelectrocatalytic water oxidation. *Journal of Materials Chemistry A*, 5(15):6905–6913, 2017.
- [194] Benjamin Lamm, Lite Zhou, Pratap Rao, and Morgan Stefik. Atomic Layer Deposition of Space-Efficient SnO₂ Underlayers for BiVO₄ Host-Guest Architectures for Photoassisted Water Splitting. *ChemSusChem*, 12(9):1916–1924, 2019.
- [195] Sean P. Berglund, David W. Flaherty, Nathan T. Hahn, Allen J. Bard, and C. Buddie Mullins. Photoelectrochemical oxidation of water using nanostructured bivo₄ films. *The Journal of Physical Chemistry C*, 115(9):3794–3802, 2011.
- [196] Le Chen, Esther Alarcón-Lladó, Mark Hettick, Ian D. Sharp, Yongjing Lin, Ali Javey, and Joel W. Ager. Reactive sputtering of bismuth vanadate photoanodes for solar water splitting. *The Journal of Physical Chemistry C*, 117(42):21635–21642, 2013.
- [197] Esther Alarcón-Lladó, Le Chen, Mark Hettick, Neeka Mashouf, Yongjing Lin, Ali Javey, and Joel W. Ager. Bivo₄ thin film photoanodes grown by chemical vapor deposition. *Phys. Chem. Chem. Phys.*, 16:1651–1657, 2014.
- [198] Francesca M. Toma, Jason K. Cooper, Viktoria Kunzelmann, Matthew T. McDowell, Jie Yu, David M. Larson, Nicholas J. Borys, Christine Abelyan, Jeffrey W. Beeman, Kin Man Yu, Jinhui Yang, Le Chen, Matthew R. Shaner, Joshua Spurgeon, Frances A. Houle, Kristin A. Persson, and Ian D. Sharp. Mechanistic insights into chemical and photochemical transformations of bismuth vanadate photoanodes. *Nature Communications*, 7:12012, 2016.
- [199] Chang Woo Kim, Young Seok Son, Myung Jong Kang, Do Yoon Kim, and Young Soo Kang. (040)-crystal facet engineering of bivo₄ plate photoanodes for solar fuel production. *Advanced Energy Materials*, 6(4):1501754, 2016.
- [200] Fatwa F. Abdi and Roel van de Krol. Nature and light dependence of bulk recombination in co-pi-catalyzed bivo₄ photoanodes. *The Journal of Physical Chemistry C*, 116(17):9398–9404, 2012. doi: 10.1021/jp3007552.
- [201] Benjamin Klahr, Sixto Gimenez, Francisco Fabregat-Santiago, Juan Bisquert, and Thomas W. Hamann. Electrochemical and photoelectrochemical investigation of water oxidation with hematite electrodes. *Energy and Environmental Science*, 5(6):7626–7636, 2012.
- [202] Yongjing Lin, Sa Zhou, Stafford W. Sheehan, and Dunwei Wang. Nanonet-based hematite heteronanostructures for efficient solar water splitting. *Journal of the American Chemical Society*, 133(8):2398–2401, 2011.

- [203] Rui Liu, Yongjing Lin, Lien Yang Chou, Stafford W. Sheehan, Wangshu He, Fan Zhang, Harvey J M Hou, and Dunwei Wang. Water splitting by tungsten oxide prepared by atomic layer deposition and decorated with an oxygen-evolving catalyst. *Angewandte Chemie - International Edition*, 50(2):499–502, 2011.
- [204] Yuan Gao, Omid Zandi, and Thomas W. Hamann. Atomic layer stack deposition-annealing synthesis of cuwo4. *Journal of Materials Chemistry A*, 4(8):2826–2830, 2016.
- [205] Manjunath Puttaswamy, Marko Vehkamäki, Kaupo Kukli, Mukesh Chandra Dimri, Marianna Kemell, Timo Hatanpää; Mikko J. Heikkilä; Kenichiro Mizohata, Raivo Stern, Mikko Ritala, and Markku Leskela. Bismuth iron oxide thin films using atomic layer deposition of alternating bismuth oxide and iron oxide layers. *Thin Solid Films*, 611:78–87, 2016.
- [206] Omid Zandi and Thomas W. Hamann. Enhanced water splitting efficiency through selective surface state removal. *The Journal of Physical Chemistry Letters*, 5(9):1522–1526, 2014.
- [207] Ludmilla Steier, Jingshan Luo, Marcel Schreier, Matthew T. Mayer, Timo Sajavaara, and Michael Grätzel. Low-temperature atomic layer deposition of crystalline and photoactive ultrathin hematite films for solar water splitting. *ACS Nano*, 9(12):11775–11783, 2015.
- [208] Maureen H. Tang, Pongkarn Chakthranont, and Thomas F. Jaramillo. Top-down fabrication of fluorine-doped tin oxide nanopillar substrates for solar water splitting. *RSC Adv.*, 7:28350–28357, 2017.
- [209] Kazuhiro Sayama, Atsushi Nomura, Takeo Arai, Tsuyoshi Sugita, Ryu Abe, Masatoshi Yanagida, Takashi Oi, Yasukazu Iwasaki, Yoshimoto Abe, and Hideki Sugihara. Photoelectrochemical decomposition of water into H₂ and O₂ on porous BiVO₄ thin-film electrodes under visible light and significant effect of Ag Ion treatment. *Journal of Physical Chemistry B*, 110(23):11352–11360, 2006.
- [210] Savio J.A. Moniz, Jun Zhu, and Junwang Tang. 1D Co-Pi modified BiVO₄/ZnO junction cascade for efficient photoelectrochemical water cleavage. *Advanced Energy Materials*, 4(10):1301590, 2014.
- [211] Rie Saito, Yugo Miseki, and Kazuhiro Sayama. Highly efficient photoelectrochemical water splitting using a thin film photoanode of bivo₄/sno₂/wo₃ multi-composite in a carbonate electrolyte. *Chem. Commun.*, 48:3833–3835, 2012.
- [212] Guangnan Meng, Jayson Paulose, David R. Nelson, and Vinothan N. Manoharan. Elastic instability of a crystal growing on a curved surface. *Science*, 343(6171):634–637, 2014.
- [213] Leopoldo R. Gómez, Nicolás A. García, Vincenzo Vitelli, JoseLorenzana, and Daniel A. Vega. Phase nucleation in curved space. *Nature Communications*, 6: 6856, 2015.

- [214] Zongyan Zhao, Zhaosheng Li, and Zhigang Zou. Electronic structure and optical properties of monoclinic clinobisvanite BiVO_4 . *Phys. Chem. Chem. Phys.*, 13: 4746–4753, 2011.
- [215] Yanying Feng, Zhaoying Zhou, Xiongying Ye, and Jijun Xiong. Passive valves based on hydrophobic microfluidics. *Sensors and Actuators A: Physical*, 108 (1):138 – 143, 2003.
- [216] Mark C. Draper, Colin R. Crick, Viktorija Orlickaite, Vladimir A. Turek, Ivan P. Parkin, and Joshua B. Edel. Superhydrophobic surfaces as an on-chip microfluidic toolkit for total droplet control. *Analytical Chemistry*, 85(11):5405–5410, 2013.
- [217] James A Callow and Maureen E Callow. Trends in the development of environmentally friendly fouling-resistant marine coatings. *Nature Communications*, 2: 244, 2011.
- [218] Binbin Zhang, Xiuhua Hu, Qingjun Zhu, Xiutong Wang, Xia Zhao, Congtao Sun, Yantao Li, and Baorong Hou. Controllable dianthus caryophyllus-like superhydrophilic/superhydrophobic hierarchical structure based on self-congregated nanowires for corrosion inhibition and biofouling mitigation. *Chemical Engineering Journal*, 312:317 – 327, 2017.
- [219] Nagarajan Padmavathy and Rajagopalan Vijayaraghavan. Enhanced bioactivity of ZnO nanoparticles—an antimicrobial study. *Science and Technology of Advanced Materials*, 9(3):035004, 2008.
- [220] Robin E. Rodríguez, Sneha P. Agarwal, Shun An, Eric Kazyak, Debashree Das, Wen Shang, Rachael Skye, Tao Deng, and Neil P. Dasgupta. Biotemplated morpho butterfly wings for tunable structurally colored photocatalysts. *ACS Applied Materials & Interfaces*, 10(5):4614–4621, 2018.
- [221] Xueqing Zhang and Anja Bieberle-Hütter. Modeling and simulations in photoelectrochemical water oxidation: From single level to multiscale modeling. *ChemSusChem*, 9(11):1223–1242, 2016.
- [222] Chengxiang Xiang, Andrew C. Meng, and Nathan S. Lewis. Evaluation and optimization of mass transport of redox species in silicon microwire-array photoelectrodes. *Proceedings of the National Academy of Sciences*, 109(39):15622–15627, 2012.
- [223] Kelley M. H. Young and Thomas W. Hamann. Enhanced photocatalytic water oxidation efficiency with Ni(OH)_2 catalysts deposited on $\alpha\text{-Fe}_2\text{O}_3$ via ALD. *Chem. Commun.*, 50:8727–8730, 2014.